THE EFFECT OF FLUID FLOW IN FAULT GOUGE DURING SIMULATED EARTHQUAKES

A Thesis

by

KEVIN KENNETH HIGBY

Submitted to the Office of Graduate and Professional Studies of
Texas A&M University
in partial fulfillment of the requirements for the degree

MASTER OF SCIENCE

Chair of Committee,	David W. Sparks
Committee Members,	Benchun Duan
	Marcelo Sanchez
Head of Department,	Michael Pope

May 2016

Major Subject: Geophysics

ABSTRACT

When the frictional strength of a fault zone is met, displacement occurs within the fault zone. Displacement can occur at a seismogenic or aseismic velocity. Seismogenic events cause devastating earthquakes while aseismic activity is the result of low velocity slip events. These slow slip events are thought to be from over pressured pore pressures present in the fault zone.

This work investigates the effect of pore fluid flow within fault gouge during an earthquake by using a grain scale numerical model. Fault gouge is simulated using a Discrete Element Model (DEM) that is coupled with grain motion to generate pressures from fluid flow. We compare the evolution of an earthquake using numerical simulations that began with identical granular arrangements run with a high permeability (drained) and a low permeability (undrained). Drained simulations are defined as those where fluid can flow freely enough such that the slip event is not affected by it. Undrained simulations are those in which pore fluid pressure cannot flow, and the strength of the system is severely affected by pressure perturbations.

Type I events the undrained system reached a lower static strength while Type II events are those where the undrained system achieved a higher static strength. Local granular rearrangements are responsible for the strengthening or weakening of the undrained events.

The slip velocities during a simulated earthquake in a drained system are well modeled by the block slider model with a constant coefficient of dynamic friction. However, a number of undrained earthquakes showed complex slip characteristics

including abrupt changes in velocity and a variable dynamic resistance. These slip events resemble creep-like and tremor-like behavior seen in natural subduction zones and caused by pressure perturbations within the gouge zone.

We find fluid pressure perturbations can weaken the static strength of undrained systems, but not always. This shows reductions in pressures play the dominant role in controlling the strength of a system. In addition, the dynamic resistance of complex events is primarily controlled by fluid flow, and not a variable coefficient of dynamic friction.

TABLE OF CONTENTS

Page

LIST OF FIGURES

Page

LIST OF TABLES

Page

I. INTRODUCTION

Large earthquakes release colossal amounts of elastic potential energy into the Earth's crust in the form of seismic waves. These events cause extensive deformation to the surrounding country rock while devastating infrastructure. It is vital to have an understanding of all components in a fault system, and how their dynamic interactions effect the initiation, termination and evolution of an earthquake.

Earthquakes are unstable displacement along a fault when the frictional strength of the fault is met by applied shear stress. The ability for an earthquake to occur is dependent on the seismogenic zone's resistance to shear forces. In particular, there is a dependence of frictional resistance of slip velocity. For example, a velocity weakening behavior is necessary for natural fault zones where unstable slip occurs. This means the fault zones resistance to shear stress lowers as the earthquake takes place.

Mature fault zones consist of three main components: intact and undamaged country rock, a highly fractured damage zone, and a fault core (Figure 1). During slip, material in the core of a fault becomes ground and crushed. Over time, this results in a fine granular material in the core called fault gouge. The strength of this zone controls the stability of a fault (resistance to shear forces) because most displacement and deformation occurs in this component.

Typically, when earthquakes occur and relieve stress, the result is sliding along the fault on the order of meters per second. However, other methods of stress relief within fault zones have been detected. For example, fault creep is a constant slow and steady

slippage that occurs in the fault core without being accompanied by a seismogenic event. Creep occurs when the fault relieves stress at a similar rate that its' being loaded (centimeters per year). An additional way to relieve stress placed on a fault zone is through earthquake "episodic" tremors. Tremors are low velocity slip events that take place during discrete intervals of time. It has been suggested that a possible mechanism that causes creep and tremors is the interaction of fluid pressures and the fault gouge at depth [*Sleep & Blanpied,* 1992; *Obara,* 2002; *Katsumata & Kamaya,* 2003]. These fluid pressures change the strength of the fault from fluid pressurization and through chemical reactions with the surrounding minerals.

The dynamics of fault gouge have been widely studied because thought-provoking behaviors arises when they are under shear. A grain-scale numerical model by Cundall & Strack [1979], was adopted to model fault gouge as discrete particles. Since then, a number of numerical experiments have highlighted intriguing behaviors of fault gouge such as the fact that shear stress highly localizes in dry fault gouge by forming shear bands where the frictional resistance is a minimum [*Iwashita & Oda*, 1998; *Aharonov & Sparks*, 2002; *Daub et al*., 2008]. Frictional resistance controls the stability of fault zones and granular systems under shear, and thus has been studied in laboratories [*Engelder et al*., 1975; *Byerlee et al*., 1978; *Marone et al*., 1990; *Nasuno et al*., 1997; *Karner & Marone*, 1998; *Leoni et al*., 2011; *Liao et al.,* 2014] and numerical experiments [*Hayakawa*, 1999; *Rathbun et al*., 2013] to gain insight on the frictional properties of fault gouge. Even though extensive research has been performed, a unified constitutive law describing friction in shearing gouge has yet to be formulated [*Marone*, 1998].

A unique characteristic of granular material is that instead of being a continuum, it is a set of touching particles separated by voids. The Discrete Element Method (DEM) treats grains as discrete entities that interact through simple contact laws. Figure 2A shows the granular system after it has been compacted under a uniform confining stress. Here, the grains are outlined by faint circles and are shaded by their total contact force; warmer colors indicate a large contact force, while cooler colors represent little to no contact force. In addition, the thickness of lines connecting the centers of grains designates the magnitude and direction of the contact force on a particular grain – thicker lines indicate a larger contact force. When granular materials are subject to an imposed normal or shear force by boundaries, they non-uniformly distribute the force. The largest forces arrange in a contact force network and are known as force chains. The phenomenon of force chain formation and their role in supporting systems has been studied under laboratory conditions [*Daniels & Hayman*, 2008, *Majmudar & Behringer*, 2005], numerical models [*Radjai et al*., 1999; *Tordesillas & Muthuswamy*, 2009; *Guo*, 2012] and is illustrated in Figure 2B. In Figure 2B, a shear force has been applied to the top wall creating deviatoric stresses. These chains form in a favorable position geometrically to support the applied stress and are aligned in the direction of the maximum principal stress. The behavior of these force chains will become a controlling component of the stability of the system under shear when fluid is included in the model.

Another important element of natural fault zones is the abundant presence of fluids in the pore space, which can dramatically affect the fault's stability by flowing into and out of the fault's damage zone and core [*Nur & Byerlee*, 1971]. The dependence of the

strength (shear stress required to deform a saturated material), τ , on fluid pressures P , was first pointed out by Terzaghi [1943]. Terzaghi discovered that fluctuations in pore fluid pressures can strongly affect the strength of the system as governed by Equation 1.

$$\tau = \mu(\sigma - P) = \mu\sigma_e \quad [1]$$

Here, μ is the surface coefficient of friction, σ is the normal stress, P is pore fluid pressure and σ_e is defined as the effective normal stress from the interaction of pore fluid pressures with the applied normal stress. According to Equation 1, reductions in local pore pressure strengthen a granular system while increases in pore pressure weaken the system, causing it to be more prone to failure.

These pressure fluctuations are especially important in a granular material where deformation is accompanied by local dilation and compaction of the pore space. As shear commences, local areas of the fault gouge dilate and compact driving local changes in fluid pressures that diffuse throughout the system overtime. These changes in local pore pressure (dependent on compaction or dilation) can weaken or strengthen the granular skeleton. Because the damage zone surrounding the fault core is often highly fractured [*Chester & Logan*, 1987; *Mitchell et al.,* 2011], fluid flow through the damage zone will act to mitigate significant pressurizations and depressurizations. However, if the gouge permeability is low, rapid deformation will still produce transient pressure fluctuations that cannot be drained in the time scale of an earthquake. Any pressure change in the gouge changes the effective normal stress, and hence, the ability to initiate or terminate an earthquake. This thesis will explore some of the consequences of fluid effects on a partially-drained fault gouge during slip.

This project aims to gain insight on the effect of fluid flow within a gouge layer under shear using a grain-scale numerical model. Numerical models allow the comparison of how dynamics within a gouge layer evolve throughout a simulated earthquake. Under the right loading conditions, numerical methods can reproduce stick-slip behavior similar to a natural fault zone [*Aharonov & Sparks*, 2004; *Volfson et al.,* 2004; *Tordesillas & Muthuswamy*, 2009; *Cimarra et al.,* 2011]. We investigate the effect of fluid pressure on granular systems undergoing stick-slip behavior by varying the permeability of the gouge. All simulations are nominally "drained" because the boundary conditions we use allow fluid to flow into and out of the gouge zone. If fluid can flow between the gouge and damage zone so freely that fluid pressures aren't changed by local dilations and compactions (fully drained), the system responds to shear as if fluids were absent – effectively a "dry" system. On the other hand, a low permeability gouge zone will retard fluid flow to the damage zone and will act as partially drained or an effectively undrained ("wet") system. The main question we wish to answer is how local perturbations in fluid pressure influence the evolution of a slip event.

II. PREVIOUS NUMERICAL STUDIES OF SHEARING FULLY DRAINED FAULT GOUGE

Past simulations of dry granular material under shear have shown that episodic slip, is in some ways, similar to a simple block-slider model [*Aharonov & Sparks*, 2004]. A simple block-slider model consists of a moveable block on a fixed surface with a plane of contact between the two. In-between these two surfaces, irregularities may exist with some coefficient of static and dynamic friction. The block has a spring attached to it with a defined stiffness that is pulled at a fixed velocity. Once the force of the spring overcomes the surface's static resistance to shear, the block slides relieving a portion of the shear stress. When the plane of contact has a constant coefficient of dynamic friction during slip that is lower than the static friction, the block slider model can give stick-slip motion under some conditions.

Previous numerical work performed by Aharonov and Sparks [2004] applied shear stress to a layer of grains similarly to the block-slider model. The found two end members of granular behavior: stick-slip behavior and continuous shear. They used the Discrete Element Method to simulate a 2-D layer consisting of approximately 550 quartz grains. In the model, the top and bottom walls are rigid while the system was periodic in the layer-parallel direction, simulating an annulus of grains similar to a rotary shear experiment. The top wall is analogous to the block in a block-slider model and the fault gouge is equivalent to the contact surface. To simulate shearing fault gouge, they applied a shear stress to the top block using a simulated spring.

Aharonov and Sparks were able to quantify, for a range of loading conditions, when stick-slip behavior and continuous shear arises in granular fault gouge. They found that stick-slip occurs within simulated fault gouge when lower loading rates and higher confining stresses were used during their numerical experiments (Figure 3).

If the friction during slip is constant, the force balance of a block-slider model during motion can be modeled as a simple harmonic oscillator (Equation 2). In this equation, m_b is the mass of the block, $\frac{d^2x}{dt^2}$ is acceleration, k_s is the driving springs' stiffness, $\Delta x(t)$ describes the stretch on the spring from its' natural length, N is the normal force the block exerts on the surface, μ_d is the dynamic coefficient of friction, $\Delta x(0)$ is the stretch on the spring when the system has reached its' static strength, V_s is the velocity the spring is pulled at, $x(t)$ is the displacement of the block and μ_s is the static coefficient of friction.

$$\begin{aligned} m_b \frac{d^2x}{dt^2} &= k_s \Delta x(t) - N\mu_d \\ m_b \frac{d^2x}{dt^2} &= k_s \left(\Delta x(0) + V_s t - x(t)\right) - N\mu_d \\ m_b \frac{d^2x}{dt^2} &\approx k_s x(t) - N\left(\mu_s - \mu_d\right) \end{aligned} \qquad [2]$$

The solution for the velocity of the block V_w (Equation 3) can be determined by solving Equation 2 subject to the initial condition $k_s \Delta x(t=0) = N\mu_s$ and under the assumption that further loading of the spring during the slip is effectively zero $\left(kV_s t << x(t)\right)$. This equation describes the temporal evolution of the block during a slip event beginning at

$t = 0$.

$$V_w(t) \approx \frac{N\Delta\mu}{\sqrt{k_s m_b}} \sin\left(\sqrt{\frac{k_s}{m_b}}t\right) \qquad [3]$$

Here, $\Delta\mu$ is the difference between the coefficient of static (μ_s) and coefficient of dynamic friction (μ_d). An important aspect of Equation 3 is that the top wall velocity will resemble a sine wave if and only if μ_d is a constant during the slip event. It is also important to note that in a periodic granular layer, N translates into approximately a uniform confining stress.

Figure 4 shows some resultant wall velocity curves for a suite of experiments from Aharonov and Sparks [2004] undergoing unstable sliding. In these simulations, only a simple coefficient of friction is specified: the contact friction of grain surfaces is held at 0.5. The resulting bulk static and dynamic frictional resistance emerges naturally from the model. In Figure 4, the vertical axis is dimensionless scaled wall velocity and the horizontal axis is dimensionless time. The velocity profiles produced by their experiments are in agreement with the approximate analytical solution for a block slider (Equation 3). However, there are some higher-frequency fluctuations inferred to be from individual granular collisions during slip; an artifact that Equation 3 does not account for. If one were to average the various experiments together, a less-noisy sine wave would result in agreement with Equation 3. In addition, there is a characteristic slip-time associated with a granular layer that agrees with the period of the predicted slip in Equation 3. All of this suggests that the bulk friction in the granular layer behaves like the block-slider model; μ_d is less than μ_s, and appears to be constant during slip even

though grain surfaces in the model only have a simple fixed coefficient of friction. Aharonov and Sparks [2004] were able to estimate $\Delta\mu$ from conditions at which slip transitions from episodic to stable sliding.

This study will differ from Aharonov and Sparks [2004] in the following ways: First, a significantly larger system will be modeled (~10,000 grains), and the top wall will be loaded orders of magnitude slower than those shown in their phase diagram: as a result the displacement of the top wall is on the orders of hundreds of grains, instead of a few. Second, fluid pressure effects that are fully coupled to the granular forces will be included to investigate the role of pressure changes on the initiation, evolution and termination of an earthquake.

III. DISCRETE ELEMENT MODEL (DEM) OF SATURATED GRANULAR SYSTEMS

To investigate the dynamics of granular fault gouge under shear, the two-dimensional Discrete Element Method [*Cundall & Strack,* 1979] for approximately 10,000 densely packed spherical grains is used. This allows us to calculate individual contact forces using the Hertz-Mindlin contact model for spheres, and track the motions of grains. To account for fluid pressure effects in a saturated granular material, we use the method outline by Goren et. al [2011], which calculates the fluid pressures formed by local grain motions using a finite difference scheme, and the effect of pressure gradients on the grains. We use the numerical model developed by Aharonov & Sparks [2004], Goren et al. [2011] and is described in more detail in Appendix C. A detailed derivation of the calculation of pore fluid pressures can be found in Goren et. al [2011] and Appendix C.

We numerically approximate the temporal evolution of fluid pressures (Equation 18, Appendix C) by using a finite difference grid to average fluid pressures and grain velocities across a few grains. Gradients in these pressures act as a drag force on individual grains. This model assumes a Darcy-like flow and the average permeability is controlled in the model, but does vary spatially with local porosity. In our simulations, the mean permeability is about $10^{-14}\ m^2$. Local permeability is calculated dynamically and varies from approximately $3\times10^{-14}\ m^2$ to $6\times10^{-15}\ m^2$.

After non-dimensionlization of the pressure equation, Goren et al. [2011]

formulated a term called the Deborah Number (De), which describes the interplay between fluid pressure diffusion by flow and pressure generation from matrix deformation:

$$De = \frac{l^2/D}{l/u_0} = \frac{lu_0}{D} = \frac{t_{diffusion}}{t_{generation}} \quad [4]$$

Here D is the diffusivity of pressure dependent on local permeability, fluid viscosity and fluid compressibility, l is the dimensional distance from the isolated pressure generation event to the walls of the system with free flow (drained) boundary conditions and u_0 is the velocity of a grain. When $De << 1$, isolated pressure generated within the granular system quickly diffuses through out the system, having no effect on the evolution of a slip event. We call this situation "fully drained" because no large pressure perturbations can occur, even locally. On the contrary, for $De >> 1$ the pressure generation from granular compaction and/or movement cannot flow from the area, which can significantly impact the effective stress on the system. We are interested in when fluid flow has an effect during earthquakes $(De \geq 1)$, that is, when fluid can neither flow too easily (such as at the boundaries) nor is it restricted too much where pressure diffusion cannot effect the surrounding system. We refer to this as "effectively undrained" to indicate that local pressure perturbations can be large.

To simulate slip events, our model setup is similar to Aharonov and Sparks [2004]: grains are bounded on the top and bottom by rough walls consisting of cohesive grains. The top wall has a constant effective confining stress applied to reflect natural fault zone conditions. Note that the applied stress on the walls is effective stress, in that it accounts

for an ambient uniform fluid pressure in the gouge that is in equilibrium with the damage zone. Therefore, calculated fluid pressures (P) are positive and negative perturbations to this equilibrium pressure. The bottom wall is held fixed, while the top wall and granular fault gouge are free to undergo displacement. The systems slip at velocities on the order of meters per second. The system is periodic (wrap-around) in the layer parallel direction. Although the images show a rectangular system, it is actually an unwrapped annulus, similar to a rotary shear experiment. Pressure perturbations in the damage zone are assumed to be zero $(P=0)$. In the following simulations, fluid is allowed to flow freely into and out of the walls.

It is important to note that all findings presented are non-dimensionalized. Velocities are scaled by the P-wave velocity of a grain, stresses are scaled by the Young's modulus of a grain, and lengths by the mean grain size. The material constants used for scaling can be found in Table 1.

The systems discussed are 200 grains wide in the layer parallel direction by approximately 50 grains in the layer perpendicular direction. The height of the system was chosen so that the middle of the gouge layer would be isolated from the effect of the free-flow boundary condition. If the gouge layer is too thin, fluid pressure is too easily relieved by flow through the boundaries. Flow through the boundaries can also affect where localization occurs in the gouge [*Bianco,* 2013]. If the box is tall enough, shear can concentrate in other locations where it is more difficult to relieve fluid pressures through boundary flow. In addition, the width of the box was picked so higher probabilities of multiple force chains were present. These are important because they support the bulk

stress of the system.

We slowly apply shear stress to the top wall by pulling a simulated spring at a constant velocity (V_s) (Figure 3). Aharonov and Sparks [2004] studied the behavior near the transition between stick-slip behavior and stable sliding. In this work, we build the stresses much more slowly to: 1) limit interference between slip rate and the rate of loading and 2) prevent fluid pressure deviations from affecting successive slip events. Once the frictional limit of the contacts is reached, an earthquake occurs as the top wall accelerates, relieving a portion of the shear stress applied to the system. Slip continues until the driving force is reduced enough that the frictional force is able to halt the top wall.

We have the ability to adjust elastic parameters to model a variety of slip displacements. The slip distances vary greatly, but are on the order of several tens to hundreds of grains. The systems slipped far enough so that many granular configurations were achieved, and force chains were created and destroyed during dynamic rearrangement. Unlike laboratory experiments, [*Liao et al*., 2014] an important aspect of our model is the lack of constraint on the slip rate: the granular system is not forced to adhere to imposed velocity functions.

An advantage of numerical models compared to laboratory experiments is that systems can be stopped and restarted at any time during a simulation. We simulate a slip event in a dry system, and then restart the system right before a slip event occurs, including fluid effects (Equations 12-20, Appendix C). This is acceptable because stress loading between events is so slow that no significant pressurizations occur as the system

approaches peak static stress. Thus, slip events that begin with a particular granular arrangement can be run dry (simulating very high gouge permeability or a “fully drained” system) and then with a lower permeability (so that the gouge is only “partially drained”) to see the effect of fluid flow. This allows us to directly compare the effect of fluid on the evolution of a slip event from two systems that originated with the identical granular packing.

An additional advantage of numerical models, some laboratory methods, is the ability to directly observe the sample undergo deformation, and in our case, to witness the fault core deform and pore fluid pressures arise and diminish. We record snap shots of our DEM model with fluid pressures shaded inside of all finite difference cells throughout an entire simulation. This allows us to view fluid flow caused by the granular matrix during an earthquake.

IV. RESULTS AND ANALYSIS

4.1 Slip Events in Fully Drained Simulations

We conducted a large number of simulations using the same constant confining stress $(\sigma = 24 \text{ MPa})$ with a variety of loading conditions applied to the top wall. The system is stressed much more slowly than Aharonov and Sparks [2004] as indicated by the boxes in loading space (Figure 4). A summary of the different elastic parameters used in each simulation can be found in Table 2.

Figure 5 is a sample from our large collection of fully drained simulations containing multiple slip events. The vertical axis of the top graph is normalized shear stress and the horizontal axis is dimensionless time. We define normalized shear stress as shear stress applied to the top wall, scaled by the constant applied confining stress. The model is initiated under a confining stress only; we apply a shear stress to the top wall of the system by slowly pulling a simulated spring at a fixed velocity. This is shown as a linear increase in stress from the origin to Time A. During this time period, force chains begin to take a preferential direction due to the application of shear stress. Once the system reaches the peak stress for this unique granular packing (Time A), it fails and the top wall displaces. This relieves applied shear stress until a new arrangement arises that can support the reduced shear stress. After the initial slip event, a number of other earthquakes occur between Times A and B, separated by approximately the same interval, and relieving a similar amount of stress (characteristic stress drop). There are 32

earthquakes in this plot as evident by the drop in shear stress. For example, the time period between the Times labeled B and C shows 13 earthquakes with almost identical stress drops. Again, in-between Times E and F, there is a repeated characteristic change in stress for each event. We find repetitive slip events consisting of similar stress drops to be characteristic of drained systems.

Figure 5 (bottom) shows top wall velocity normalized by the loading velocity for the same time period as the normalized stress figure. Throughout a simulation with multiple slip events, the time rate of change of displacement varies with each event. This occurs because each slip event begins with a unique granular packing that has a varying resistance to failure relative to other slip events. We find earthquakes that relieve the largest amount of shear stress, undergo displacement at the highest velocities (for example, Time D). In this figure, the average velocity is $V_{Average} = 9.28$. The relationship between large slip velocities and large stress drops can be explained by investigating Equation 3. For a given simulation the terms k_s and m_b control the period of the driving spring and are held constant with each slip event. The observed time of each slip event is well-explained by this spring period, as in Equation 3. Since slip time is fixed, to slip farther and faster, the term affecting the amplitude $(\Delta\mu)$ must be larger. Our full catalog of simulations consisting of multiple earthquakes can be found in Appendix A.

Figure 6 is a magnified version of a single slip event from a simulation consisting of multiple earthquakes. The velocity curve clearly resembles a sine wave with some high frequency fluctuations. Because of the contact model, our system has its own frequency

that it vibrates at while displacement is occurring and we infer the high frequency fluctuations imposed on the velocity to be from this. Figure 6 and Figure 7 reveal two very important results of fully drained systems: first, the occurrence times of slip events (characteristic slip time) is relatively constant as expected from the period in Equation 3, and second, the approximate solution to the spring-block slider model (Equation 3) is a good predictor for velocity curves in this DEM simulation.

4.2 Slip Events in Effectively Drained Systems

We find the amount of shear stress relieved during an event can vary greatly between drained and undrained events. Figure 7 (top) shows normalized shear stress versus time and the corresponding velocity (bottom) through time. In this figure, the drained system from Figure 5 is shown again, except the initial loading phase is not included. In contrast to the drained system, the undrained system has more earthquakes (43) in the same period, which reached lower peak velocities $\left(V_{Average} = 7.53\right)$. However, the undrained events are more variable and sometimes the fluid systems slip faster than the mean velocity for dry events. Unlike dry systems, there is not a characteristic stress drop associated with these saturated systems; instead they behave unpredictably, consisting of numerous small slip events.

We are able to directly compare the effect of fluid flow in high and low permeability events because we can restart slip events using the identical granular

packing; first using a system with a high permeability and then restarting the system at a point prior to slip with a lower permeability. We have done this drained vs. effectively undrained comparison experiment for 39 different slip events. The elastic parameters used in each simulation can be found in Table 3.

For identical granular arrangements, undrained systems always slip at a lower velocity than its drained counterpart. For example, Figure 8 shows the drained velocity curve from Figure 6, superimposed on the undrained version of the same slip event. Immediately noticeable is the peak velocity of the undrained system is only 61.5% of the dry system. The slip-time of the undrained simulation is longer relative to the drained system. These deviations in period and peak velocity from Equation 3 imply undrained events tend to diverge from the block-slider solution much more than drained systems.

The static strength of the undrained events is often different from the drained events. Type I events are those in which the undrained system fails before the drained system while in Type II events the undrained systems achieve a higher static strength. Figure 9 is a slip event where the undrained system failed before the drained system (Type I), that is, the undrained system has a lower static strength. At Time A, both the undrained and the drained systems support the same shear stress load (24% of the confining stress). Shortly after, some movement within the undrained system such as the breakdown of a force chain causes fluctuations in the local fluid pressures. In this example, local compaction likely created positive fluid pressures, lowering the effective confining stress, which weakened the system just enough to cause an earthquake. The drained system continues to strengthen beyond that of the undrained system because the

local compaction event did not weaken the system enough to cause failure (in the absence of fluid). Nine of 39 earthquake simulations behaved as Type I events.

More often, granular systems tend to dilate under shear stress as discussed below. When undrained granular materials dilate the effective confining stress acting on the system increases. This increase (according to Equation 1) strengthens the systems resistance to shear (static friction) and we refer to these as Type II cases. Of our 39 events, 30 were classified as Type II. Figure 10 displays an example of a Type II earthquake event. At Time A, the drained system and undrained system are under the identical shear stress. Immediately after this time, an earthquake occurs in the drained system, relieving shear stress between Times A and B. This indicates the static strength of this system is $\left(\tau/\sigma = 0.2193\right)$. Unlike the drained system, the undrained system strengthens beyond its counterpart by about $\tau/\sigma \approx 0.05$ or 2% more than the identical drained system before the event occurs. It is apparent that pressure generation during the loading phase played a role because the two systems did not achieve the same peak shear stress. Our full catalog of Type I and Type II events can be found in Appendix B.

The existence of these two types indicates that the static resistance to shear depends on the initial motion of the material, which will vary between different granular arrangements. Note that in both Type I and Type II cases, the stress drop is smaller than in the drained system, implying that in the resistance to shear during slip is always higher in the undrained system. The value and evolution of dynamic resistance to shear leads to complex slip behavior that is not reproduced in drained systems.

4.3 The Evolution of Complex Slip Events

Both Type I and Type II undrained events can have velocity curves that differ significantly from the block-slider prediction, and occur only in undrained slip events. Here, local pressure perturbations affect not only the timing of an event, but also the temporal evolution of the earthquake. These may consist of multiple events, where events terminate after a small amount of displacement and new events initiate in other locations of the fault gouge. From our catalog, 5 of 9 Type I events are sub-classified as Type I-C and 20 of 30 Type II events as Type II-C.

Figure 11 shows normalized shear stress versus time for a complex undrained system (Type II-C) and the identical drained system. As the two systems are stressed, the drained simulation reached static strength at Time A $\left(\tau/\sigma = 0.2148\right)$. At Time B, the undrained system exhibits its first significant earthquake resulting in a stress drop of $\Delta\tau/\sigma = 0.0027$. Contrary to the drained system, this earthquake consists of multiple small stress drops. The system is halted due to negative fluid pressure generation raising the effective normal stress and strengthening the granular system. It is not until Time C $\left(\tau/\sigma = 0.2285\right)$ that a slip similar in magnitude to the drained system occurs. During this event, there are six smaller isolated earthquakes in between Times C and D. These complex events are interpreted to be from fluid flow influencing different areas of the gouge to fail.

Figure 12 is one example of a complex top wall velocity for a undrained gouge zone. The velocity for the drained system follows the sine wave solution to a block-slider model. On the other hand, the undrained system shows multiple small earthquakes with little or no time between events. These small slips lack a characteristic slip period that can be predicted by Equation 3.

Six events from our full catalog are shown in Figure 13. On each plot the sloping red line indicates the loading rate of the top wall in the absence of a slip. These earthquakes exhibit interesting behaviors ranging from fault creep to episodic tremors. For example, Figure 13A had a small slip event at the beginning of the simulation. Following this, the gouge layer begins to creep. During this time, the system creeps at the same velocity as its' loading velocity, as evident by the horizontal stress curve. Figure 15B exhibits, although the creep that is slightly faster than the loading, resulting a very small gradual stress drop. The fault core eventually fails, resulting in a large stress drop. In Panel C, as the system attempts to fail, fluid pressures immediately lock the event. After more loading, the main event occurs. However, at the end of the event the system creeps. Eventually, the reduced pressures, which strengthened the system, diffuse and the core undergoes one smaller earthquake. Panel D shows a mixture of tremor-like and creep-like behavior. In the middle of the simulation there are two small stress drops separated by small intervals of loading followed by the main event. After this, the gouge layer returns to creep-like behavior. Panel E shows behavior further into the tremor regime. As the system is loaded to its' static strength, seven small stress drops occur. Figure 13F undergoes a number of tremors as stress is applied. During this period the

system is rarely stationary and instead has small discrete earthquakes accompanied with small stress drops relative to the primary stress drop at the end. These tremors are most likely due to fluid flow into neighboring areas of the gouge, halting a slip event in one location, and beginning a new event somewhere else.

V. DISCUSSION

5.1 Effect of Pore Fluid on Static Strength of Faults

We found that fluid can strengthen or weaken the static strength of a granular system. Of our simulations, 77% of undrained systems achieved a higher static strength. An explanation for the strengthening of the wet system is due to local and/or large-scale dilation of the granular network, increasing the effective confining stress acting on the grains. Generally, dilation occurs in isolated areas around force chains where grains rotate and roll relative to each other, increasing the local porosity.

5.2 Effect of Fluid on Dynamic Strength – Anatomy of a Slip Event

To investigate the effect of local pore fluid pressure perturbations on an earthquake, snapshots of fluid flow during a simulation are shown for a Type II-C event. Figure 14 shows a velocity function produced by a Type II-C event (blue curve), which started with the identical granular packing as the fully drained system (black curve). The shear stress applied on the top wall for the undrained system is shown in Figure 15A. Figure 15B shows a magnified version of the undrained system and is marked at various times of interest: (A) The onset of initial slip, (B) the peak velocity of initial slip, (C) termination of the initial slip, (D) initiation of the main slip event, (E) peak velocity of the main slip event, and (F) termination of the main event.

Figure 16 shows snapshots of the grain and pore pressure configurations at the labeled times in Figure 15B. Warm colors represent positive fluid pressure deviations while cooler shades are negative pressures. The outlines of the grains are absent, but the bold lines connecting the grain's centers represent the contact forces. The blocky shading of pore fluid pressures shows the size of the finite difference grid in calculating pressure. The shading in Figures 16A- 16F is scaled using different pressures to emphasize the pattern at each time, as the magnitude of pressure deviations varies greatly during the event.

Before Time A in Figure 15B, there were no pressure deviations in the fault core. Figure 16A marks the beginning of a low velocity slip event with the generation of positive fluid pressures marked with the dashed rectangle. In this Figure, the fluid pressures are scaled by 0.6 MPa. In the dashed rectangle (left), a collapse of a few grains generates a positive fluid pressure large enough to initiate this slip event. Surprisingly, a pressure generation of only 0.6 MPa or 2.5% of the constant confining pressure is enough to launch the system from a stuck phase to a slip phase. Fluid pressures quickly diffuse via pore spaces to other locations near the initial pore collapse as indicated by the arrows (Figure 16A). Another noteworthy point of this image is that even though compaction took place at the boundary of the system, where fluid can easily flow into the damage zone $(P = 0)$, pressures quickly diffused to the interior of the fault core as indicated by the arrows in the figure. According to this pressure snapshot, pervasive compaction is not required to incite a slip event. Instead, slip only requires very confined and localized fluid pressure generations that are much less than the applied normal stress.

By Time B (Figure 16 B) the majority of the system is dilating. Here the image is scaled by 4.8 MPa, a pressure still significantly less than that of the constant confining pressure. This strengthens the system enough to cause a rapid decrease in velocity. It is important to note that the bulk of the reduced pressures (blue) are concentrated around the force chains as outlined by the dashed rectangles. These pressures strengthen the system by increasing the effective confining stress on the chains and cause the slip event to begin to halt. While the majority of the core is dilating, there are a few locations where pore spaces are collapsing. However, they do not lower the systems resistance to shear enough to initiate the main earthquake. As a result, the dilated areas begin to shut down the slip event.

As slip decelerates to zero, the force chains are further rotated and the entire gouge layer dilated until slip is halted (Figure 16C). This generates a system spanning reduction in pore fluid pressures. In this figure, the pressure is scaled by 1.5 MPa or 6.25% of the constant applied confining stress. Large areas of reduced pressures exist around force chains with a couple smaller, localized areas of high pressures. All pressure fluctuations are the result of the prior dilation, because at this time the dilation rate should be near zero $\left(V_w \approx 0\right)$. Only a small displacement of ~10 grains has occurred by this time.

After Time C, the gouge layer equilibrates pore pressure. This corresponds to a relatively "quiet" time in the fault core where only slow displacement occurs. During this time, the top wall creeps and neither accumulates nor relieves any shear stress placed on the system (Figure 15B). Eventually, small portions of the system collapse, producing positive fluid pressures in a number of locations within the gouge zone (Figure 16D). In

Figure 16D, pore fluid pressures are scaled by 16 MPa – a substantial percentage (67%) of the constant applied confining force. Contrary to Figure 16A, two locations of the fault core compact, generating enough positive fluid pressures to initiate the main slip event.

During the peak velocity of the main slip event (Figure 16E), positive and negative pressure perturbations can be found in neighboring areas. These areas attempt to equilibrate in fluid pressures via fluid flow. As the top wall continues to relieve shear stress from displacement, grains rotate and roll, causing force chains to be formed and destroyed. In Figure 16E, the interwoven network of force chains are accompanied by negative fluid pressures (dilation), while positive pressures are associated with areas of little to no contact force. The pressures are scaled by 12 MPa, indicating movement of the matrix generates large pressure perturbations.

Eventually, enough shear stress is relieved from the top wall and/or enough negative fluid pressures formed to end the event (Figure 16F). Displacement is roughly 100 grain diameters since Time A. In Figure 16F, fluid pressures are scaled by 2.4 MPa or 10% of the constant confining pressure. Although there are well-organized positive fluid pressures, they don't generate enough pressure to continue the slip event. Figures 16B and 16F show that reduced fluid pressures don't have to occur everywhere in the gouge to slow or stop a slip event. The instantaneous dynamic strength of the system appears to be sensitive to the local pressure fluctuations, not system averages. Further, in systems that have both local pressure reductions and (larger) local pressure increases, the system appears stronger. This indicates that the reductions are the key to gouge strength evolution.

5.3 Quantifying the Dynamic Effects of Fluid Pressure During Slip

To quantify the temporal evolution of effectively undrained systems, we return to the force balance of the spring block slider model (Equation 2). The normal force is replaced by the effective normal force $\left(\sigma - P(t)\right)A$ where A is the cross sectional area of the layer:

$$\begin{aligned} m_b \frac{d^2x}{dt^2} &= \sigma A\mu_s + kV_s t - kx(t) - \left(\sigma - P^*(t)\right)A\mu_d(t) \\ m_b \frac{d^2x}{dt^2} &\approx \sigma A\mu_s - kx(t) - \left(\sigma - P^*(t)\right)A\mu_d(t) \end{aligned} \quad [5]$$

The spring-block slider model assumes friction instantaneously drops from a higher static value to a lower, constant dynamic value when slip occurs. However, we can treat dynamic friction as a possible function of time as well and solve for the overall shear resistance. Here, $\sigma\mu_s$ is the peak shear force exerted by the spring at the moment that slip begins $(t = 0)$. It is important to distinguish the fluid pressures. In Equation 18 (Appendix C), $P(t)$, is from the actual fluid pressures calculated in the finite difference grid. $P^*(t)$ Is a measurement of fluid pressure effects, i.e. pressures required to influence the system. This may correspond to a local pressure at the strongest part of the gouge. Equation 5 can be rearranged to measure the systems instantaneous resistance to shear from the displacement and by using a finite-difference approximation for the top walls' acceleration:

$$\mu_d(t)\left(\sigma - P^*(t)\right)A = \sigma A\mu_s - kx(t) - m_b\left(\frac{V_w(t+\Delta t) - V_w(t-\Delta t)}{2\Delta t}\right) \quad [6]$$

Note that for a perfectly drained system, $P \equiv 0$, so we can calculate the coefficient of dynamic friction directly:

$$\mu_d(t) = \frac{1}{\sigma A}\left[\sigma A \mu_s - kx(t) - m_b\left(\frac{V_w(t+\Delta t) - V_w(t-\Delta t)}{2\Delta t}\right)\right] \quad [7]$$

Figure 17 shows $\mu_d(t)$ for the drained slip event discussed in Figure 6. The vertical axis (left) is $\mu_d(t)$ while the other vertical axis is dimensionless velocity. This slip event was chosen because it is in good agreement with the approximate solution to the spring-block slider model, indicating $\mu_d(t)$ should be a constant. As the slip event is about to initiate, the system is at its' static strength $\left(\mu_s\sigma = 7.014 \times 10^{-5}\right)$. This is shown at early times where the friction curve is flat. During slip, there are small high frequency oscillations in top wall velocity, visible in Figure 17. These arise because the granular system itself behaves as an elastic material, in which vibrations are being stimulated by the collision of grains during slip. This gives rise to vibrations of the entire granular layer and the top wall at the natural frequency of the system. The high frequency of these small oscillations cause accelerations to dominate the μ_d signal. However, lower frequency signals correspond to real changes in the dynamic resistance of the layer. The spring-block slider model assumes μ_s immediately drops to μ_d, but Figure 17 shows that as slip begins, the friction value drops over some finite time period to a lower value. Apart from the high-frequency oscillations, the dynamic friction remains roughly constant at $\mu_d \approx 0.2204$ as we have already predicted based on the sine wave nature of the velocity curve.

In comparison, Figure 18 shows the undrained slip event presented in Section 5.2. The vertical axis (left) corresponds to slip resistance while the right axis measures the top wall velocity. Also on this figure is the static strength of the system (black line) and the average dynamic strength of the identical drained system (red line). Any fluctuations of resistance above or below these thresholds indicated fluid pressures and/or $\mu_d(t)$ affected the slip event by weakening or strengthening the system.

At Time A on Figure 18, the system starts at its' static strength $(\sigma\mu_s)$. As the wall begins to move, resistance of the system falls from a static value to roughly a dynamic value (black arrow) of the drained system, and the top wall accelerates.

At Time B, the resistance begins increasing, and continues until Time C at a value at or above the static strength. This strengthening must be caused by either a drop in fluid pressure due to a dilation of the granular system or an increase in the coefficient of dynamic friction from grain rearrangements. The strengthening is large enough that it forces the slip even to terminate, at which point the strength stays at about the static value. Thereafter, the top wall briefly stops but continues slipping at Time D. The interval between Times D and E marks a very intriguing part of the earthquake with regards to the dynamic resistance; the dynamic resistance hovers very closely to the original static strength of the system. During this period, the top wall moves at a velocity very close to the loading velocity. This suggests the system has entered a stable creep regime; fluid strengthening that is preventing the earthquake from continuing. Note from Figure 17 and the block-slider model, that when μ_d approaches μ_s sliding should become stable.

Following Time E, the dynamic resistance of the system rapidly decreased until Time F. This weakens the system enough to initiate the main earthquake as the top wall accelerates. After Time F, the dynamic resistance of the system fluctuates during the main portion of the slip. The system predominantly shows dynamic weakening throughout the main event, slipping at a strength that is near or below the dynamic strength of the drained system. However, a number of times the system's resistance increases beyond that of the static strength; each time this happens the gouge quickly decelerates, never reaching a peak velocity as seen in drained slips. In addition, the resistance of the system typically doesn't fall between the forecasted values of $\sigma\mu_s$ and $\sigma\mu_d$. Because $\mu_d(t)$ doesn't fluctuate much in the drained system, these large changes in dynamic resistance that reach beyond that of these thresholds shows fluid pressures are the dominant mechanism influencing the resistance of the system. At the end of the earthquake, the resistance returns to the static strength as a result of Equation 7.

VI. SUMMARY AND CONCLUSIONS

We have run many Discrete Element (DEM) simulations of fault gouge that has been stressed to near failure, to explore the effect of pore-fluid flow and pressure generation during deformation. By varying the average gouge permeability, we can simulate an earthquake using the same granular packing under "fully drained" (fluid flows so easily that no pressure perturbations are generated) and "effectively undrained" (fluid flows slowly enough that local perturbations significantly affect the effective stress on granular contacts).

Two primary classes of individual slip events were made: Type I and Type II. We found nine Type I and 30 Type II. Because Type II events achieved a higher static strength than the drained simulations, this showed fluid flow played a role in the static strength of the system. Type I were earthquakes in which the effectively undrained simulation reached a lower static strength than its' drained counterpart. This implied the strength of the system (fluid pressure generation) is sensitive to the initial movement of the granular skeleton. Two subcategories were also defined: Type I-C and Type II-C. These events exhibited complex behavior during an earthquake including: abrupt terminations of slip, rapid fluctuating velocity curves, creep behavior and episodes of repeated small slip events (episodic tremor).

Drained simulations showed good agreement with the prediction of the block-slider model, implying the dynamic coefficient of friction is roughly constant during a slip event. In Section 5.2 we showed the unpredictable behavior of Type I-C and Type II-

C could be explained by local pressure perturbations from granular movement. Lastly, the dynamic resistance of complex events was extracted; indicating large fluctuations were almost exclusively due to fluid effects.

In summary,

- Fluid pressures tended to increase the static strength of the fault core, but not always.
- Pressure reductions played a dominant role in stability and evolution of a slip event.
- Pressure reductions slowed the slip events relative to the drained simulations.
- Small pressure perturbations are able to initiate and terminate simulated earthquakes.
- The dynamic resistance of complex events is primarily controlled by fluid flow, and not a variable coefficient of dynamic friction.

Future work could include: A) creating a phase diagram to determine when complex behavior will arise as a function of the mean permeability and confining stress, and B) revisiting the extraction of dynamic resistance using a notch filter to attenuate the natural frequency such that the low frequency of the component is more visible.

REFERENCES

Aharonov, E., and D. Sparks (1999), Rigidity phase transition in granular packings, Physical Review E, 60(6), 6890-6896, doi: 10.1103/Phys Rev E.60.6890.

Aharonov, E., and D. Sparks (2002), Shear profiles and localization in simulations of granular materials, Physical Review E, 65(5), doi: 10.1103/Phys Rev E.65.051302.

Aharonov, E., and D. Sparks (2004), Stick-slip motion in simulated granular layers, Journal of Geophysical Research-Solid Earth, 109(B9), doi: 10.1029/2003JB002597.

Bianco, R. (2013), The effects of fluid flow on shear localization and frictional strength from dynamic models of fault gouge during earthquakes, 78 pp, M.S. Thesis, Texas A&M University, College Station, Texas.

Byerlee, J., V. Mjachkin, R. Summers, and O. Voevoda (1978), Structures developed in fault gouge during stable sliding and stick-slip, Tectonophysics, 44(1-4), 161-171, doi: 10.1016/0040-1951(78)90068-9.

Chester, F., and J. Logan (1987), Composite planar fabric of gouge from the Punchbowl Fault, California, Journal of Structural Geology, 9(5-6), 621-634, doi: 10.1016/0191-8141(87)90147-7.

Ciamarra, M., E. Lippiello, L. de Arcangelis, and C. Godano (2011), Statistics of slipping event sizes in granular seismic fault models, EuroPhysics Letters, 95(5), doi: 10.1209/0295-5075/95/54002.

Cundall, P., and O. Strack (1979), Discrete numerical-model for granular assemblies, Geotechnique, 29(1), 47-65.

Daniels, K., and N. Hayman (2008), Force chains in seismogenic faults visualized with photoelastic granular shear experiments, Journal of Geophysical Research-Solid Earth, 113(B11), doi: 10.1029/2008JB005781.

Daub, E., M. Manning, and J. Carlson (2008), Shear strain localization in elastodynamic rupture simulations, Geophysical Research Letters, 35(12), doi: 10.1029/2008GL033835.

Engelder, J., J. Logan, and J. Handin (1975), Sliding characteristics of sandstone on quartz fault-gouge, Pure and Applied Geophysics, 113(1-2), 69-86, doi: 10.1007/BF01592900.

Goren, L., E. Aharonov, D. Sparks, and R. Toussaint (2011), The Mechanical coupling of fluid-filled granular material under shear, Pure and Applied Geophysics, 168(12), 2289-2323, doi: 10.1007/s00024-011-0320-4.

Guo, P. (2012), Critical length of force chains and shear band thickness in dense granular materials, Acta Geotechnica, 7(1), 41-55, doi: 10.1007/s11440-011-0154-3.

Hayakawa, H. (1999), Simple model for granular friction, Physical Review E, 60(4), 4500-4504, doi: 10.1103/Phys Rev E.60.4500.

Iwashita, K., and M. Oda (1998), Rolling resistance at contacts in simulation of shear band development by DEM, Journal of Engineering Mechanics-Asce, 124(3), 285-292, doi: 10.1061/(ASCE)0733-9399(1998)124:3(285).

Karner, S., and C. Marone (1998), The effect of shear load on frictional healing in simulated fault gouge, Geophysical Research Letters, 25(24), 4561-4564, doi: 10.1029/1998GL900182.

Katsumata, A., and N. Kamaya (2003), Low-frequency continuous tremor around the Moho discontinuity away from volcanoes in the southwest Japan, Geophysical Research Letters, 30(1), doi: 10.1029/2002GL015981.

Leoni, F., A. Baldassarri, F. Dalton, A. Petri, G. Pontuale, and S. Zapperi (2011), Friction memory in the stick-slip of a sheared granular bed, Journal of Non-Crystalline Solids, 357(2), 749-753, doi: 10.1016/j.jnoncrysol.2010.07.046.

Liao, Z., J. Chang, and Z. Reches (2014), Fault strength evolution during high velocity friction experiments with slip-pulse and constant-velocity loading, Earth and Planetary Science Letters, 406, 93-101, doi: 10.1016/j.epsl.2014.09.010.

Majmudar, T., and R. Behringer (2005), Contact force measurements and stress-induced anisotropy in granular materials, Nature, 435(7045), 1079-1082, doi: 10.1038/nature03805.

Marone, C. (1998), Laboratory-derived friction laws and their application to seismic faulting, Annual Review of Earth and Planetary Sciences, 26, 643-696, doi: 10.1146/annurev.earth.26.1.643.

Marone, C., C. Raleigh, and C. Scholz (1990), Frictional behavior and constitutive modeling of simulated fault gouge, Journal of Geophysical Research-Solid Earth and Planets, 95(B5), 7007-7025, doi: 10.1029/JB095iB05p07007.

Mitchell, T., Y. Ben-Zion, and T. Shimamoto (2011), Pulverized fault rocks and damage asymmetry along the Arima-Takatsuki Tectonic Line, Japan, Earth and Planetary Science Letters, 308(3-4), 284-297, doi: 10.1016/j.epsl.2011.04.023.

Nasuno, S., A. Kudrolli, and J. Gollub (1997), Friction in granular layers: Hysteresis and precursors, Physical Review Letters, 79(5), 949-952, doi: 10.1103/PhysRevLett.79.949.

Nur, A., and J. Byerlee (1971), Exact effective stress law for elastic deformation of rock with fluids, Journal of Geophysical Research, 76(26), 6414-&, doi: 10.1029/JB076i026p06414.

Obara, K. (2002), Nonvolcanic deep tremor associated with subduction in southwest Japan, Science, 296(5573), 1679-1681, doi: 10.1126/science.1070378.

Radjai, F., S. Roux, and J. Moreau (1999), Contact forces in a granular packing, Chaos, 9(3), 544-550, doi: 10.1063/1.166428.

Rathbun, A., F. Renard, and S. Abe (2013), Numerical investigation of the interplay between wall geometry and friction in granular fault gouge, Journal of Geophysical Research-Solid Earth, 118(3), 878-896, doi: 10.1002/jgrb.50106.

Sleep, N., and M. Blanpied (1992), Creep, Compaction and the weak rheology of major faults, Nature, 359(6397), 687-692, doi: 10.1038/359687a0.

Sutherland, R., et al. (2012), Drilling reveals fluid control on architecture and rupture of the Alpine fault, New Zealand, Geology, 40(12), 1143-1146, doi: 10.1130/G33614.1.

Terzaghi, K. (1943), Theoretical Soil Mechanics, edited, John Wiley, New York.

Tordesillas, A., M. Muthuswamy, M. Nakagawa, and S. Luding (2009), Stick-slip and force chain buckling, Powders and Grains 2009, 1145, 313-316.

Volfson, D., L. Tsimring, and I. Aranson (2004), Stick-slip dynamics of a granular layer under shear, Physical Review E, 69(3), doi: 10.1103/PhysRevE.69.031302.

APPENDIX A

TABLES

Table 1. Dimensional material constants used in this study.

Symbols	Description	Values
β	Fluid compressibility	$4.5\times10^{-10}\,Pa^{-1}$
η	Fluid viscosity	$10^{-3}\,Pa\,s$
ρ_f	Pore fluid density	$1000\ kg/m^3$
ρ_s	Bulk density of grains	$2460\ kg/m^3$
μ	Friction coefficient	0.5
d	Grain diameter	$5\times10^{-4}\,m$
E	Young's Modulus	$8\times10^{10}\ Pa$
υ	Poisson's Ratio	0.2

Table 2. Dimensionless elastic parameters used in long simulations.

RUN	Spring Constant	Normal Force	Loading Velocity	Permeability
Run 4 Dry	5 X 10^{-7}	3 X 10^{-4}	1 X 10^{-5}	N/A
Run 5 Dry	5 X 10^{-7}	3 X 10^{-4}	5 X 10^{-6}	N/A
Run 5 Wet	5 X 10^{-7}	3 X 10^{-4}	5 X 10^{-6}	1 X 10^{-5}
Run 7 Dry	3 X 10^{-8}	3 X 10^{-4}	2 X 10^{-5}	N/A
Run 8 Dry	5 X 10^{-7}	3 X 10^{-4}	5 X 10^{-6}	N/A
Run 8 Wet	5 X 10^{-7}	3 X 10^{-4}	5 X 10^{-6}	1 X 10^{-5}
Run 14 Dry	1 X 10^{-7}	3 X 10^{-4}	5 X 10^{-5}	N/A
Run 14 Wet	1 X 10^{-7}	3 X 10^{-4}	5 X 10^{-5}	1 X 10^{-5}
Run 15 Dry	8 X 10^{-8}	3 X 10^{-4}	5 X 10^{-6}	N/A
Run 16 Dry	3 X 10^{-8}	3 X 10^{-4}	2 X 10^{-6}	N/A
Run 17 Dry	5 X 10^{-7}	3 X 10^{-4}	5 X 10^{-6}	N/A
Run 18 Dry	7 X 10^{-8}	3 X 10^{-4}	9 X 10^{-6}	N/A
Run 18 Wet	7 X 10^{-8}	3 X 10^{-4}	9 X 10^{-6}	1 X 10^{-5}
Run 19 Dry	1 X 10^{-7}	3 X 10^{-4}	3 X 10^{-6}	N/A

Table 2 Continued.

Run	Spring Constant	Normal Force	Loading Velocity	Permeability
Run 20 Dry	5×10^{-8}	3×10^{-4}	1×10^{-5}	N/A
Run 21 Dry	9×10^{-8}	3×10^{-4}	3×10^{-6}	N/A
Run 22 Dry	1×10^{-7}	3×10^{-4}	7.5×10^{-6}	N/A
Run 22 Wet	1×10^{-7}	3×10^{-4}	7.5×10^{-6}	1×10^{-5}
Run 23 Dry	9×10^{-8}	3×10^{-4}	1×10^{-5}	N/A
Run 23 Wet	9×10^{-8}	3×10^{-4}	1×10^{-5}	1×10^{-5}
Run 24 Dry	7×10^{-8}	3×10^{-4}	3×10^{-5}	N/A

Table 3. Dimensionless elastic parameters used in drained vs. undrained events.

RUN	TYPE	Spring Constant	Normal Force	Loading Velocity	Permeability
Run 7 Dry Restart Slip3	II-C	3×10^{-8}	3×10^{-4}	2×10^{-6}	1×10^{-5}
Run 7 Dry Restart Slip5	I-C	3×10^{-8}	3×10^{-4}	2×10^{-6}	1×10^{-5}
Run 7 Dry Restart Slip7	I-C	3×10^{-8}	3×10^{-4}	2×10^{-6}	1×10^{-5}
Run 14 Dry Restart Slip2	II	5×10^{-8}	3×10^{-4}	5×10^{-6}	1×10^{-5}
Run 14 Dry Restart Slip4	II-C	7.5×10^{-8}	3×10^{-4}	5×10^{-6}	1×10^{-5}
Run 14 Dry Restart Slip5	I	5×10^{-8}	3×10^{-4}	5×10^{-6}	1×10^{-5}
Run 15 Dry Restart6 Slip1	II-C	8×10^{-8}	3×10^{-4}	5×10^{-6}	1×10^{-5}
Run 15 Dry Restart6 Slip2	II-C	8×10^{-8}	3×10^{-4}	5×10^{-6}	1×10^{-5}
Run 15 Dry Restart6 Slip3	I	8×10^{-8}	3×10^{-4}	5×10^{-6}	1×10^{-5}
Run 18 Dry Restart Slip2	II	7×10^{-8}	3×10^{-4}	9×10^{-6}	1×10^{-5}
Run 18 Dry Restart Slip3	II-C	7×10^{-8}	3×10^{-4}	9×10^{-6}	1×10^{-5}
Run 18 Dry Restart Slip4	II-C	7×10^{-8}	3×10^{-4}	9×10^{-6}	1×10^{-5}
Run 20 Dry Restart3 Slip2	II	5×10^{-8}	3×10^{-4}	1×10^{-5}	1×10^{-5}
Run 20 Dry Restart3 Slip3	II-C	5×10^{-8}	3×10^{-4}	1×10^{-5}	1×10^{-5}
Run 20 Dry Restart3 Slip4	I	5×10^{-8}	3×10^{-4}	1×10^{-5}	1×10^{-5}
Run 21 Dry Restart Slip1	II-C	9×10^{-8}	3×10^{-4}	8×10^{-6}	1×10^{-5}
Run 21 Dry Restart Slip2	I-C	9×10^{-8}	3×10^{-4}	8×10^{-6}	1×10^{-5}
Run 21 Dry Restart Slip4	II-C	9×10^{-8}	3×10^{-4}	8×10^{-6}	1×10^{-5}
Run 21 Dry Restart Slip5	II-C	9×10^{-8}	3×10^{-4}	8×10^{-6}	1×10^{-5}
Run 21 Dry Restart Slip6	II	9×10^{-8}	3×10^{-4}	8×10^{-6}	1×10^{-5}

Table 3 Continued.

RUN	TYPE	Spring Constant	Normal Force	Loading Velocity	Permeability
Run 21 Dry Restart Slip8	I-C	9×10^{-8}	3×10^{-4}	8×10^{-6}	1×10^{-5}
Run 22 Dry Slip t=3E7	II	1×10^{-7}	3×10^{-4}	7.5×10^{-6}	1×10^{-5}
Run 22 Dry Slip t=4.65E7	II-C	1×10^{-7}	3×10^{-4}	7.5×10^{-6}	1×10^{-5}
Run 22 Dry Slip1	II-C	1×10^{-7}	3×10^{-4}	7.5×10^{-6}	1×10^{-5}
Run 23 Dry Slip t=1.3E7	II	9×10^{-8}	3×10^{-4}	1×10^{-5}	1×10^{-5}
Run 23 Dry Slip1	II-C	9×10^{-8}	3×10^{-4}	1×10^{-5}	1×10^{-5}
Run 24 Dry Slip2	I-C	5×10^{-8}	3×10^{-4}	1×10^{-5}	1×10^{-5}
Run 24 Dry Slip3	II	5×10^{-8}	3×10^{-4}	1×10^{-5}	1×10^{-5}
Run 24 Dry Slip4	II-C	5×10^{-8}	3×10^{-4}	1×10^{-5}	1×10^{-5}
Run 24 Dry Slip5	II	5×10^{-8}	3×10^{-4}	1×10^{-5}	1×10^{-5}
Run 24 Dry Slip6	I	5×10^{-8}	3×10^{-4}	1×10^{-5}	1×10^{-5}
Run 27 Dry Slip1	II-C	8×10^{-8}	3×10^{-4}	3×10^{-5}	1×10^{-5}
Run 27 Dry Slip2	II-C	8×10^{-8}	3×10^{-4}	3×10^{-5}	1×10^{-5}
Run 27 Dry Slip3	II-C	8×10^{-8}	3×10^{-4}	3×10^{-5}	1×10^{-5}
Run 27 Dry Slip4	II-C	8×10^{-8}	3×10^{-4}	3×10^{-5}	1×10^{-5}
Run 27 Dry Slip5	II-C	8×10^{-8}	3×10^{-4}	3×10^{-5}	1×10^{-5}
Run 27 Dry Slip6	II	8×10^{-8}	3×10^{-4}	3×10^{-5}	1×10^{-5}
Run 27 Dry Slip7	II	8×10^{-8}	3×10^{-4}	3×10^{-5}	1×10^{-5}
Run 28 Dry Slip2	II-C	6×10^{-8}	3×10^{-4}	1×10^{-5}	1×10^{-5}

APPENDIX B

FIGURES

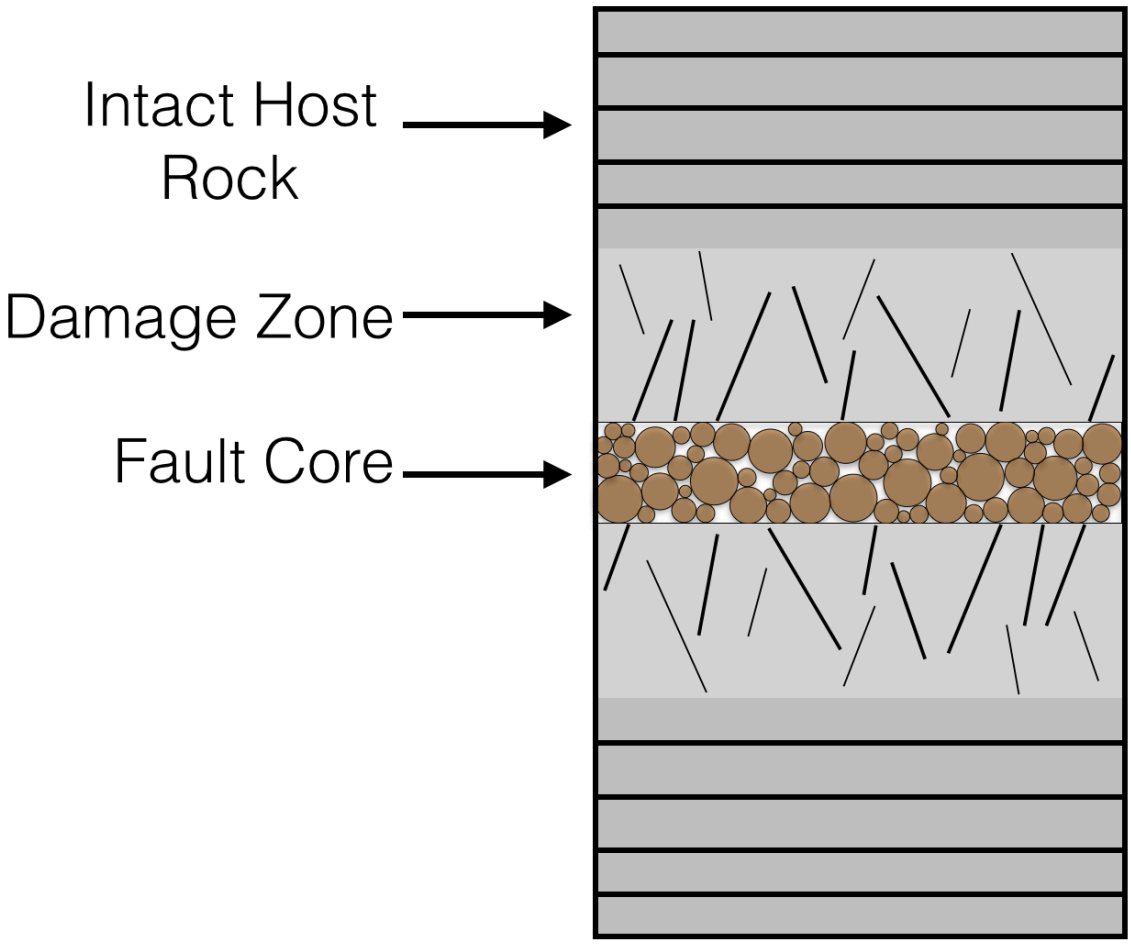

Figure 1. Anatomy of a fault zone. Three main components comprise a fault: fault core surrounded by a damage zone that is encompassed in country rock. The relative permeabilities of these range from low (country rock) to high (damage zone) with fault core lying between the two.

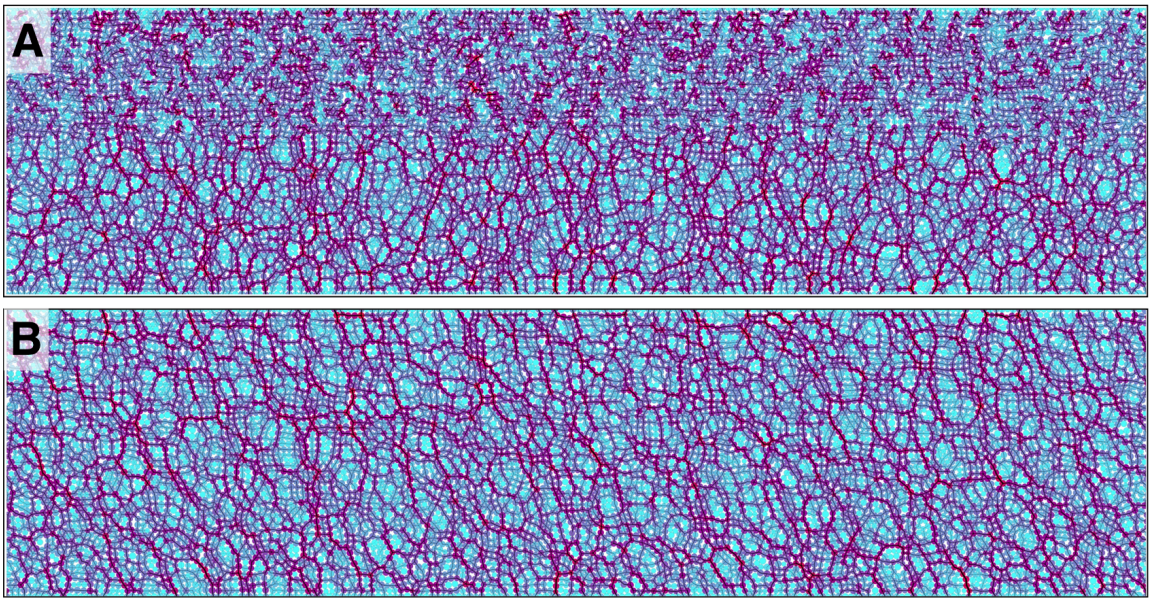

Figure 2. Force chains in a system with only confining stress applied – chains are randomly orientated (top). Granular system under a shear stress (bottom). Force chains form when a right lateral shear stress has been applied. Grains are colored according to their total contact force.

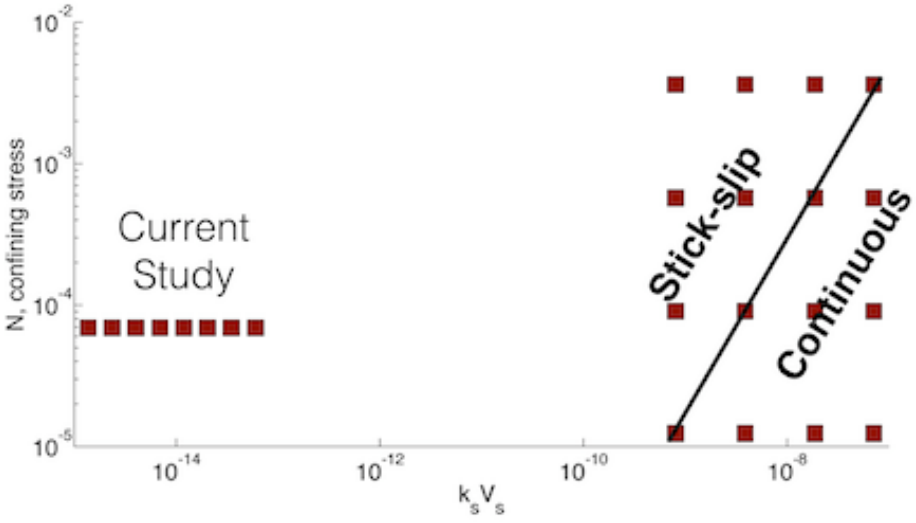

Figure 3. Phase diagram showing the transistion from stick-slip (unstable) to continuous (stable) sliding in fully drained (dry) simulations. Maroon boxes mark locations of conditions used in this study. Note the conditions used here are orders of magnitude farther into stick-slip space than those used by Aharonov & Sparks [2004].

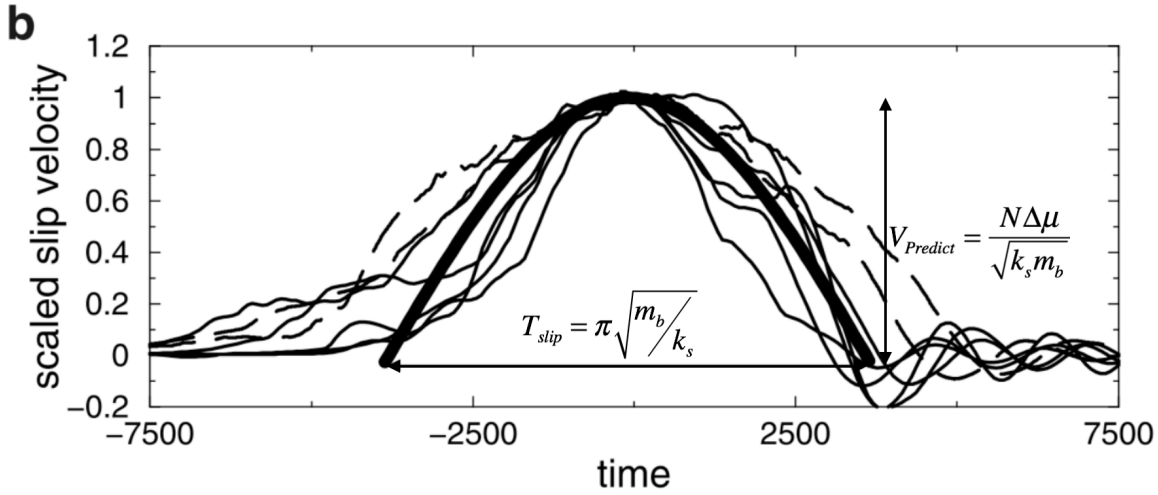

Figure 4. Dimensionless scaled slip velocity versus dimensionless time from a number of experiments conducted by Aharonov & Sparks [2004]. This shows granular fault gouge simulations approximately agrees with the predicted solution to the spring-block slider model (thick line). There is also a characteristic period associated with each slip (Tslip).[1]

[1] Reprinted from "Stick-slip motion in simulated granular layers" by Einat Aharonov and David Sparks, 2004. *Journal of Geophysical Research*, Vol. 109, 1-12, Copyright 2004 by the American Geophysical Union.

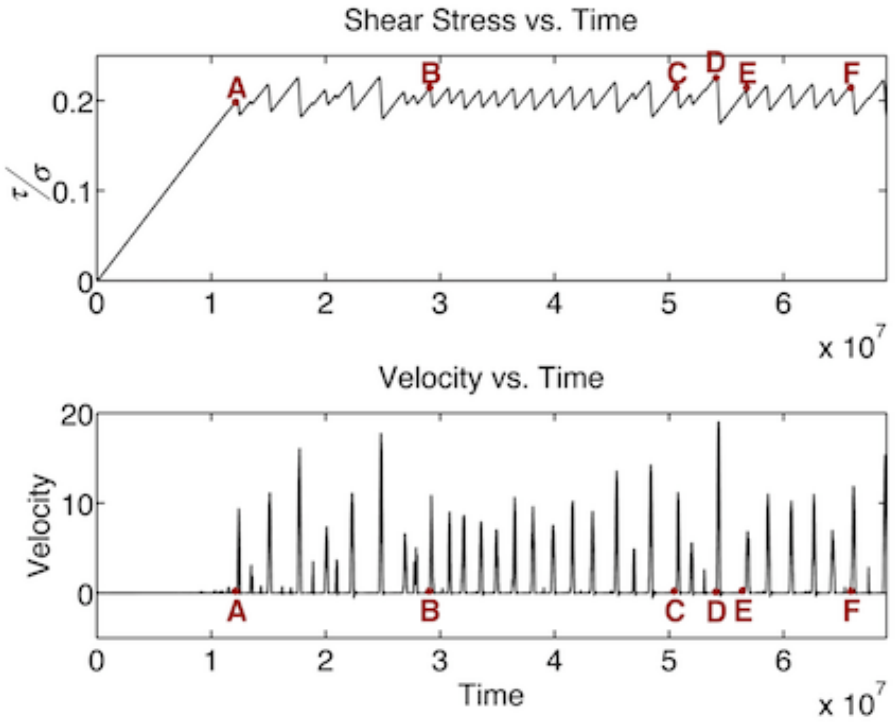

Figure 5. Applied shear stress normalized by the constant effective confining stress versus dimensionless time (top) and dimensionless velocity versus dimensionless time (bottom) for a drained system consisting of multiple events.

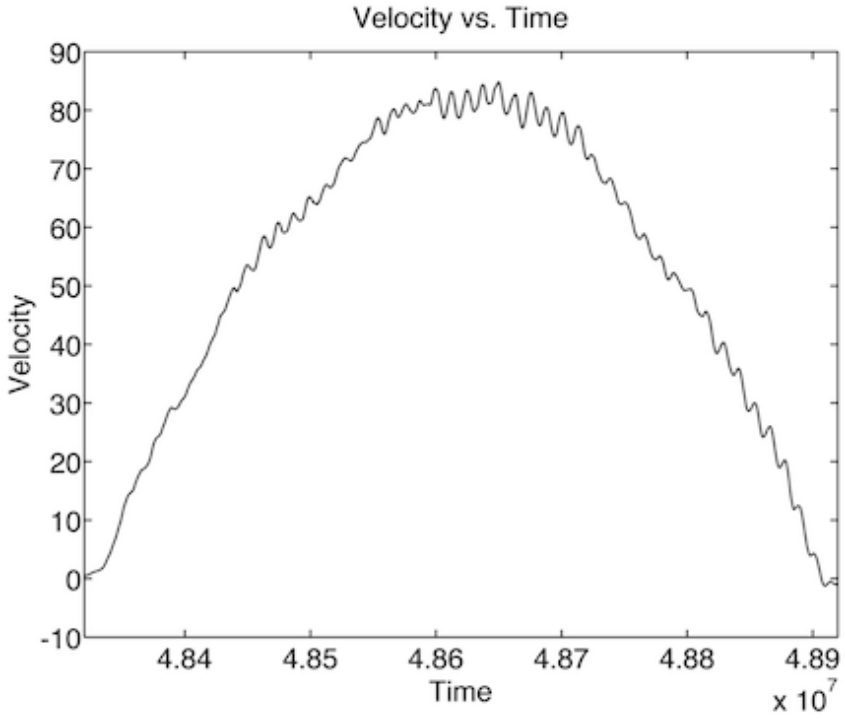

Figure 6. Dimensionless velocity versus dimensionless time from a slip event in a drained system. This slip event resembles a near perfect sine wave, in agreement with Equation 3. High frequency oscillations are inferred to be at the natural frequency of the granular packing.

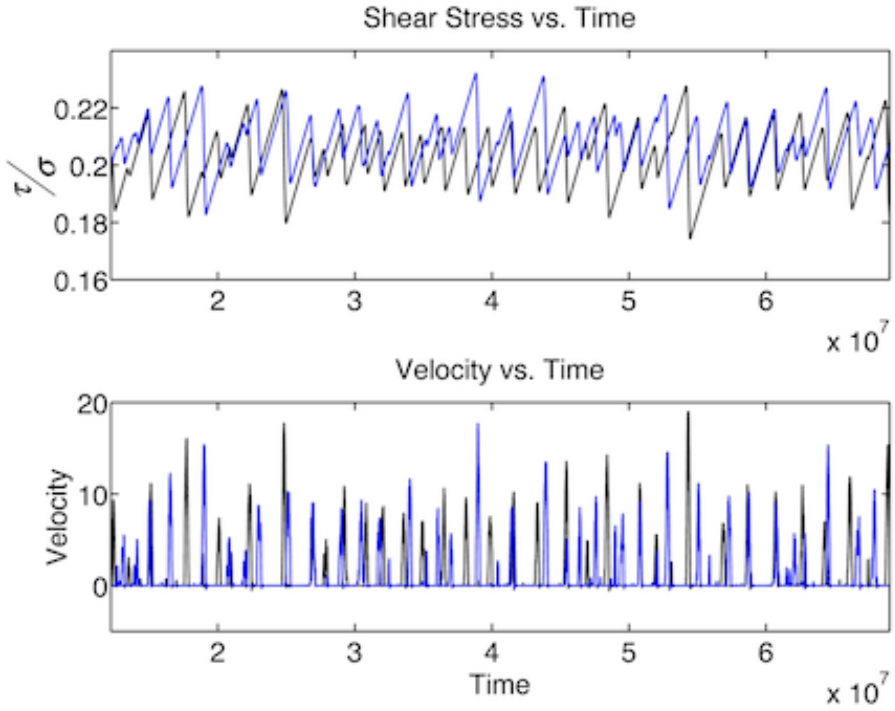

Figure 7. Applied shear stress normalized by the constant effective confining stress versus dimensionless time (top) and dimensionless velocity versus dimensionless time. The black curves represent drained conditions while the blue corresponds to an undrained system. Both systems began with the identical granular packing and are simulated using the same elastic parameters. Undrained systems tend to have more earthquakes over the same time period as dry systems, and on average, slip at lower velocities.

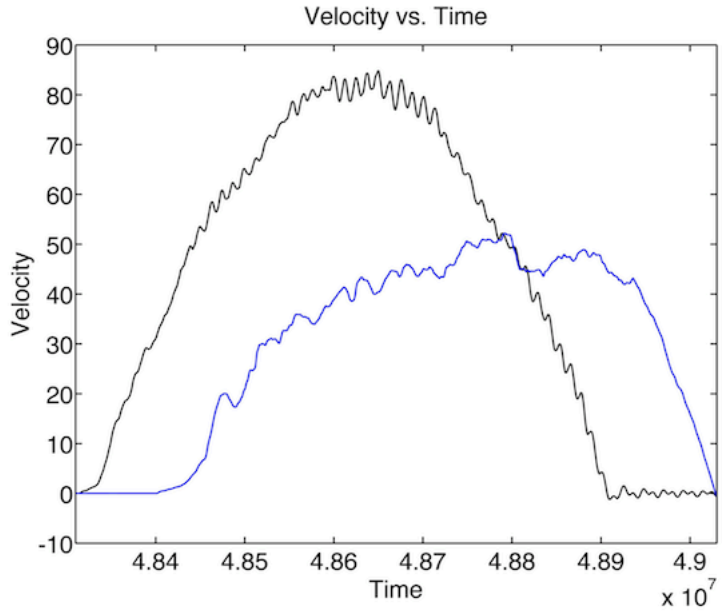

Figure 8. Dimensionless velocity versus dimensionless time for a drained (black) and undrained (blue) system that began with the same granular configuration. The drained system is the same as the one presented in Figure 6. Undrained systems have a period and velocity curve that doesn't agree with the expected solution to a spring-block slider model.

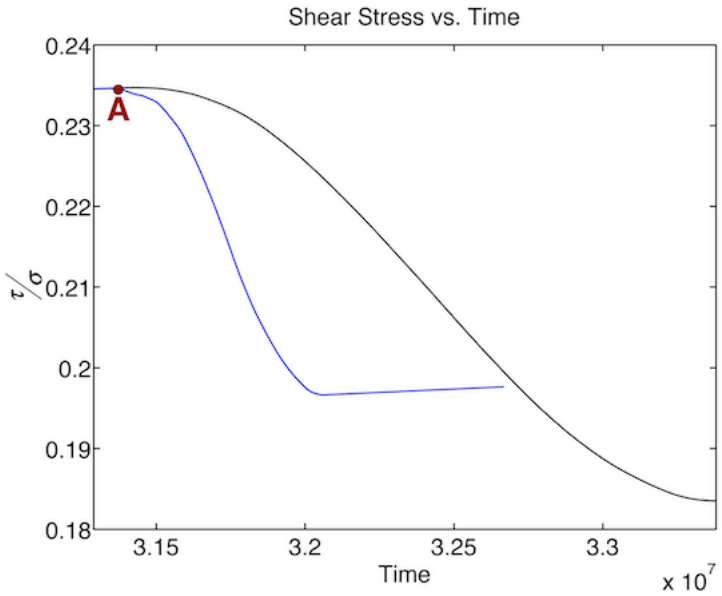

Figure 9. Applied shear stress normalized by the constant effective confining stress versus dimensionless time for a drained (black) and undrained (blue) system. This is a Type I undrained event, characterized by a lower static strength than the matching drained event.

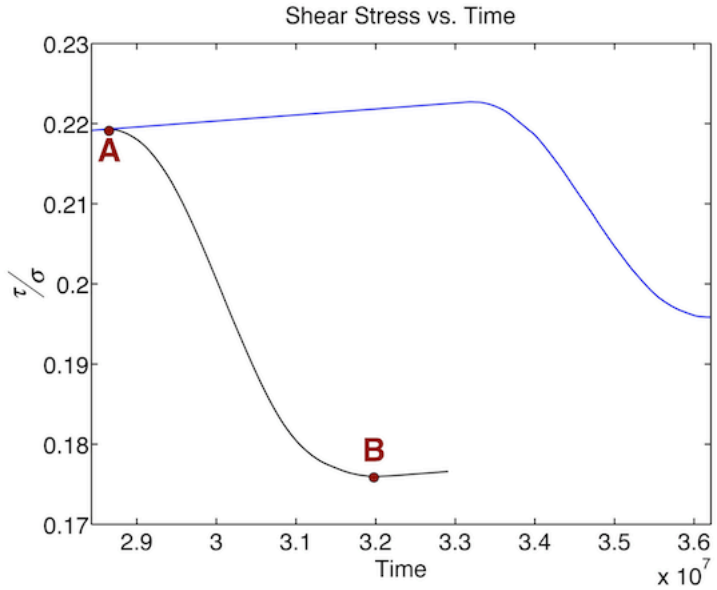

Figure 10. Applied shear stress normalized by the constant effective confining stress versus dimensionless time for a drained (black) and undrained (blue) system. This is a Type II undrained event, characterized by a higher static strength than the matching drained event.

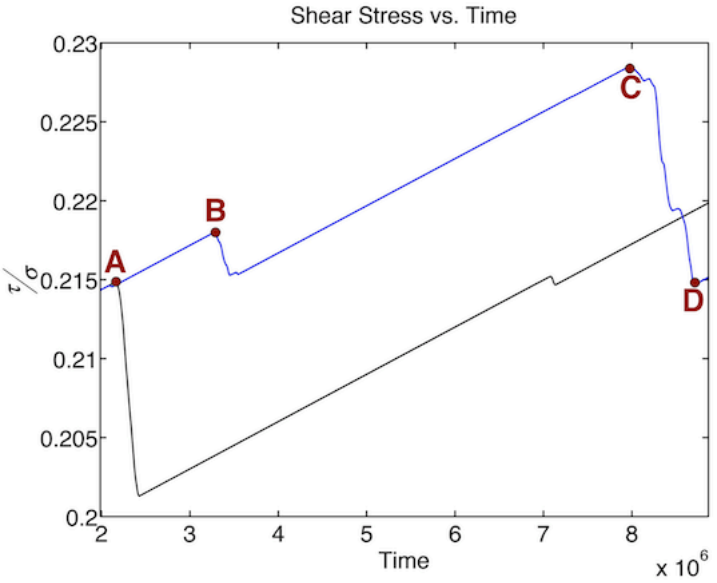

Figure 11. Applied shear stress normalized by the constant effective confining stress versus dimensionless time for a drained (black) and undrained (blue) system. This is a Type II-C undrained event, characterized by a higher static strength than the matching drained event and having a velocity curve that doesn't agree with the block-slider model.

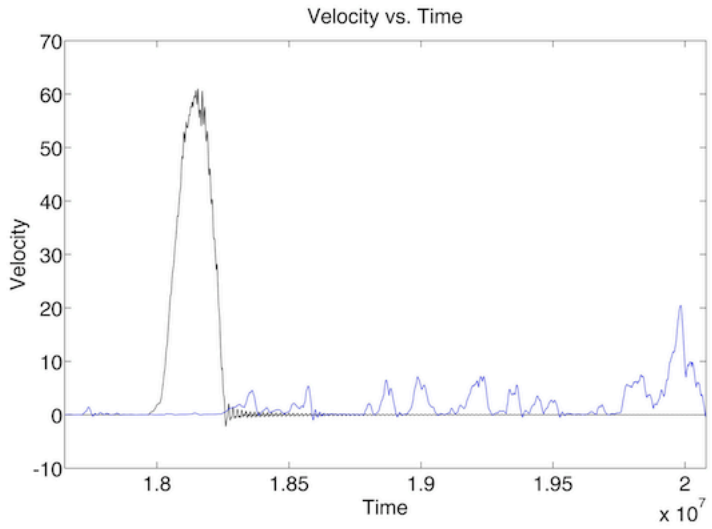

Figure 12. Dimensionless velocity versus dimensionless time for a drained (black) and undrained (blue) simulation of a Type II-C event. Note the undrained system underwent numerous small earthquakes while the drained simulation produced a velocity curve in agreement with the block-slider model.

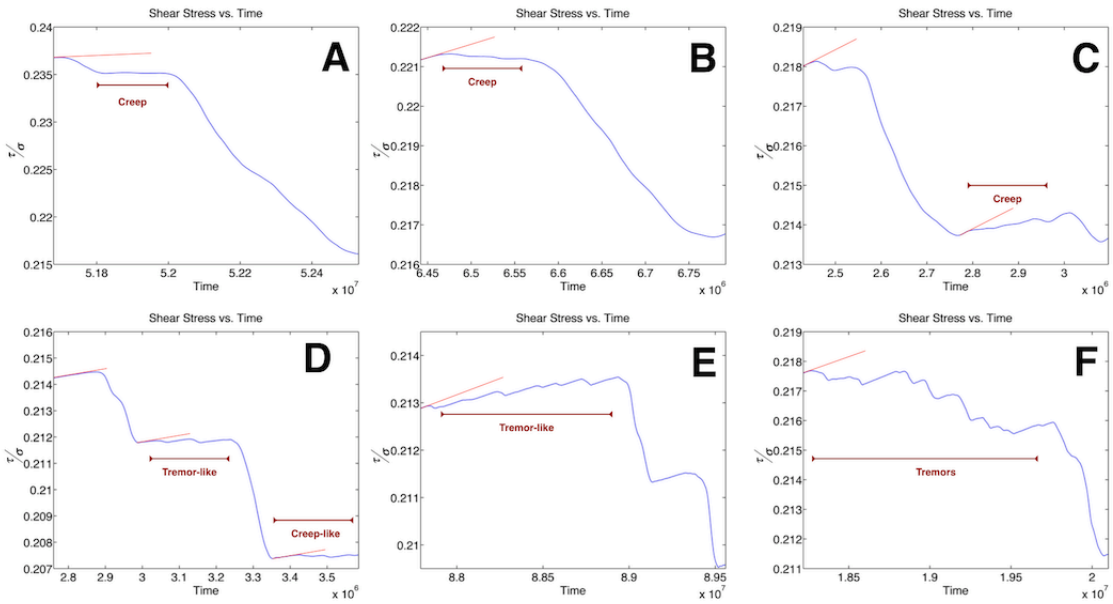

Figure 13. Six selected undrained events that exhibited creep-like and tremor-like behavior.

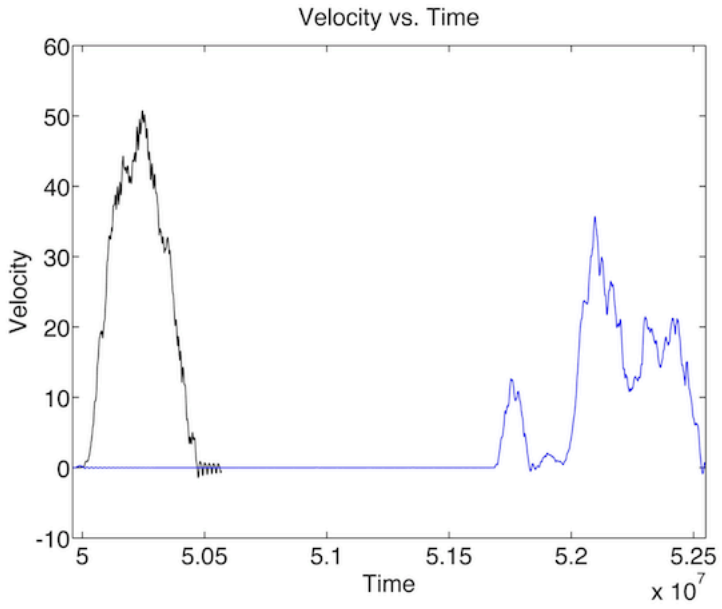

Figure 14. Dimensionless velocity versus dimensionless time for a drained (black) and undrained (blue) simulation of a Type II-C event.

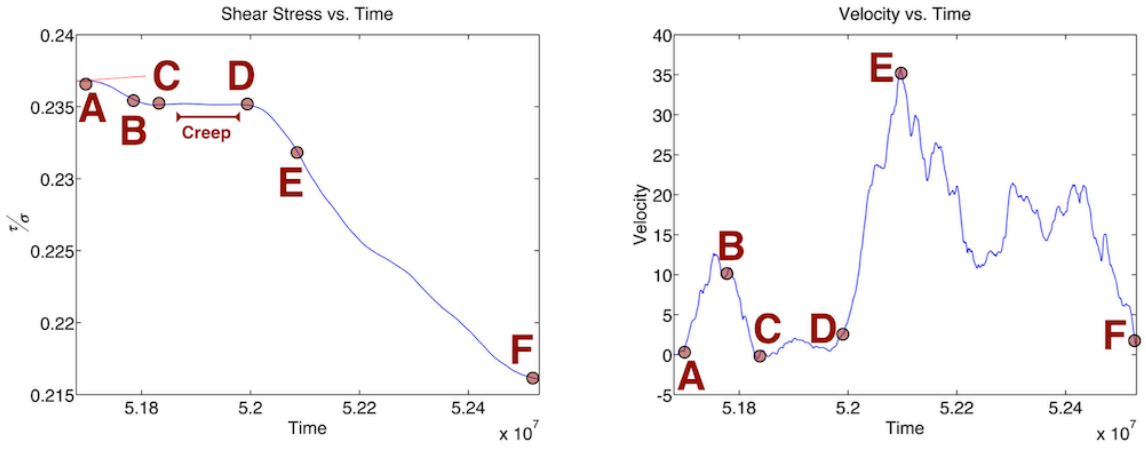

Figure 15. (a) Applied shear stress normalized by the constant effective confining stress versus dimensionless time and (b) dimensionless velocity versus dimensionless time for an undrained simulation of a Type II-C event. (b) is a magnified version of the undrained slip event shown in Figure 14.

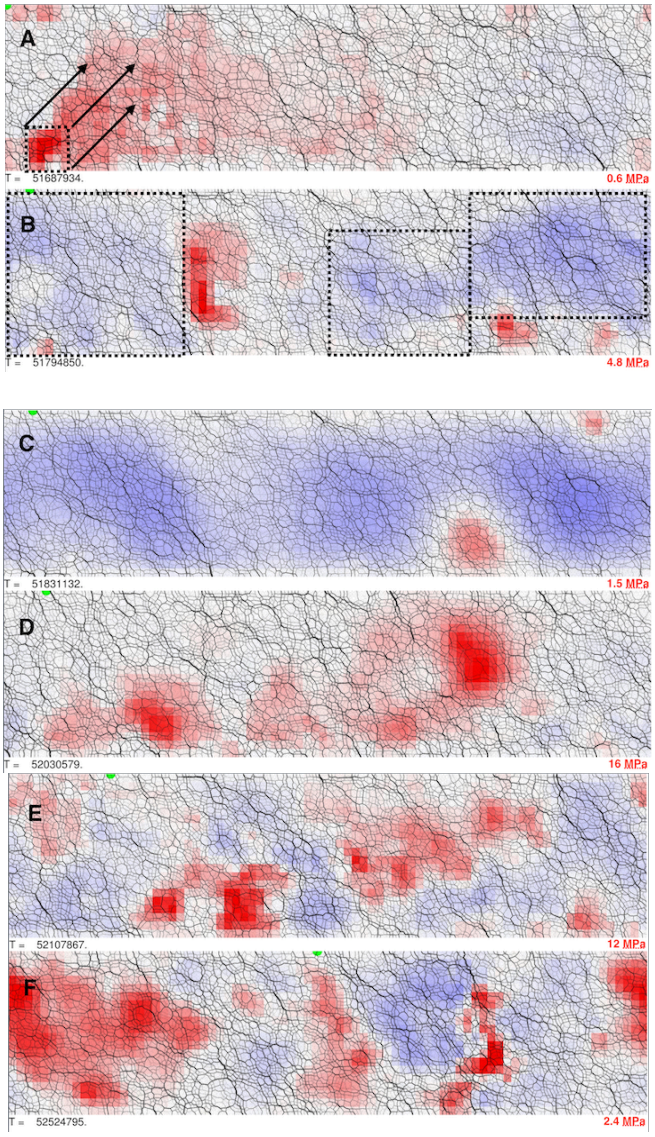

Figure 16. Snapshots of fluid pressure perturbations at the times marked in Figure 15. Pressure color scale varies in each snapshot and is scaled by the pressure shown in the bottom right hand corner. A) The beginning of the slip event is marked by the generation of positive fluid pressures, which quickly span the system. B) The system begins to arrest the slip due to generation of reduced pressures outlines in black rectangles. C) Slip event is completely halted by the generation of negative fluid pressures as indicated by the velocity curve in Figure 15B. D) The negative fluid pressures have mostly diffused by flow. The main slip event is initiated by large positive fluid pressures from collapses in the granular skeleton. Note the lack of negative fluid pressures relative to the positive fluid pressure perturbations. E) Peak velocity of the main slip event. Neighboring areas can experience negative and positive fluid pressures. Fluid flow tries to equilibrate these during the simulated earthquake. F) End of main earthquake. Positive fluid pressures are not organized enough, or not large enough to encourage the slip event to continue.

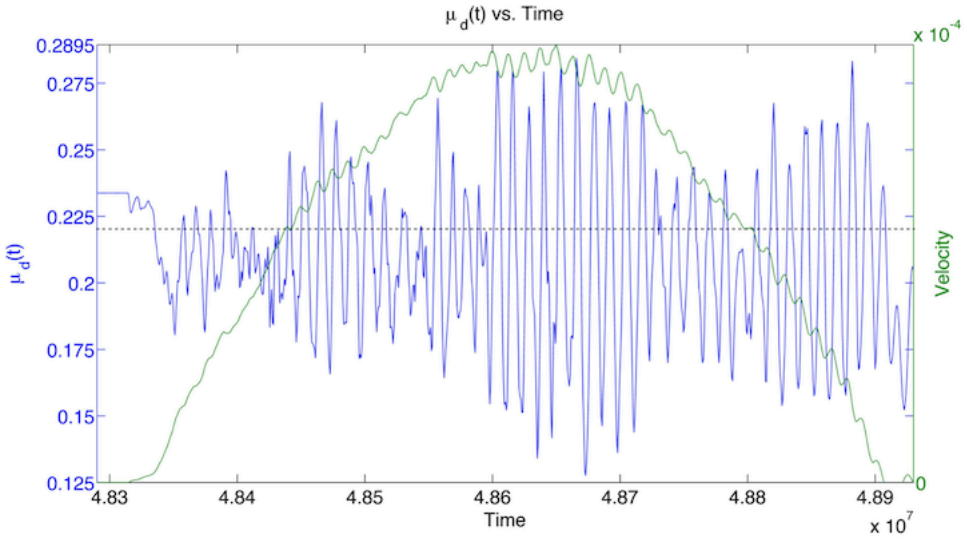

Figure 17. Coefficient of dynamic friction as a function of dimensionless time (left vertical axis) and dimensionless velocity (right axis) for a drained simulation. Note the friction drops from a static value to a dynamic one over a shot time, not instantaneously. The dashed line represents the mean value.

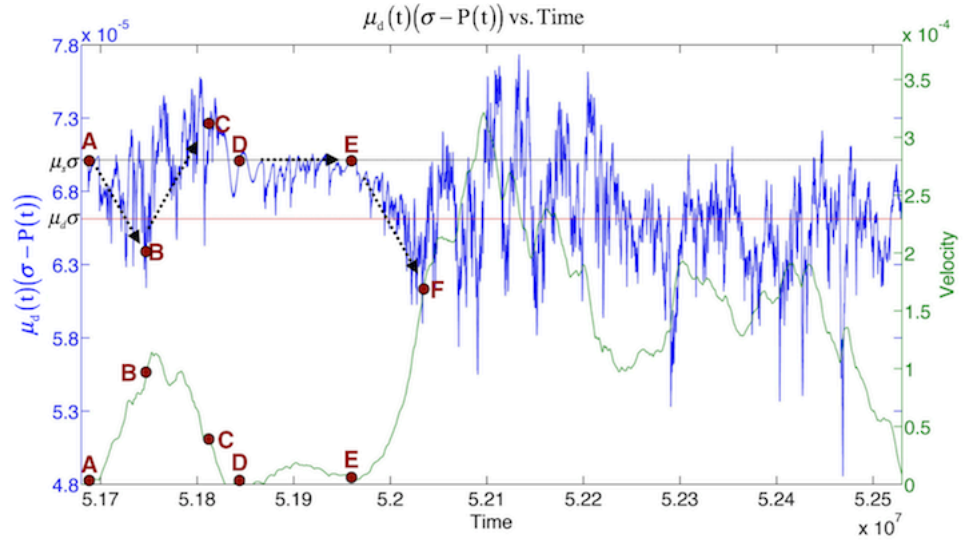

Figure 18. Coefficient of dynamic friction coupled with pressure effects as a function of time (left vertical axis). The right vertical axis shows dimensionless slip velocity for the event presented in Figure 15A-B. Black horizontal line is the static strength of the undrained system while the red horizontal line is the average dynamic coefficient of friction value for the identical fully drained system.

APPENDIX C

The following appendix shows results from full-length simulations consisting of multiple slip events. Each run has four corresponding plots associated with it: applied shear stress normalized by the constant effective confining stress, dimensionless velocity, dimensionless porosity and dimensionless displacement. Some earthquake simulations started with identical granular packings, but different permeabilities. The high – permeability system (drained) is represented by black curves while the low permeability (undrained) is shown by blue curves. Each figure caption contains the elastic parameters used during the simulation.

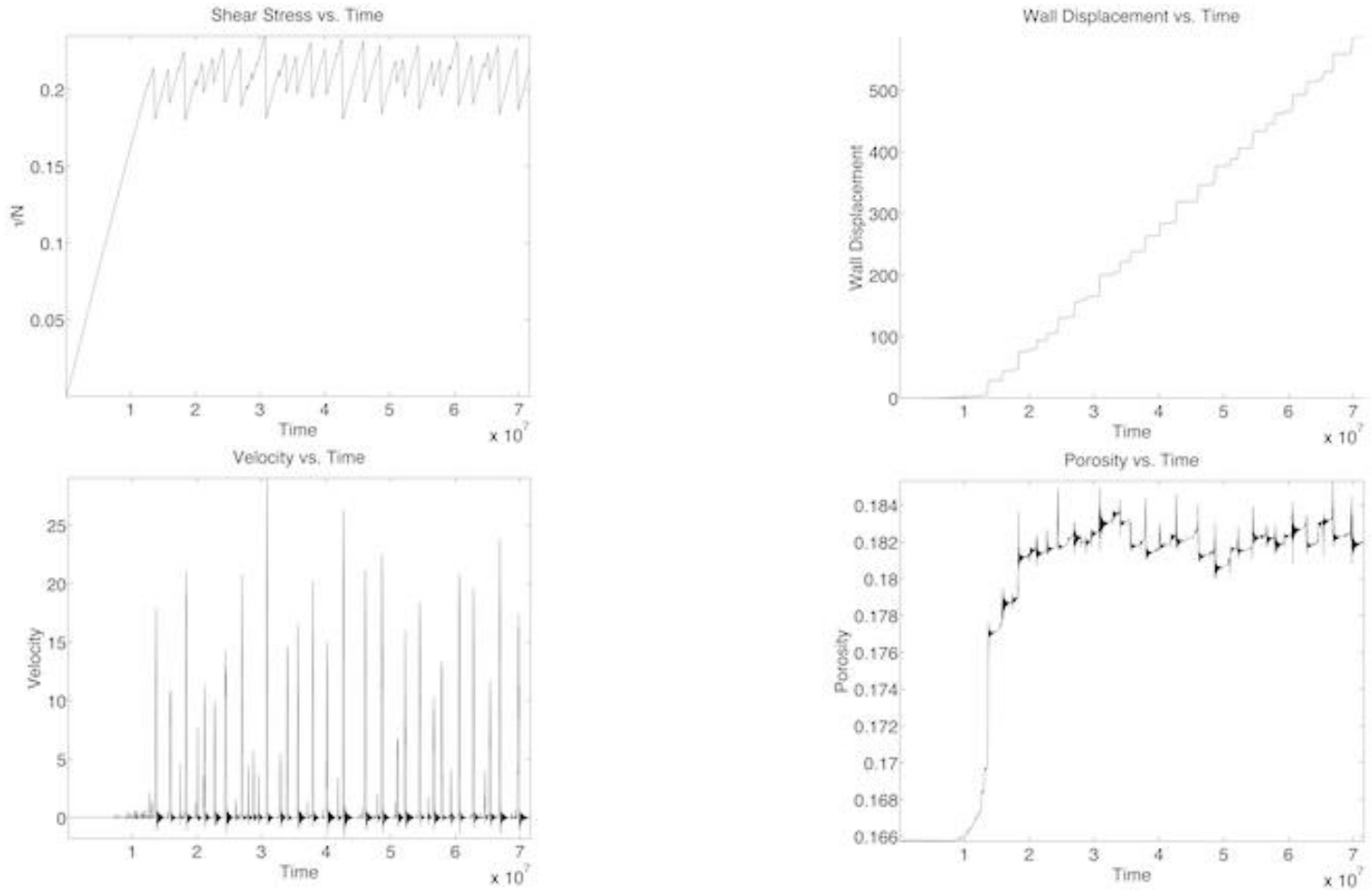

Figure C1. Applied shear stress normalized by the constant effective confining stress, dimensionless velocity, dimensionless displacement, and dimensionless porosity from a simulation. The parameters used in this simulation include: $N=3x10^{-4}$, $V_{sp}=1x10^{-5}$, and $k=5x10^{-7}$ [Table 2, Run 4 Dry].

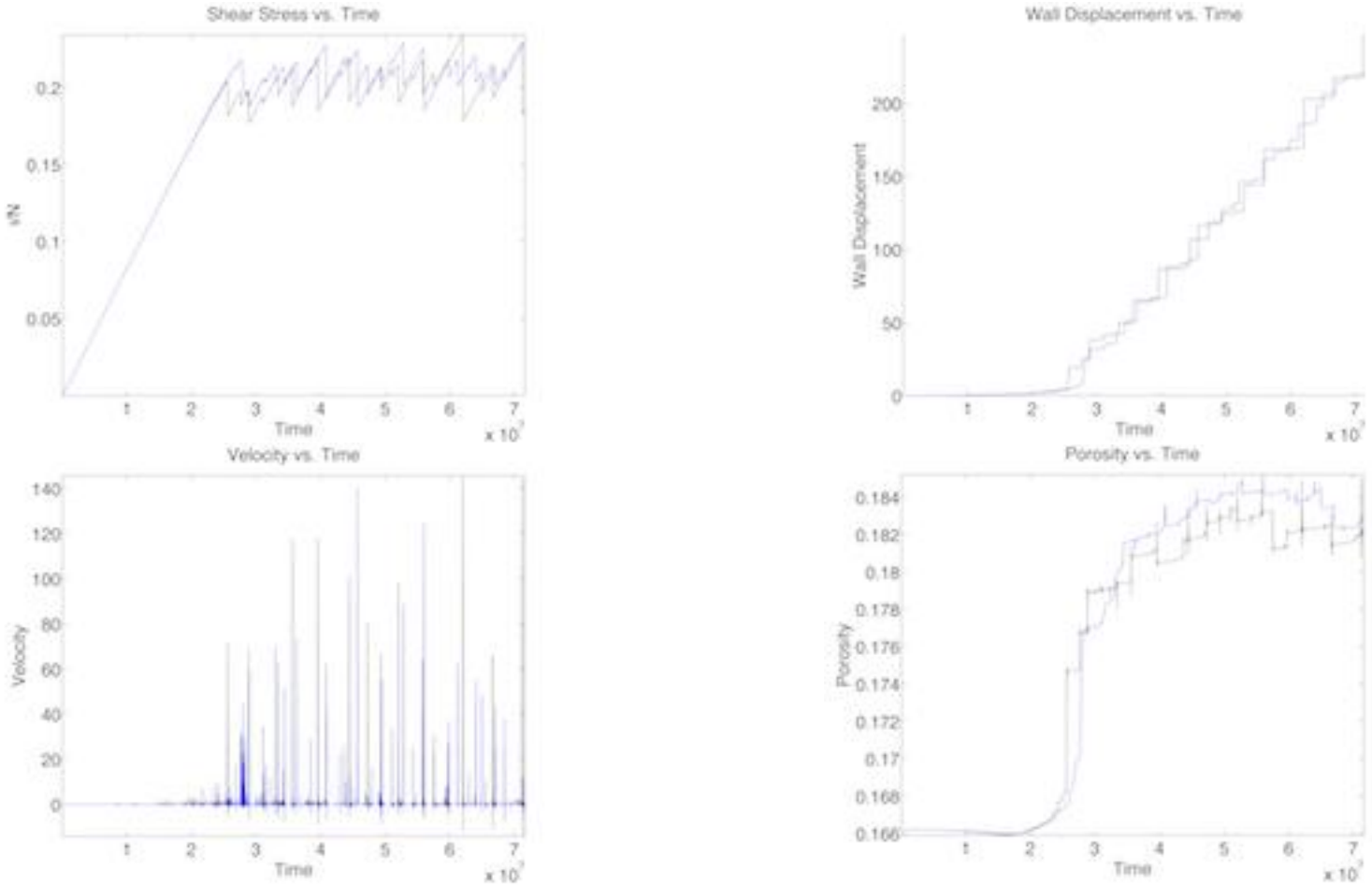

Figure C2. Differences in applied shear stress normalized by the constant effective confining stress, dimensionless velocity, dimensionless displacement, and dimensionless porosity from a drained (black) vs. undrained (blue) simulation. The parameters used in this simulation include: $N=3x10^{-4}$, $V_{sp}=5x10^{-6}$, $k=5x10^{-7}$, and $Perm=1x10^{-5}$ [Table 2, Run 4].

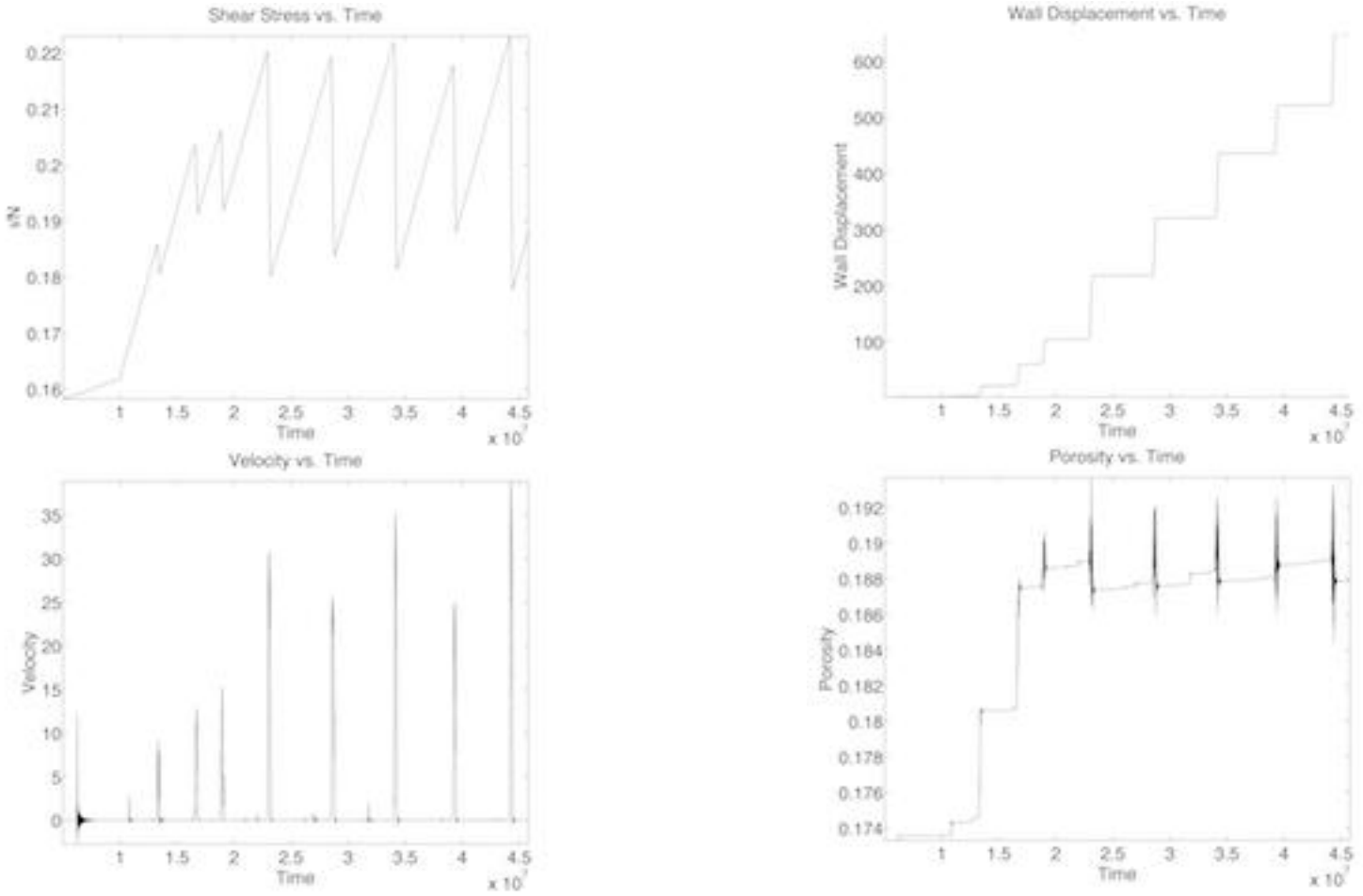

Figure C3. Applied shear stress normalized by the constant effective confining stress, dimensionless velocity, dimensionless displacement, and dimensionless porosity from a simulation. The parameters used in this simulation include: $N=3x10^{-4}$, $V_{sp}=2x10^{-5}$, and $k=3x10^{-8}$ [Table 2, Run 7 Dry].

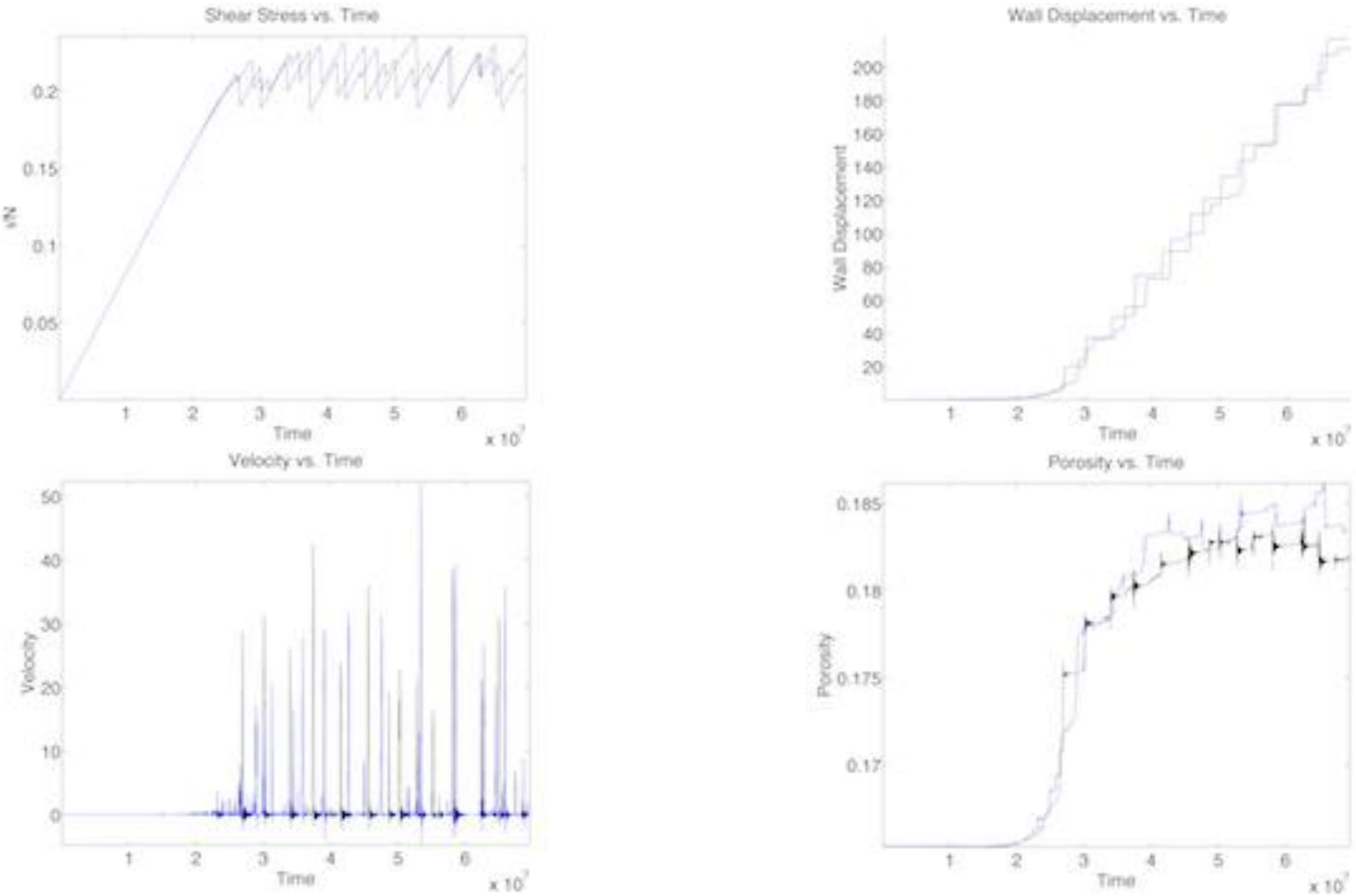

Figure C4. Differences in applied shear stress normalized by the constant effective confining stress, dimensionless velocity, dimensionless displacement, and dimensionless porosity from a drained (black) vs. undrained (blue) simulation. The parameters used in this simulation include: $N=3x10^{-4}$, $V_{sp}=5x10^{-6}$, $k=5x10^{-7}$, and $Perm=1x10^{-5}$ [Table 2, Run 8].

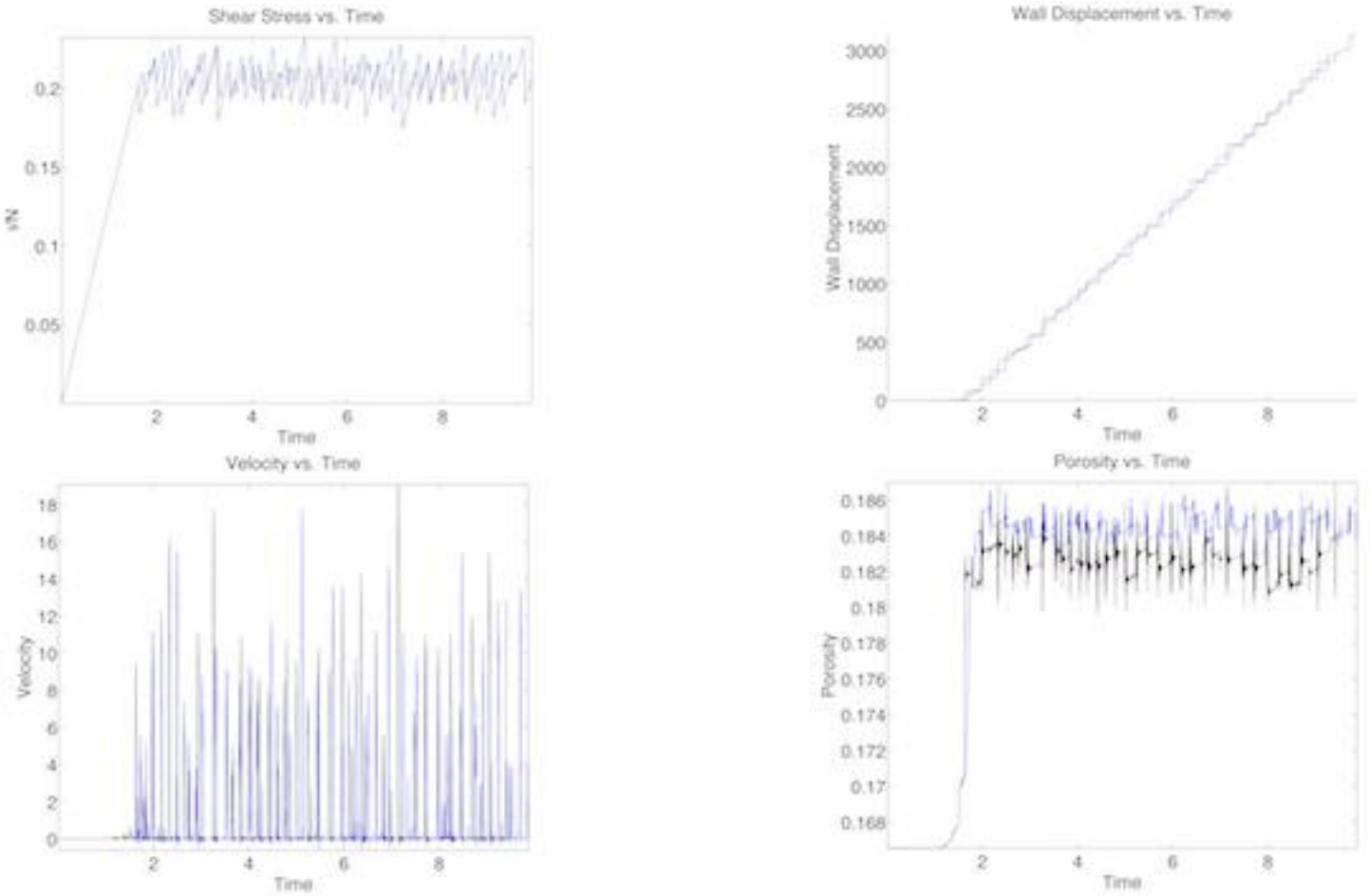

Figure C5. Differences in applied shear stress normalized by the constant effective confining stress, dimensionless velocity, dimensionless displacement, and dimensionless porosity from a drained (black) vs. undrained (blue) simulation. The parameters used in this simulation include: $N=3x10^{-4}$, $V_{sp}=5x10^{-5}$, $k=1x10^{-7}$, and $Perm=1x10^{-5}$ [Table 2, Run14].

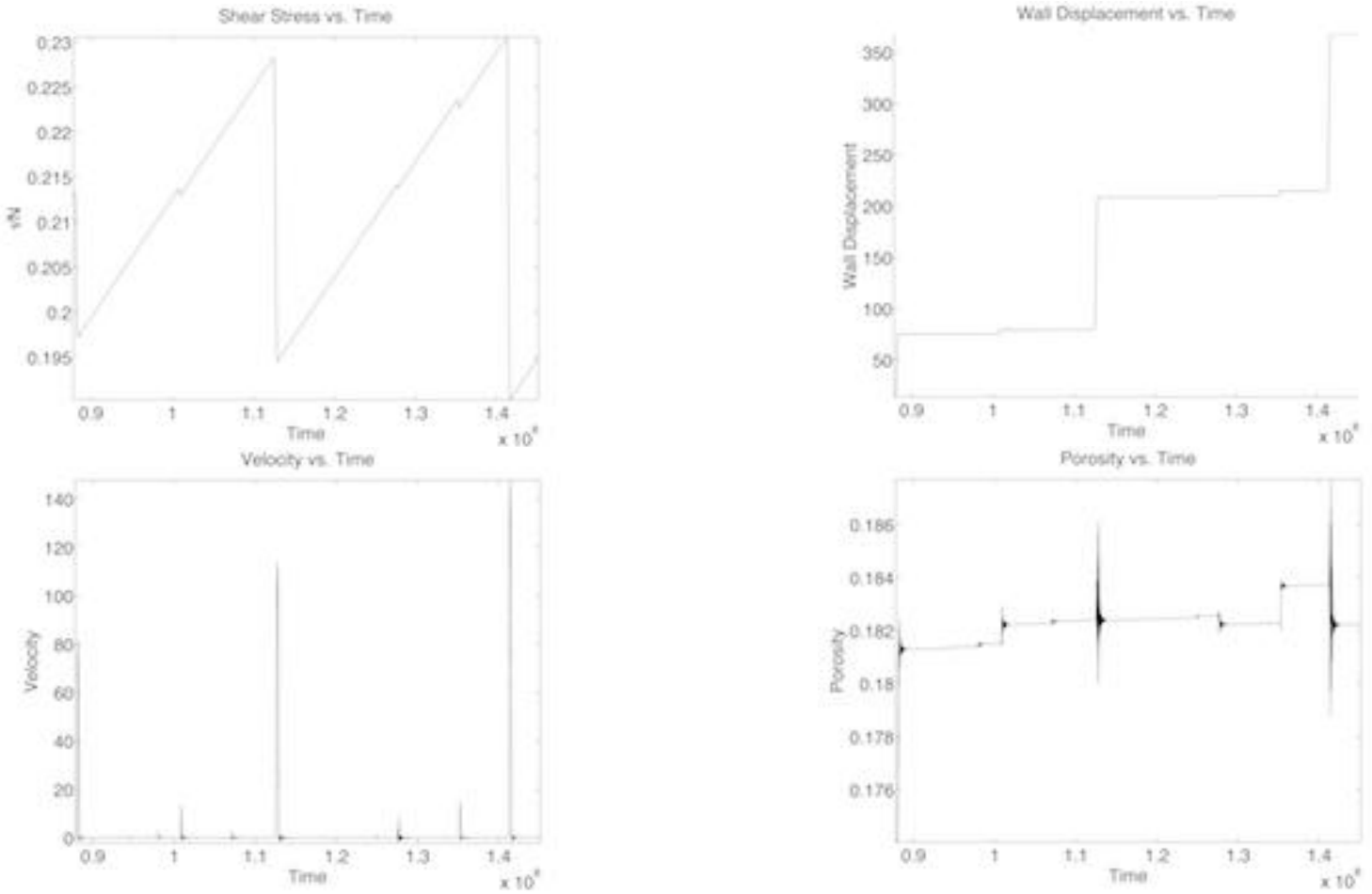

Figure C6. Applied shear stress normalized by the constant effective confining stress, dimensionless velocity, dimensionless displacement, and dimensionless porosity from a simulation. The parameters used in this simulation include: $N=3x10^{-4}$, $V_{sp}=5x10^{-6}$, and $k=8x10^{-8}$ [Table 2, Run 15 Dry].

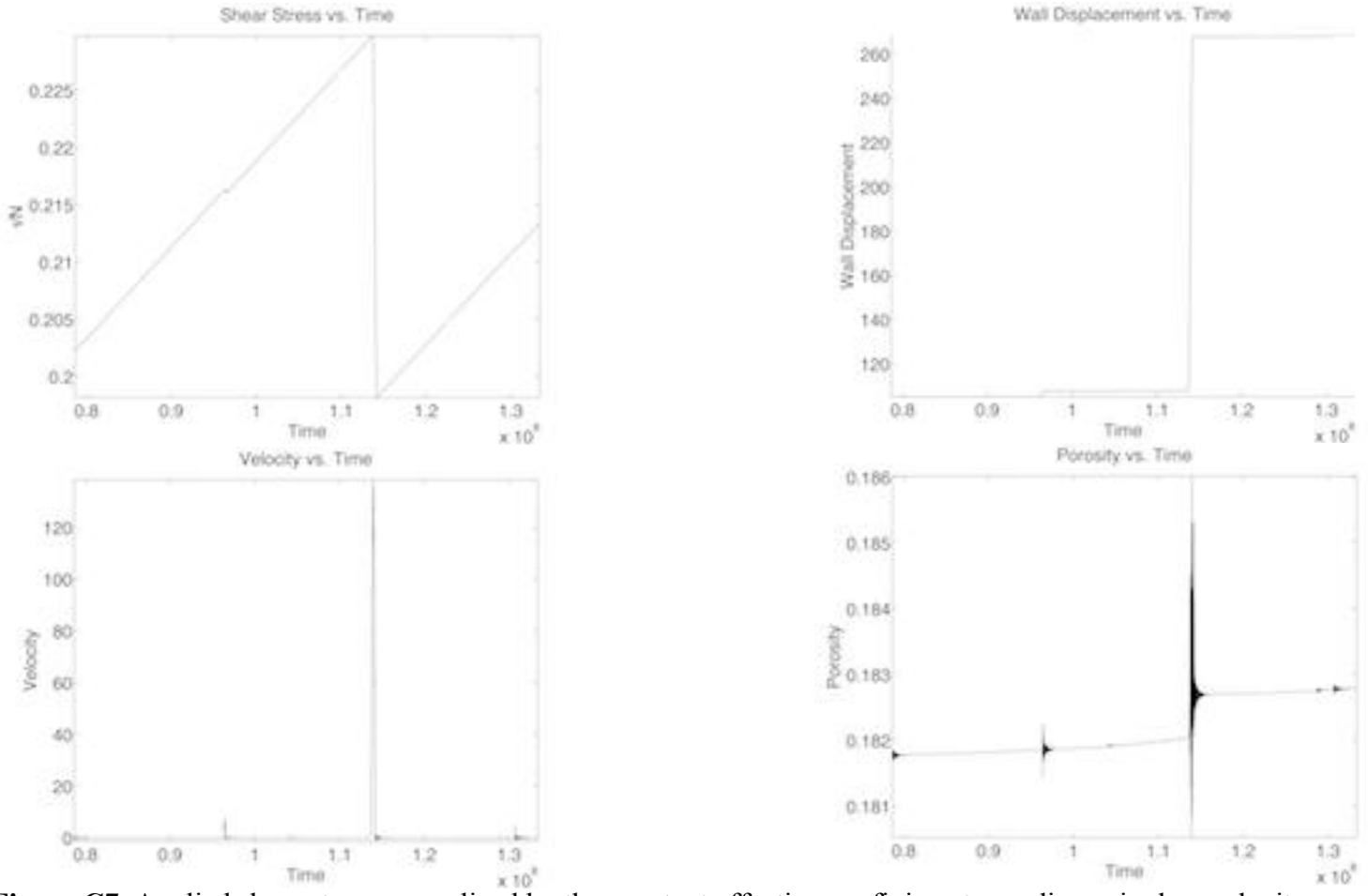

Figure C7. Applied shear stress normalized by the constant effective confining stress, dimensionless velocity, dimensionless displacement, and dimensionless porosity from a simulation. The parameters used in this simulation include: $N=3x10^{-4}$, $V_{sp}=2x10^{-6}$, and $k=3x10^{-8}$ [Table 2, Run 16 Dry].

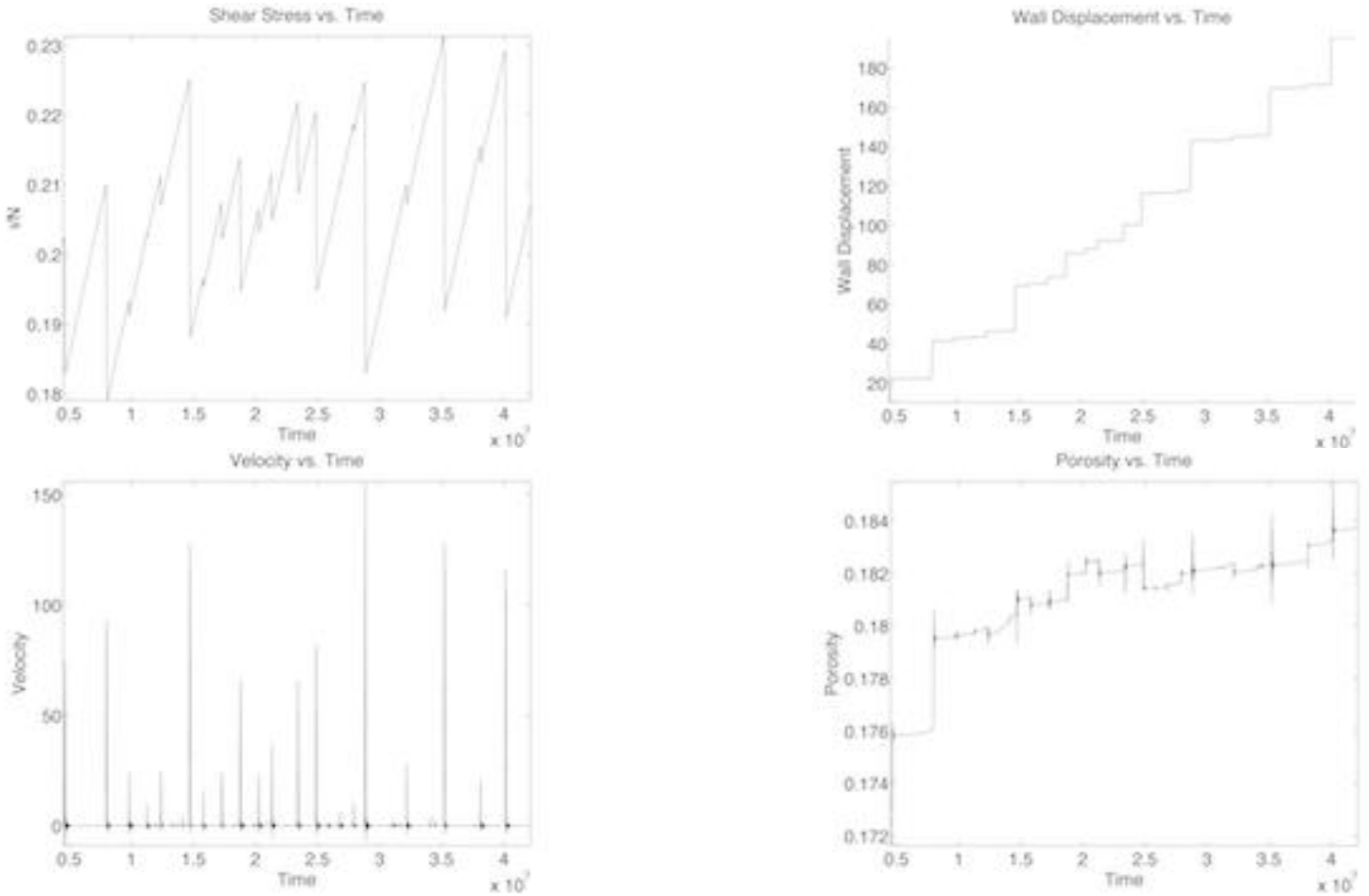

Figure C8. Applied shear stress normalized by the constant effective confining stress, dimensionless velocity, dimensionless displacement, and dimensionless porosity from a simulation. The parameters used in this simulation include: $N=3x10^{-4}$, $V_{sp}=5x10^{-6}$, and $k=5x10^{-7}$ [Table 2, Run 17 Dry].

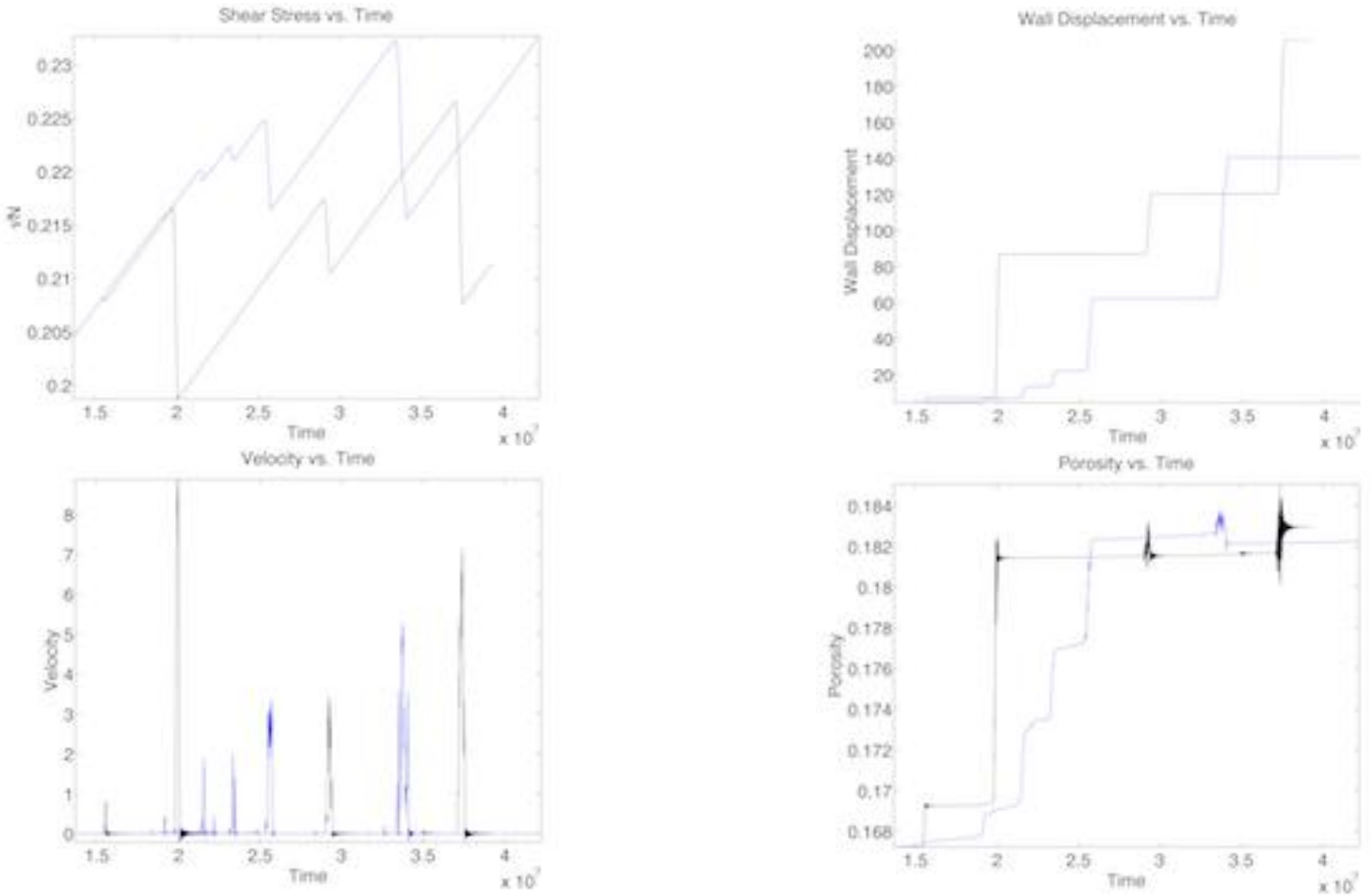

Figure C9. Differences in applied shear stress normalized by the constant effective confining stress, dimensionless velocity, dimensionless displacement, and dimensionless porosity from a drained (black) vs. undrained (blue) simulation. The parameters used in this simulation include: $N=3x10^{-4}$, $V_{sp}=9x10^{-6}$, $k=7x10^{-8}$, and $Perm=1x10^{-5}$ [Table 2, Run18].

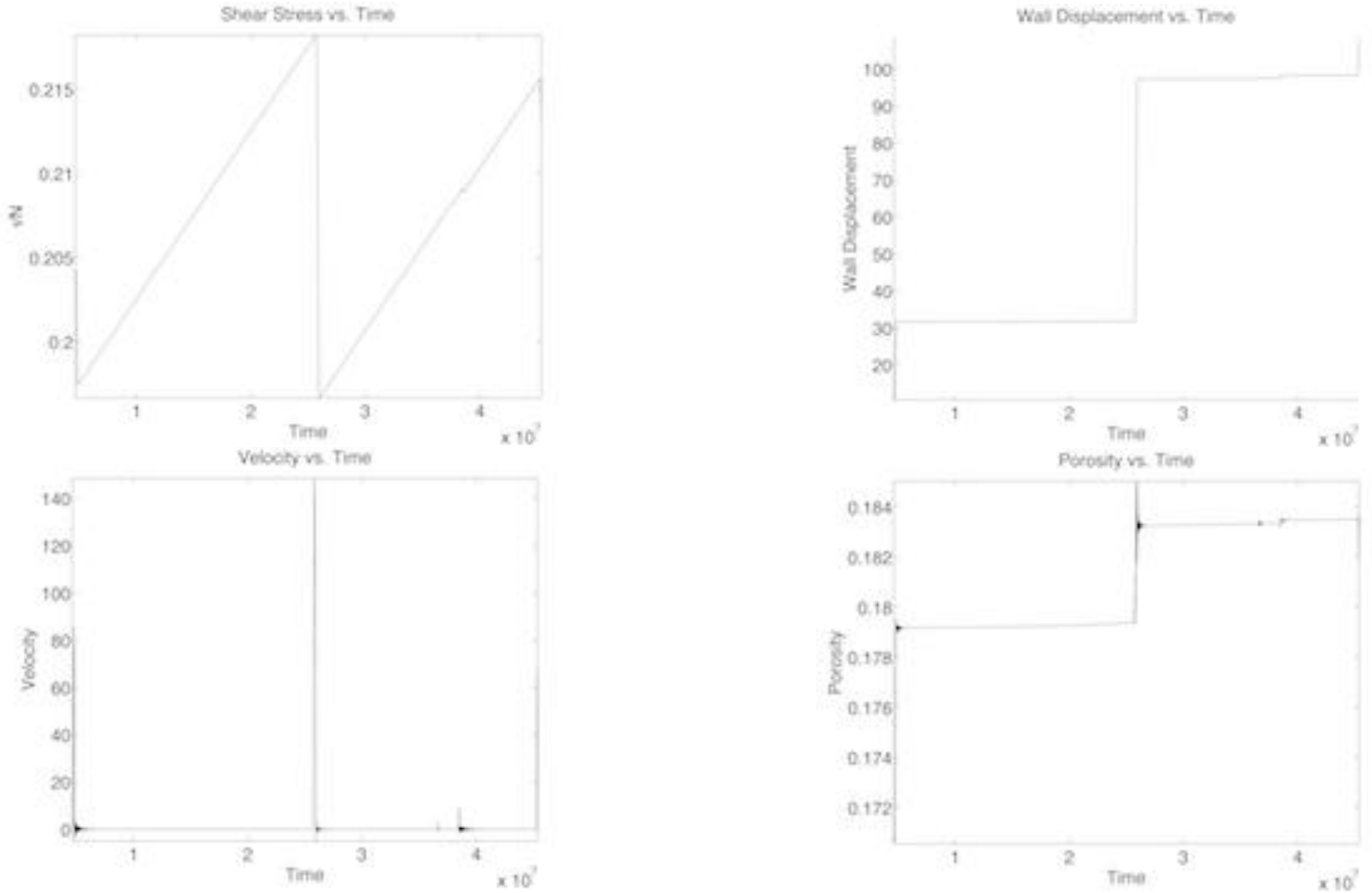

Figure C10. Applied shear stress normalized by the constant effective confining stress, dimensionless velocity, dimensionless displacement, and dimensionless porosity from a simulation. The parameters used in this simulation include: $N=3x10^{-4}$, $V_{sp}=3x10^{-6}$, and $k=1x10^{-7}$ [Table 2, Run 19 Dry].

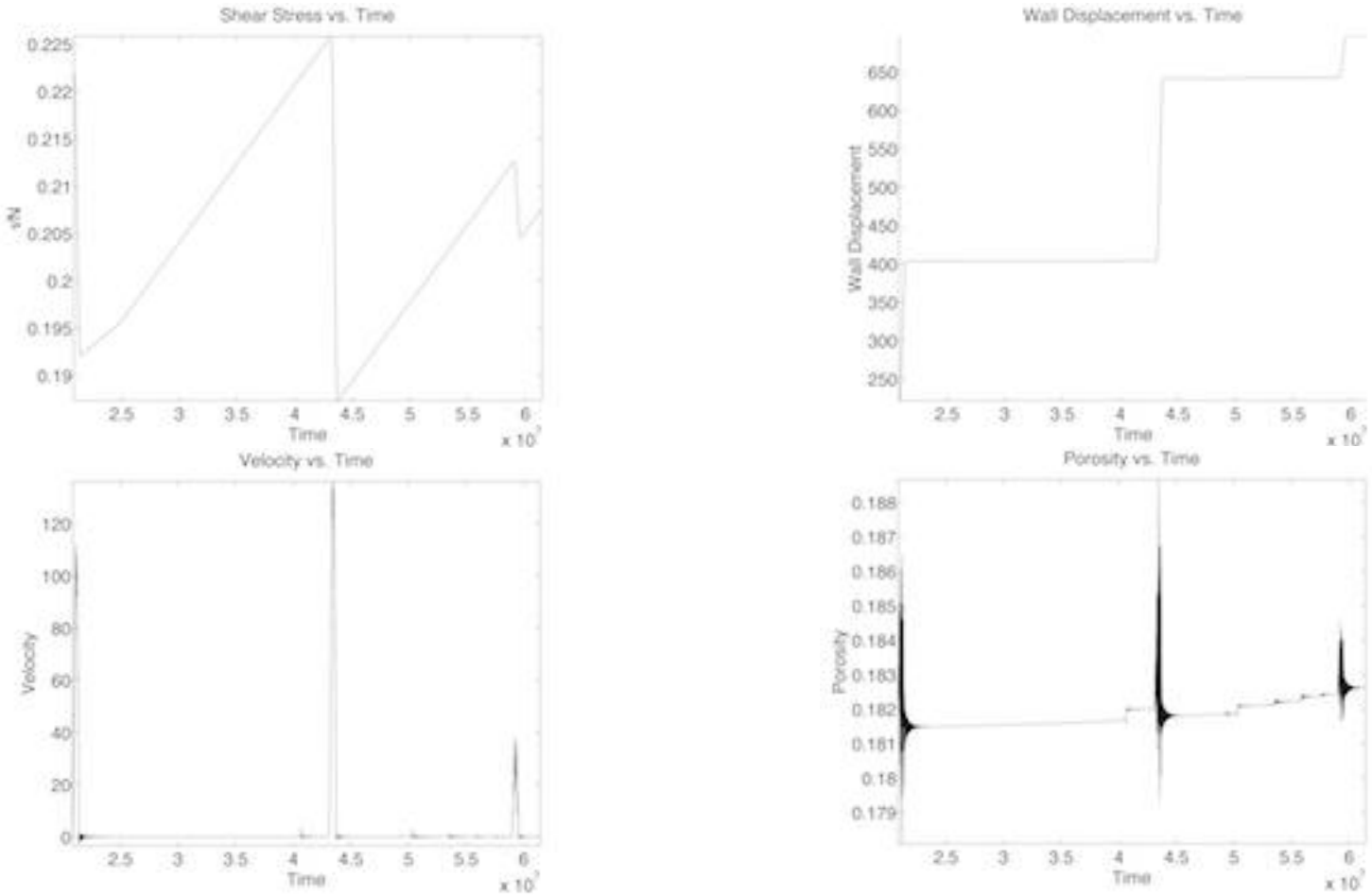

Figure C11. Applied shear stress normalized by the constant effective confining stress, dimensionless velocity, dimensionless displacement, and dimensionless porosity from a simulation. The parameters used in this simulation include: $N=3x10^{-4}$, $V_{sp}=1x10^{-5}$, and $k=5x10^{-8}$ [Table 2, Run 20 Dry].

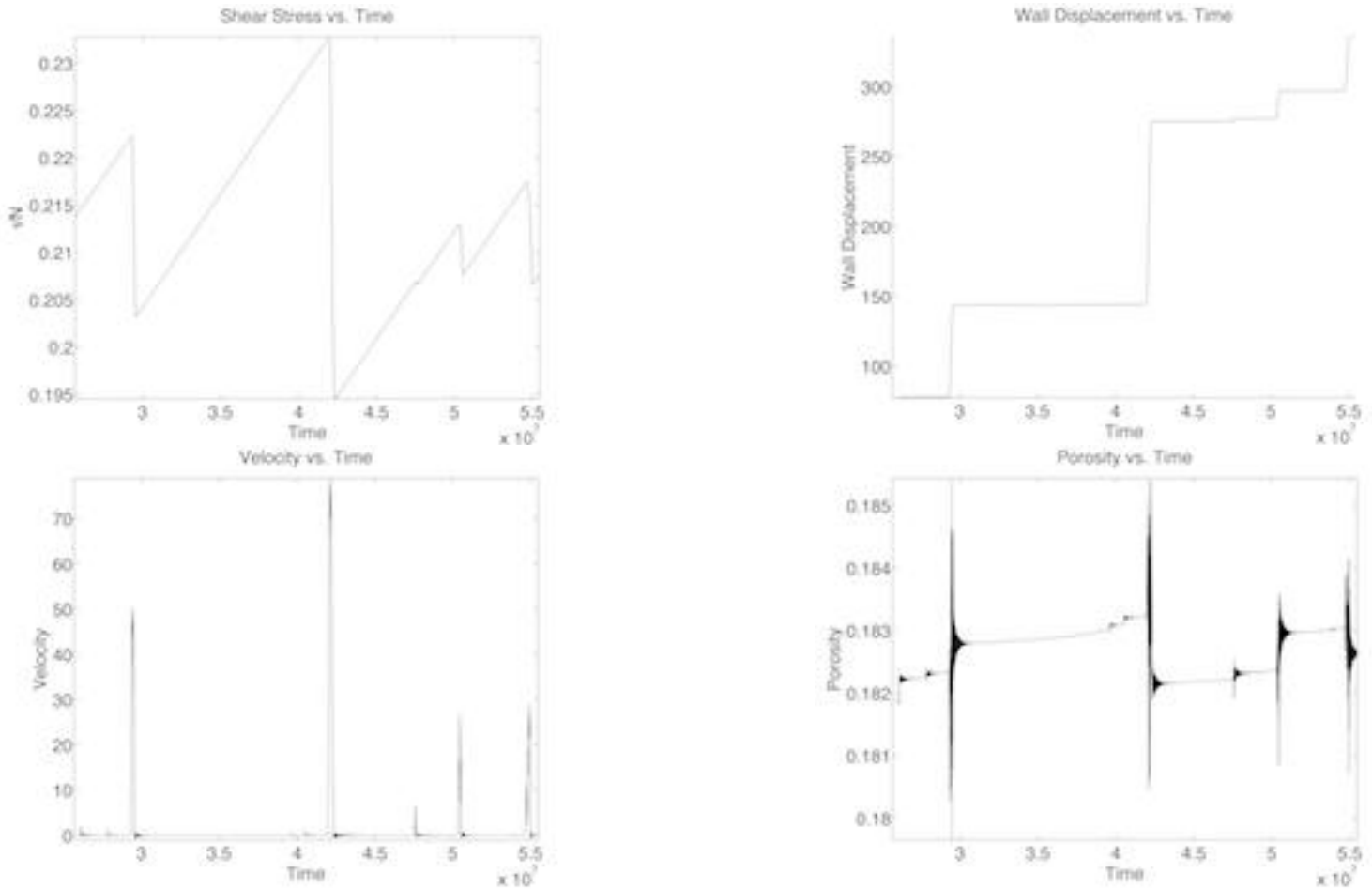

Figure C12. Applied shear stress normalized by the constant effective confining stress, dimensionless velocity, dimensionless displacement, and dimensionless porosity from a simulation. The parameters used in this simulation include: $N=3x10^{-4}$, $V_{sp}=3x10^{-6}$, and $k=9x10^{-8}$ [Table 2, Run 21 Dry].

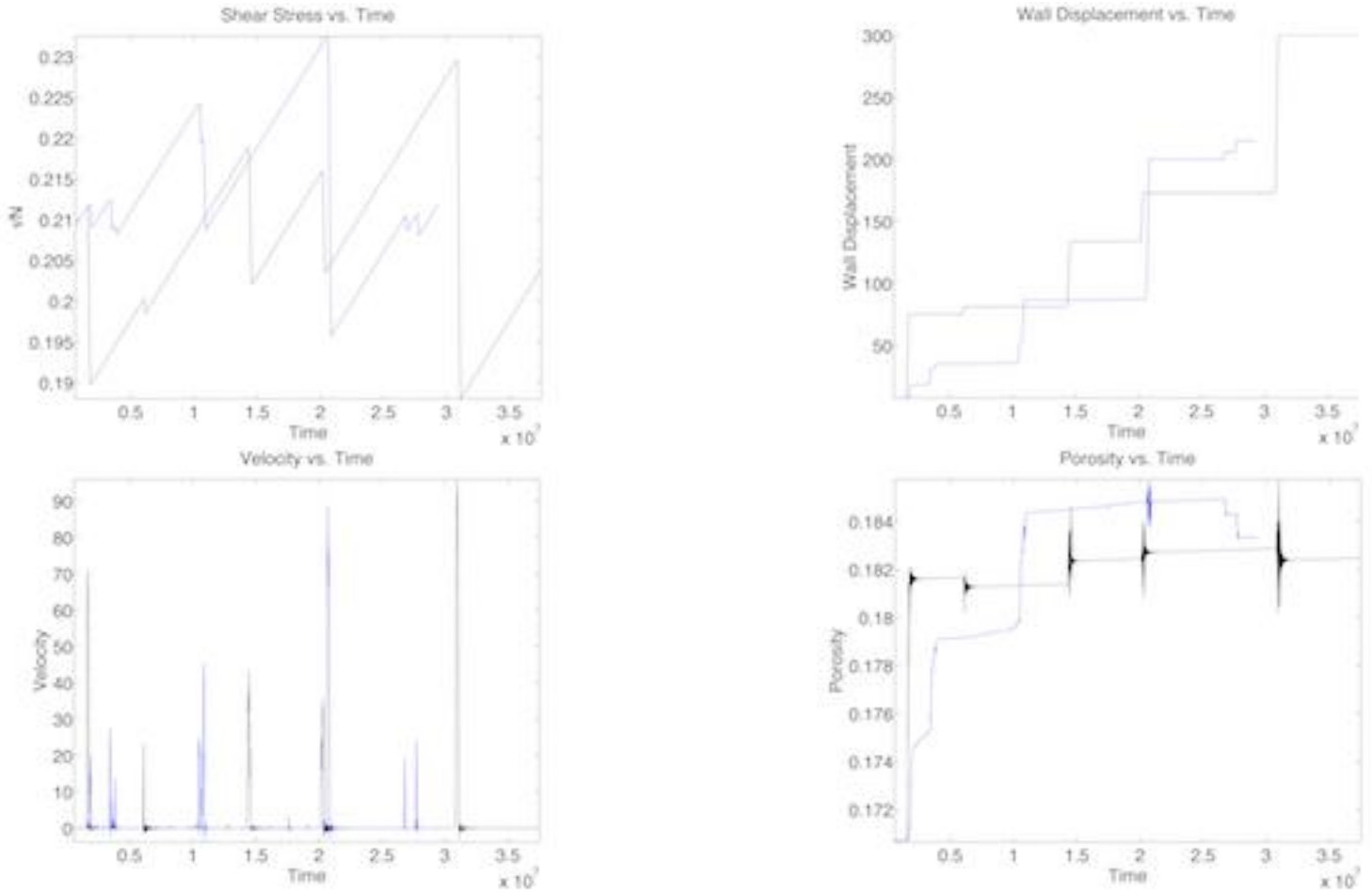

Figure C13. Differences in applied shear stress normalized by the constant effective confining stress, dimensionless velocity, dimensionless displacement, and dimensionless porosity from a drained (black) vs. undrained (blue) simulation. The parameters used in this simulation include: $N=3x10^{-4}$, $V_{sp}=7.5x10^{-6}$, $k=1x10^{-7}$, and $Perm=1x10^{-5}$ [Table 2, Run22].

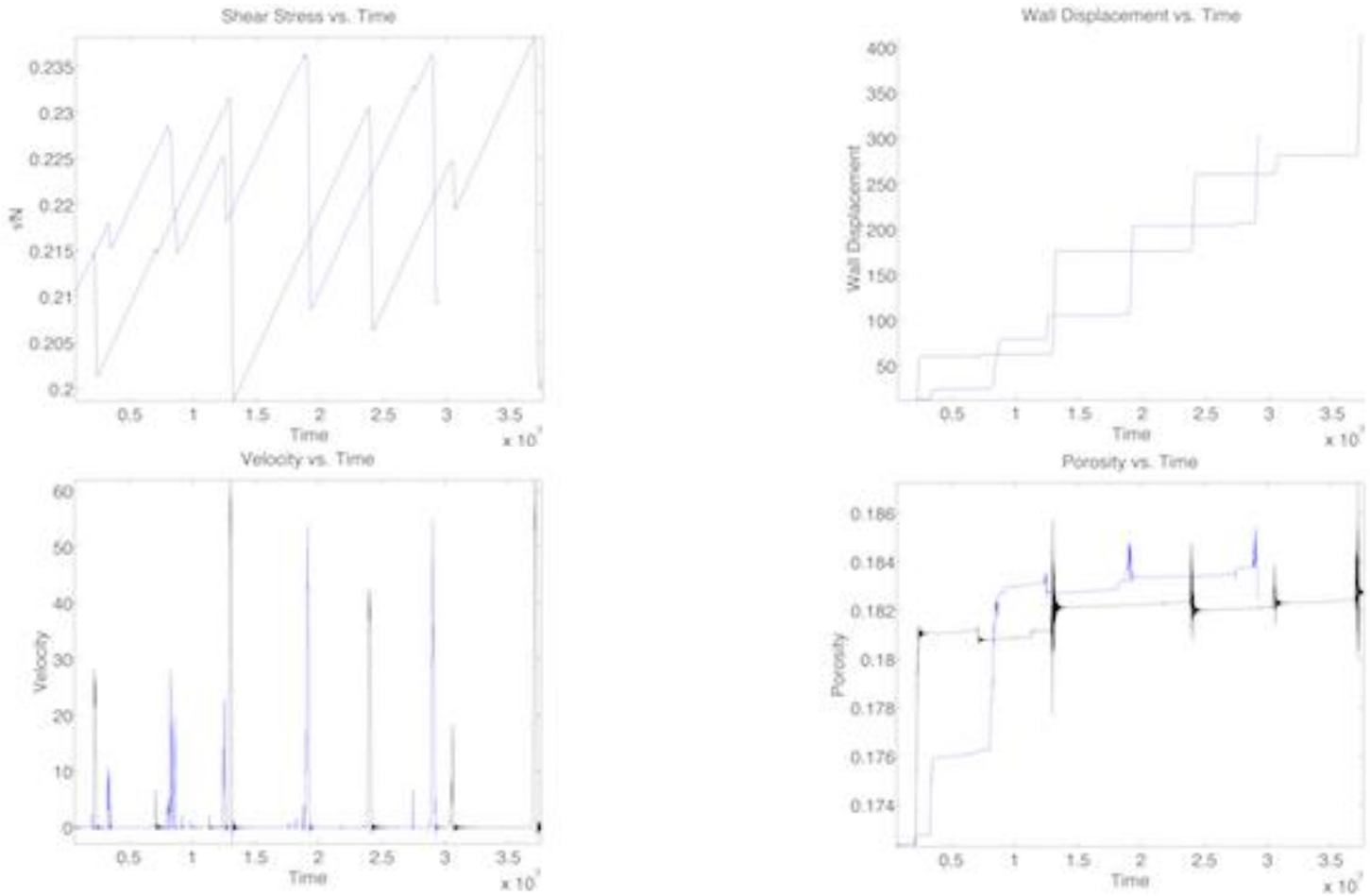

Figure C14. Differences in applied shear stress normalized by the constant effective confining stress, dimensionless velocity, dimensionless displacement, and dimensionless porosity from a drained (black) vs. undrained (blue) simulation. The parameters used in this simulation include: $N=3x10^{-4}$, $V_{sp}=1x10^{-5}$, $k=9x10^{-8}$, and $Perm=1x10^{-5}$ [Table 2, Run23].

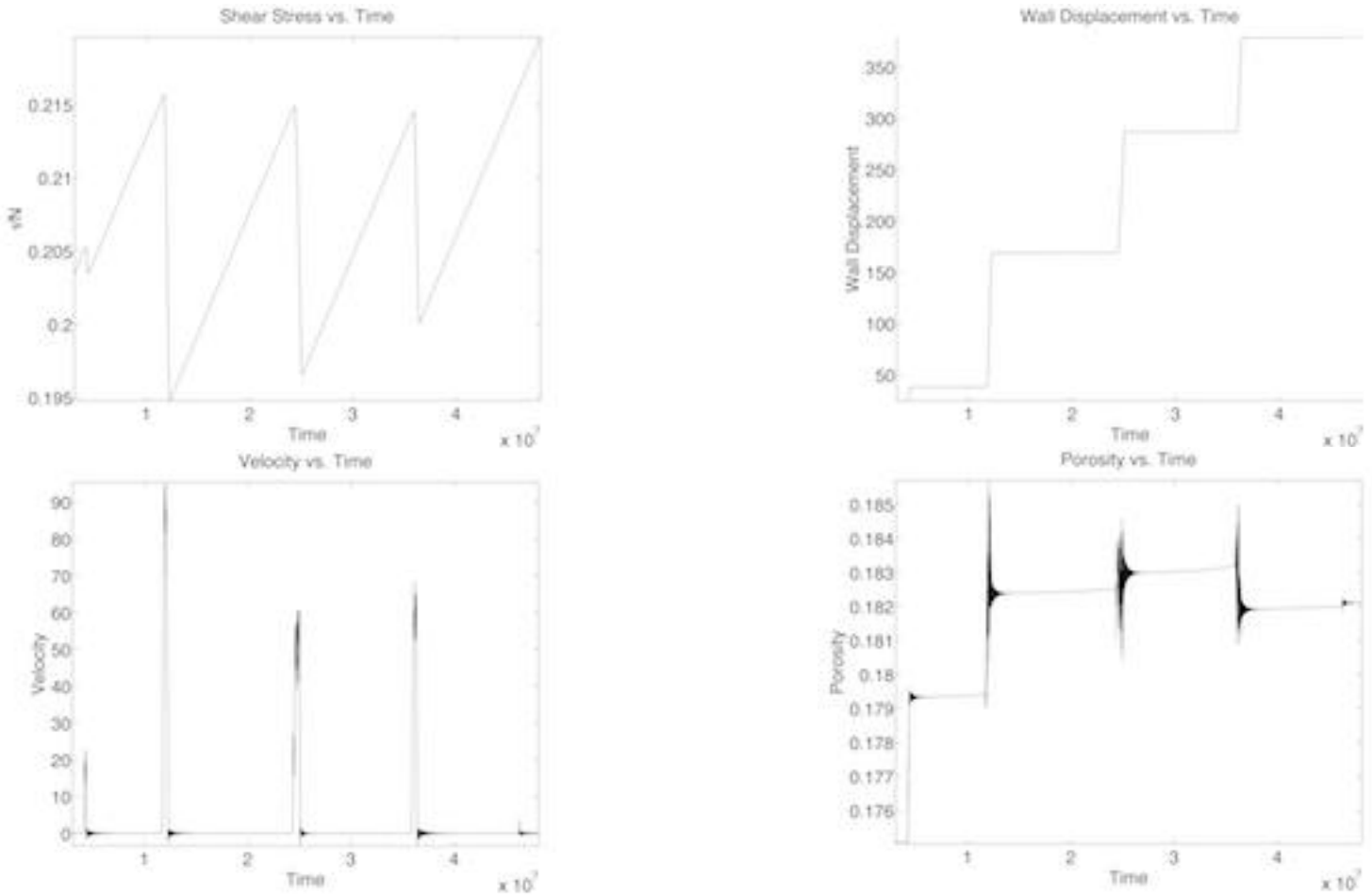

Figure C15. Applied shear stress normalized by the constant effective confining stress, dimensionless velocity, dimensionless displacement, and dimensionless porosity from a simulation. The parameters used in this simulation include: $N=3x10^{-4}$, $V_{sp}=3x10^{-5}$, and $k=7x10^{-8}$ [Table 2, Run 24 Dry].

APPENDIX D

The following appendix shows results from individual simulations which began with the identical granular arrangements. Each run has four corresponding plots associated with it: applied shear stress normalized by the constant effective confining stress, dimensionless velocity, dimensionless porosity and dimensionless displacement. These earthquake simulations started with identical granular packings, but different permeabilities. The high –permeability system (drained) is represented by black curves while the low permeability (undrained) is shown by blue curves. Each figure caption contains the elastic parameters used during the simulation.

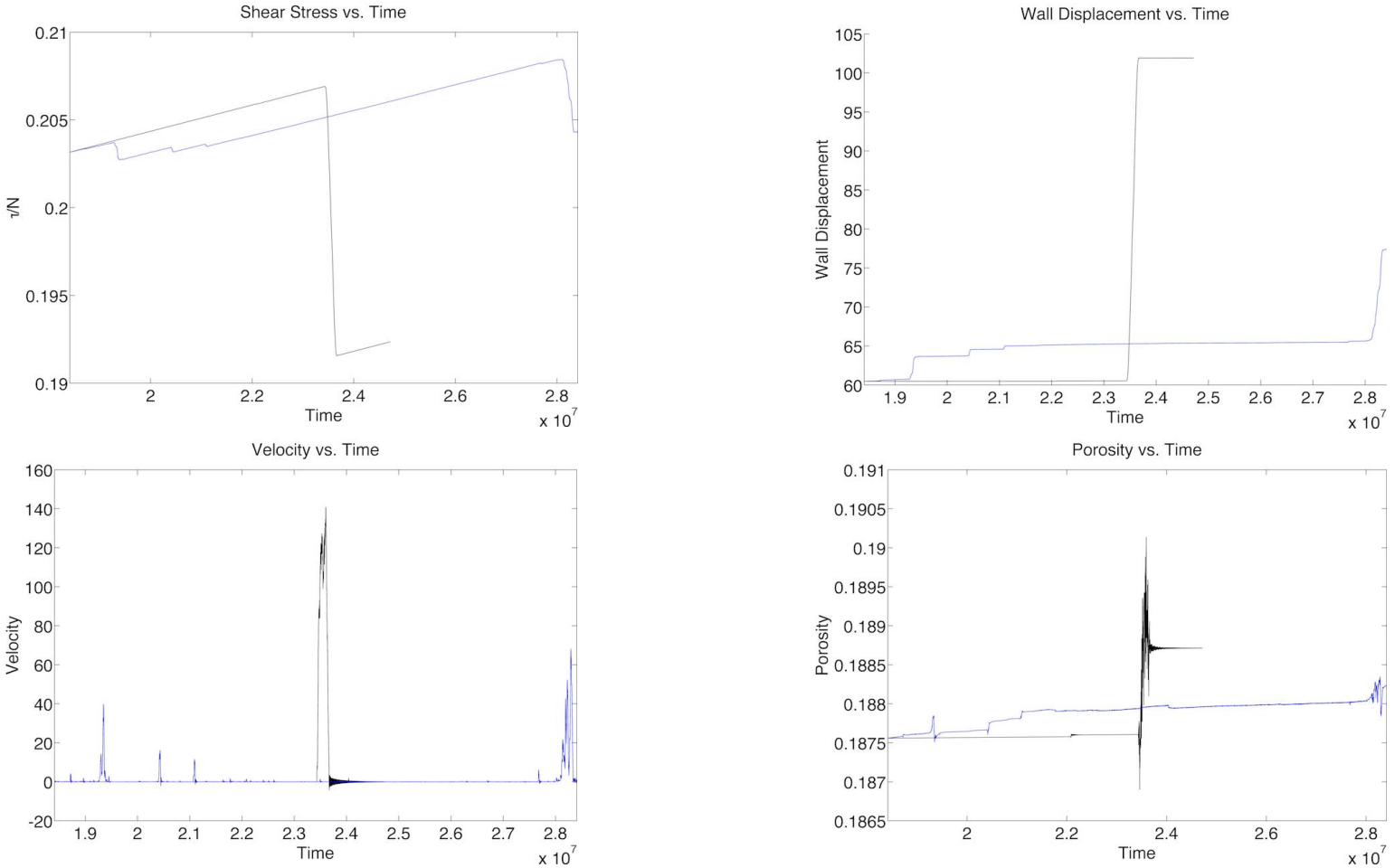

Figure D1. Differences in applied shear stress normalized by the constant effective confining stress, dimensionless velocity, dimensionless displacement, and dimensionless porosity from a drained (black) vs. undrained (blue) simulation. The parameters used in this simulation include: $N=3x10^{-4}$, $V_{sp}=2x10^{-6}$, $k=3x10^{-8}$, and $Perm=1x10^{-5}$. The undrained simulation was classified as a Type II-C earthquake [Table 3, Run 7 Dry Restart Slip 3 II-C].

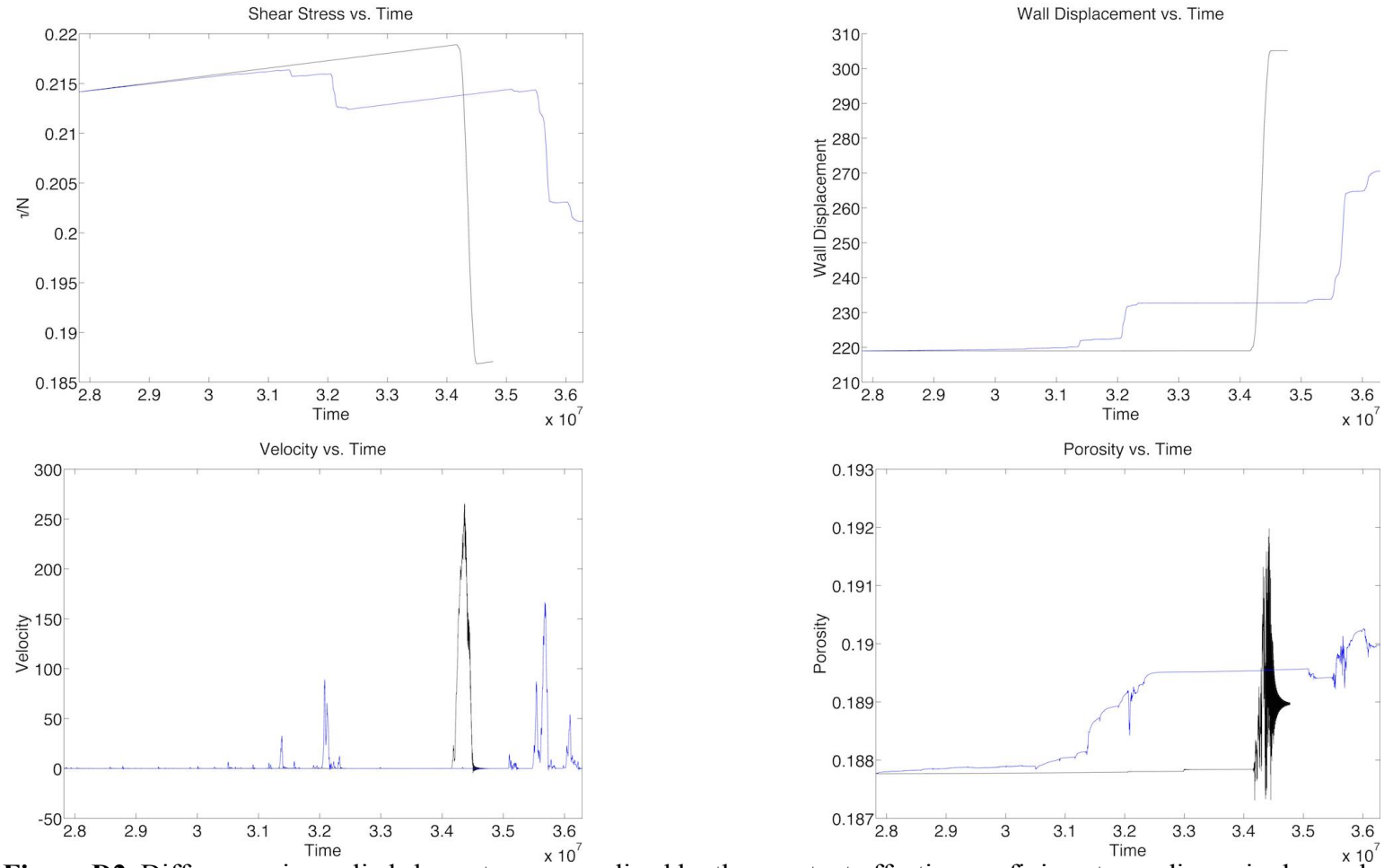

Figure D2. Differences in applied shear stress normalized by the constant effective confining stress, dimensionless velocity, dimensionless displacement, and dimensionless porosity from a drained (black) vs. undrained (blue) simulation. The parameters used in this simulation include: $N=3x10^{-4}$, $V_{sp}=2x10^{-6}$, $k=3x10^{-8}$, and $Perm=1x10^{-5}$. The undrained simulation was classified as a Type I-C earthquake [Table 3, Run 7 Dry Restart Slip 5 I-C].

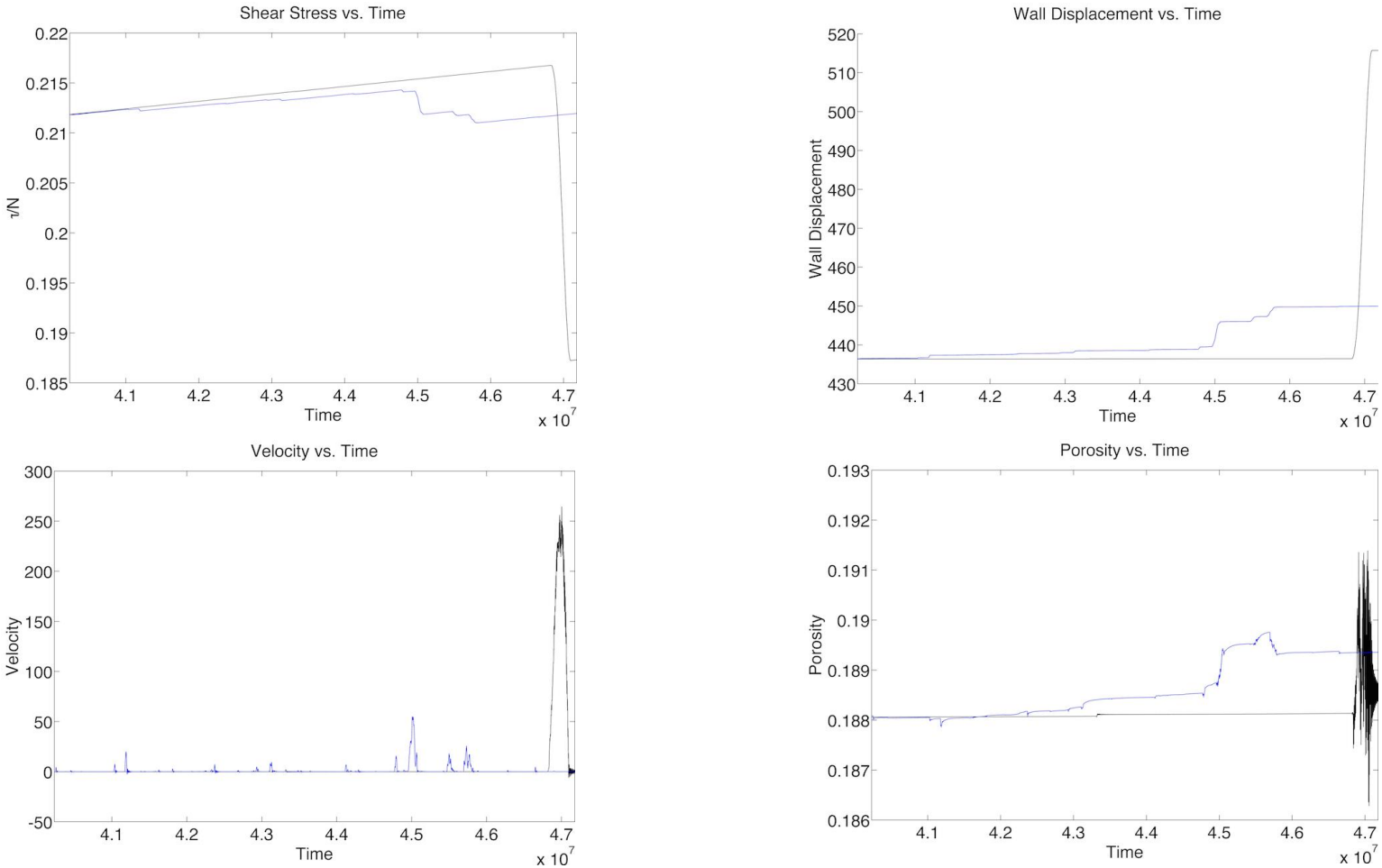

Figure D3. Differences in applied shear stress normalized by the constant effective confining stress, dimensionless velocity, dimensionless displacement, and dimensionless porosity from a drained (black) vs. undrained (blue) simulation. The parameters used in this simulation include: $N=3x10^{-4}$, $V_{sp}=2x10^{-6}$, $k=3x10^{-8}$, and $Perm=1x10^{-5}$. The undrained simulation was classified as a Type I-C earthquake [Table 3, Run 7 Dry Restart Slip 7 I-C].

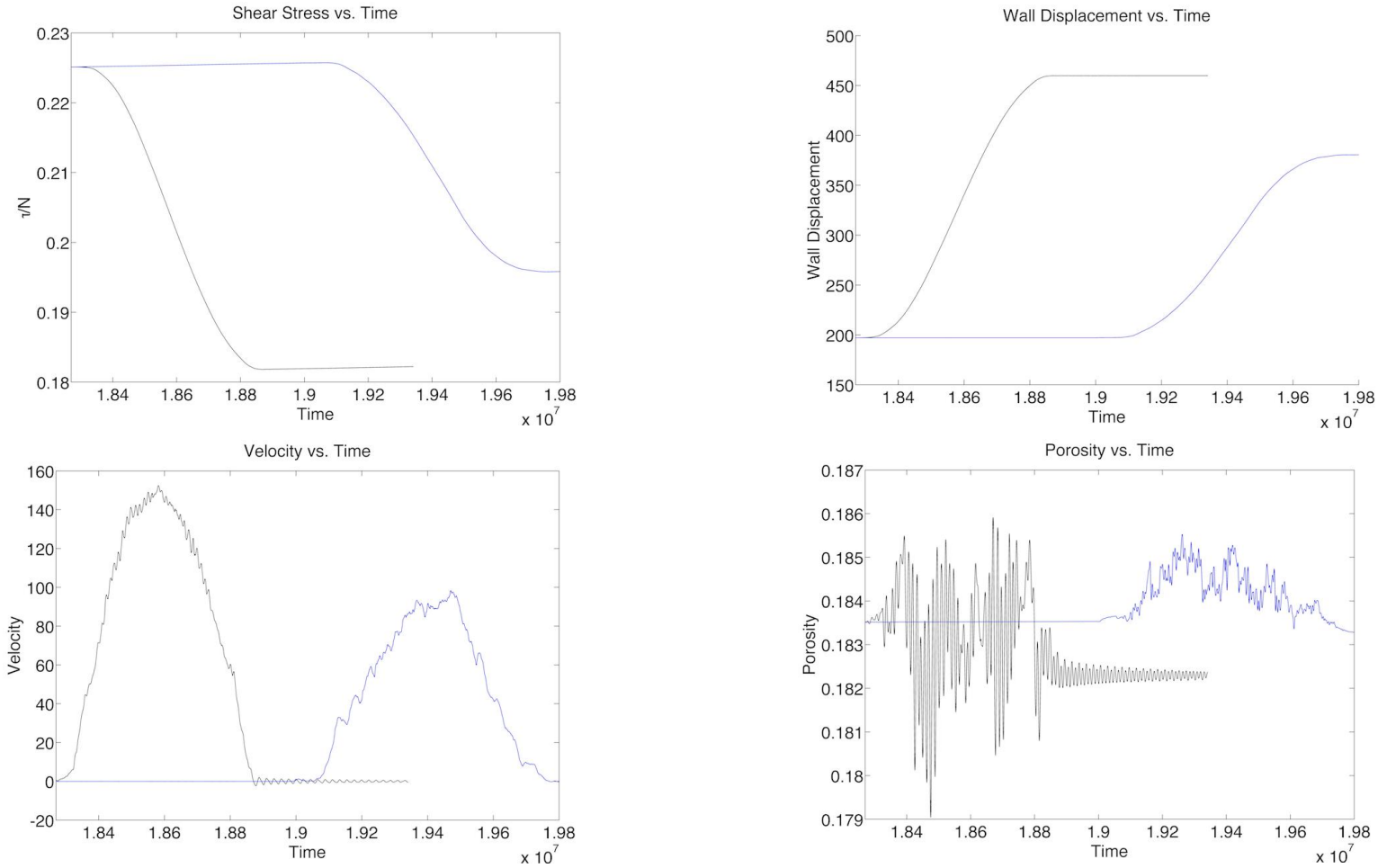

Figure D4. Differences in applied shear stress normalized by the constant effective confining stress, dimensionless velocity, dimensionless displacement, and dimensionless porosity from a drained (black) vs. undrained (blue) simulation. The parameters used in this simulation include: $N=3x10^{-4}$, $V_{sp}=5x10^{-6}$, $k=5x10^{-8}$, and $Perm=1x10^{-5}$. The undrained simulation was classified as a Type II earthquake [Table 3, Run 14 Dry Restart Slip 2 II].

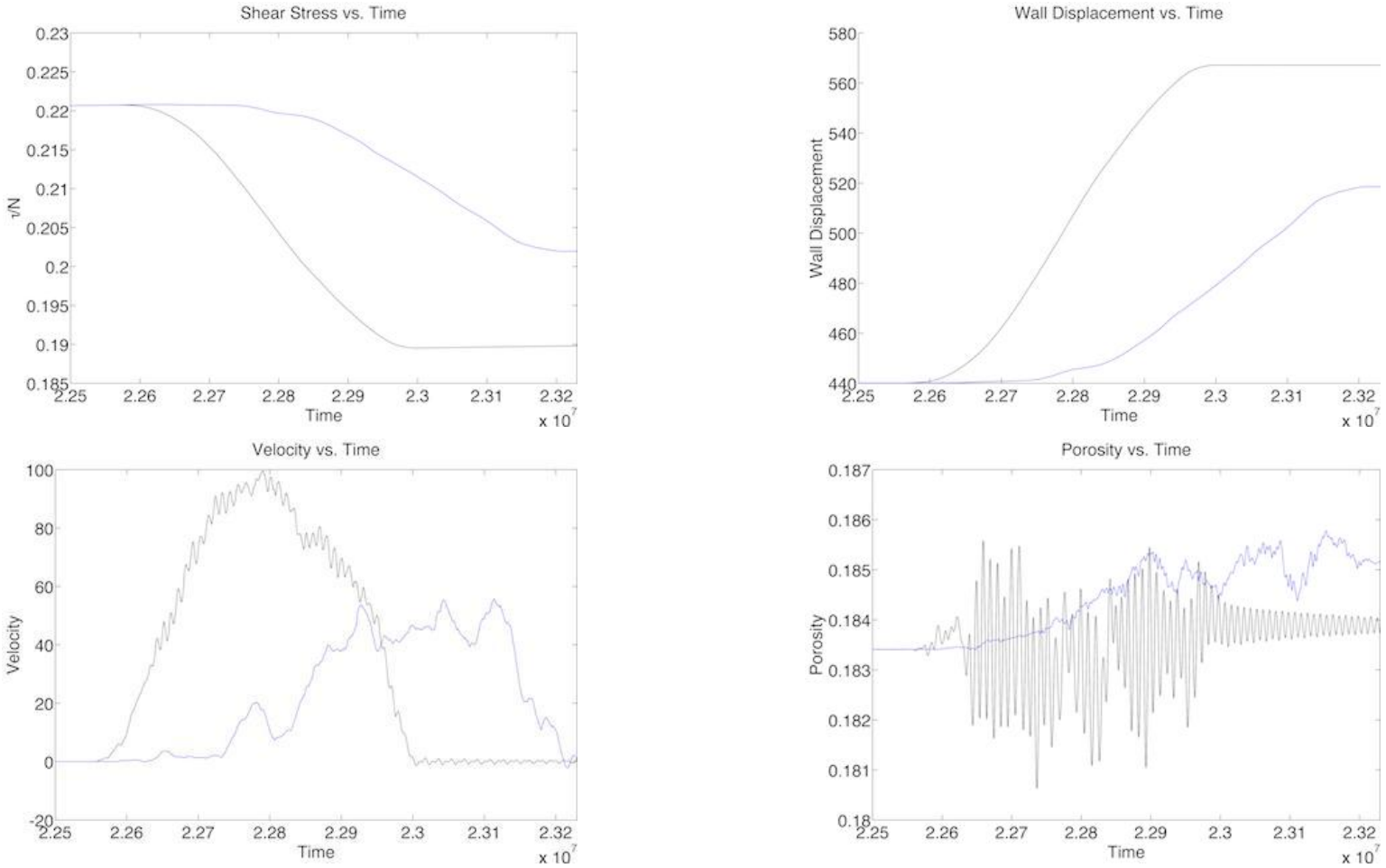

Figure D5. Differences in applied shear stress normalized by the constant effective confining stress, dimensionless velocity, dimensionless displacement, and dimensionless porosity from a drained (black) vs. undrained (blue) simulation. The parameters used in this simulation include: $N=3x10^{-4}$, $V_{sp}=5x10^{-6}$, $k=7.5x10^{-8}$, and $Perm=1x10^{-5}$. The undrained simulation was classified as a Type II-C earthquake [Table 3, Run 14 Dry Restart Slip 4 II-C].

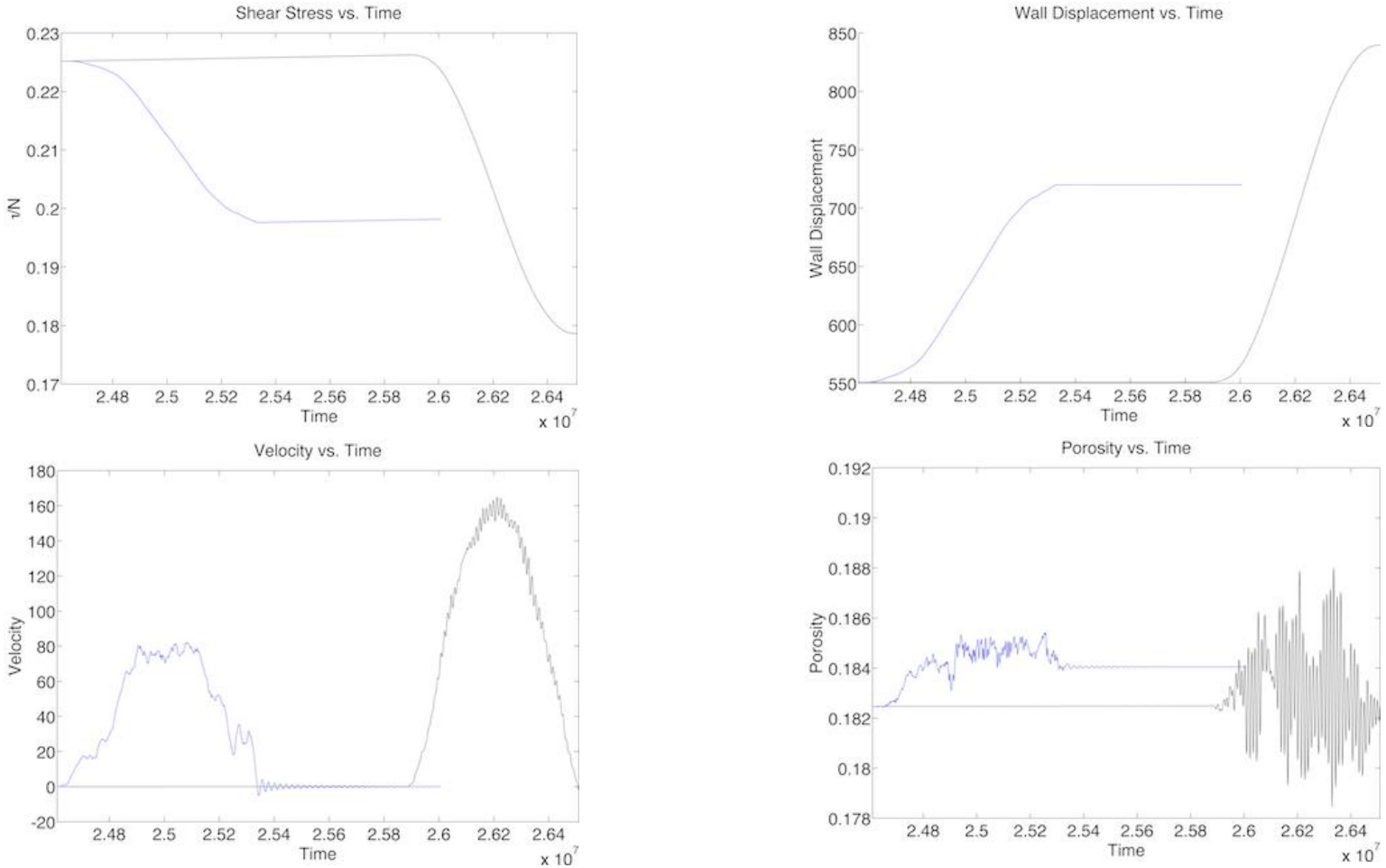

Figure D6. Differences in applied shear stress normalized by the constant effective confining stress, dimensionless velocity, dimensionless displacement, and dimensionless porosity from a drained (black) vs. undrained (blue) simulation. The parameters used in this simulation include: $N=3x10^{-4}$, $V_{sp}=5x10^{-6}$, $k=5x10^{-8}$, and $Perm=1x10^{-5}$. The undrained simulation was classified as a Type I earthquake [Table 3, Run 14 Dry Restart Slip 5 I].

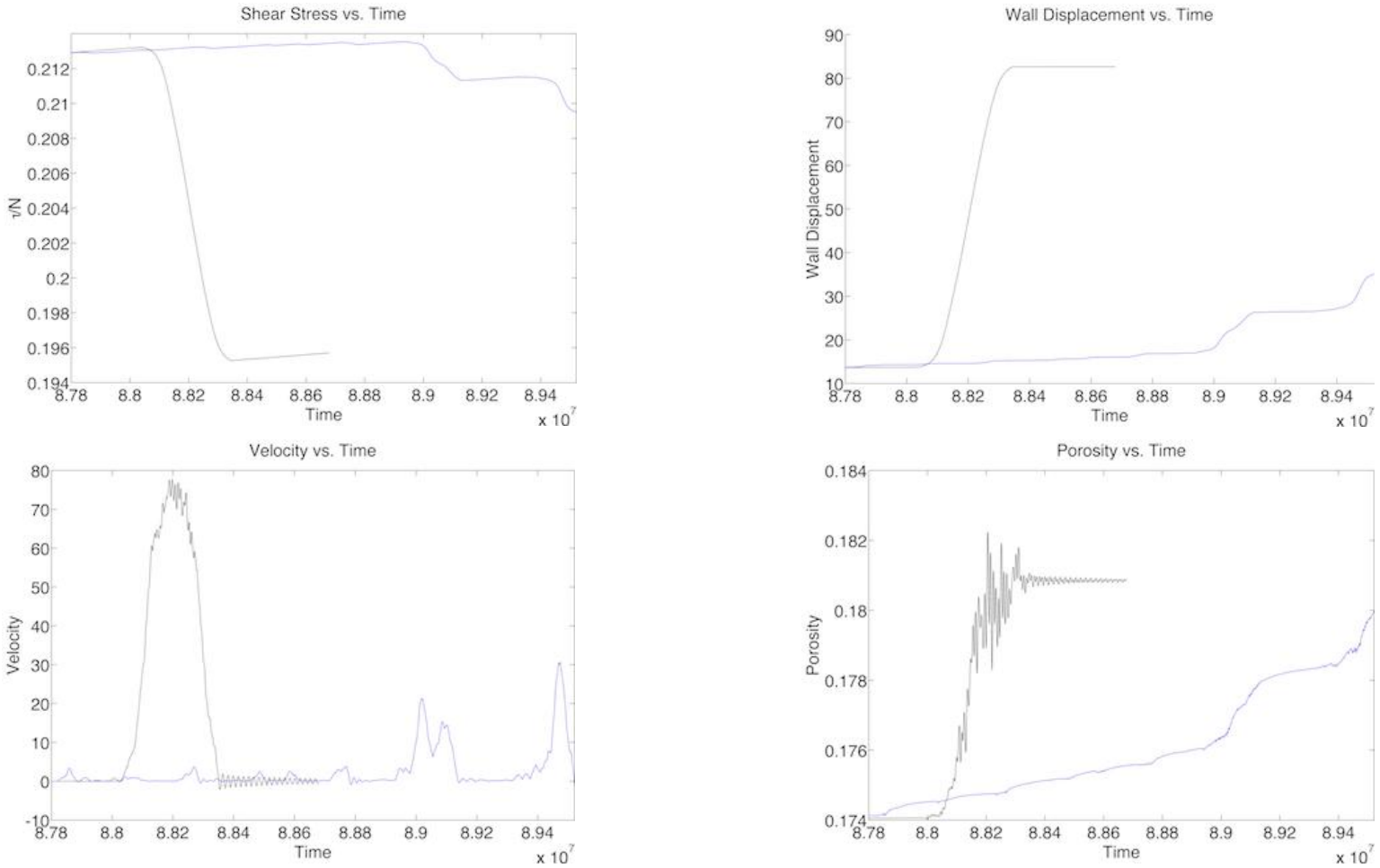

Figure D7. Differences in applied shear stress normalized by the constant effective confining stress, dimensionless velocity, dimensionless displacement, and dimensionless porosity from a drained (black) vs. undrained (blue) simulation. The parameters used in this simulation include: $N=3x10^{-4}$, $V_{sp}=5x10^{-6}$, $k=8x10^{-8}$, and $Perm=1x10^{-5}$. The undrained simulation was classified as a Type II-C earthquake [Table 3, Run 15 Dry Restart6 Slip 1 II-C].

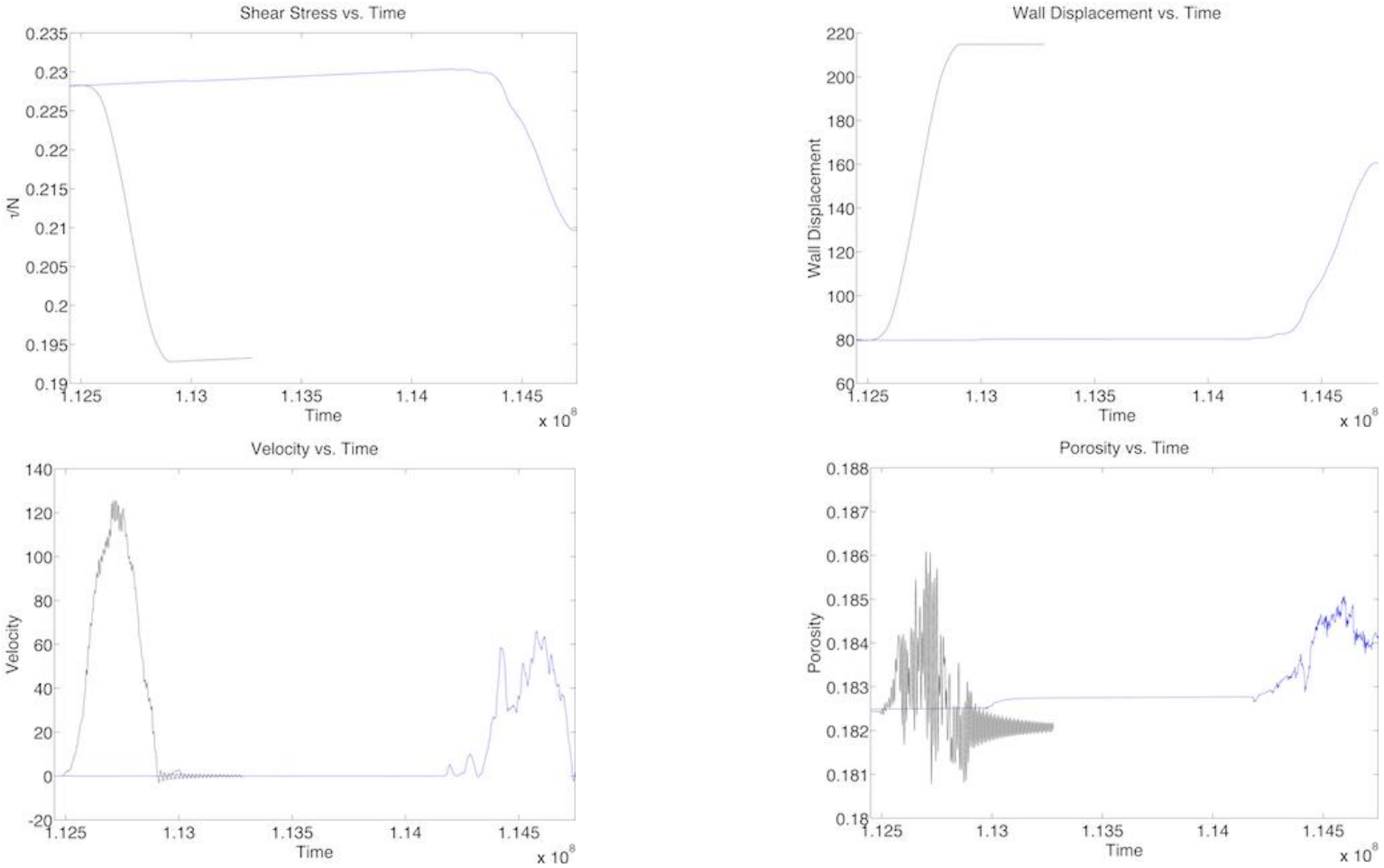

Figure D8. Differences in applied shear stress normalized by the constant effective confining stress, dimensionless velocity, dimensionless displacement, and dimensionless porosity from a drained (black) vs. undrained (blue) simulation. The parameters used in this simulation include: $N=3x10^{-4}$, $V_{sp}=5x10^{-6}$, $k=8x10^{-8}$, and $Perm=1x10^{-5}$. The undrained simulation was classified as a Type II-C earthquake [Table 3, Run 15 Dry Restart6 Slip 2 II-C].

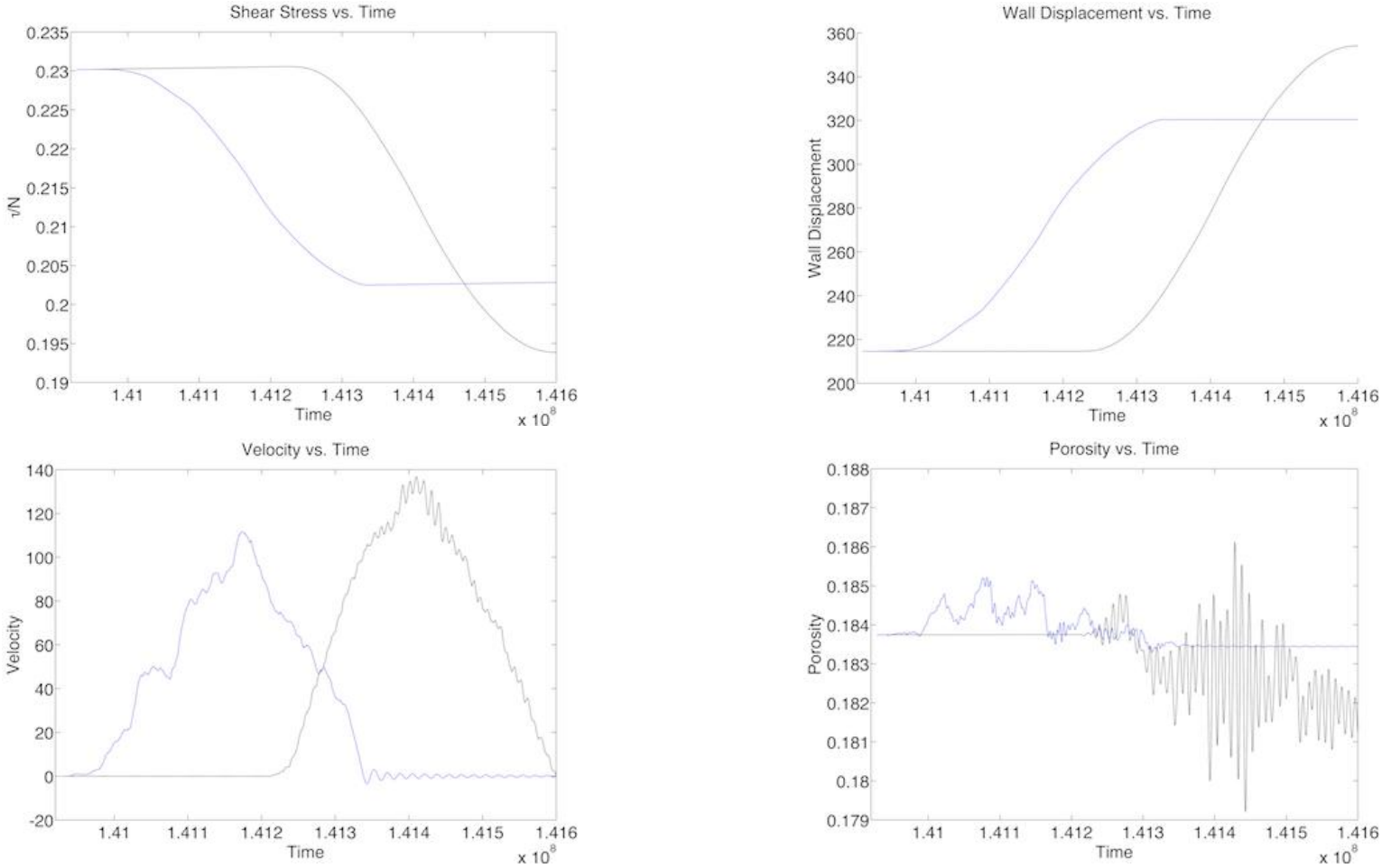

Figure D9. Differences in applied shear stress normalized by the constant effective confining stress, dimensionless velocity, dimensionless displacement, and dimensionless porosity from a drained (black) vs. undrained (blue) simulation. The parameters used in this simulation include: $N=3x10^{-4}$, $V_{sp}=5x10^{-6}$, $k=8x10^{-8}$, and $Perm=1x10^{-5}$. The undrained simulation was classified as a Type I earthquake [Table 3, Run 15 Dry Restart6 Slip 3 I].

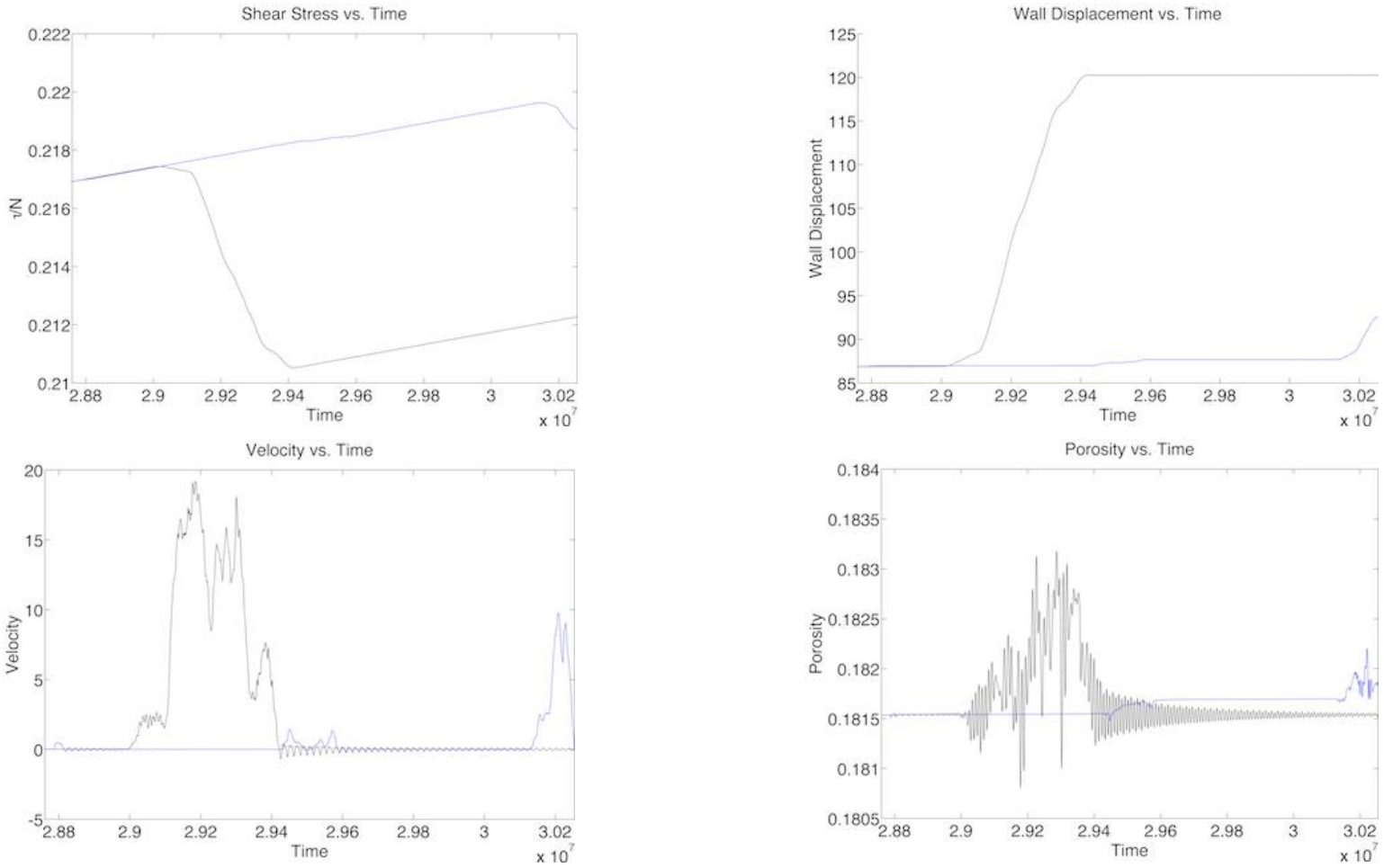

Figure D10. Differences in applied shear stress normalized by the constant effective confining stress, dimensionless velocity, dimensionless displacement, and dimensionless porosity from a drained (black) vs. undrained (blue) simulation. The parameters used in this simulation include: $N=3x10^{-4}$, $V_{sp}=9x10^{-6}$, $k=7x10^{-8}$, and $Perm=1x10^{-5}$. The undrained simulation was classified as a Type II earthquake [Table 3, Run 18 Dry Restart Slip 2 II].

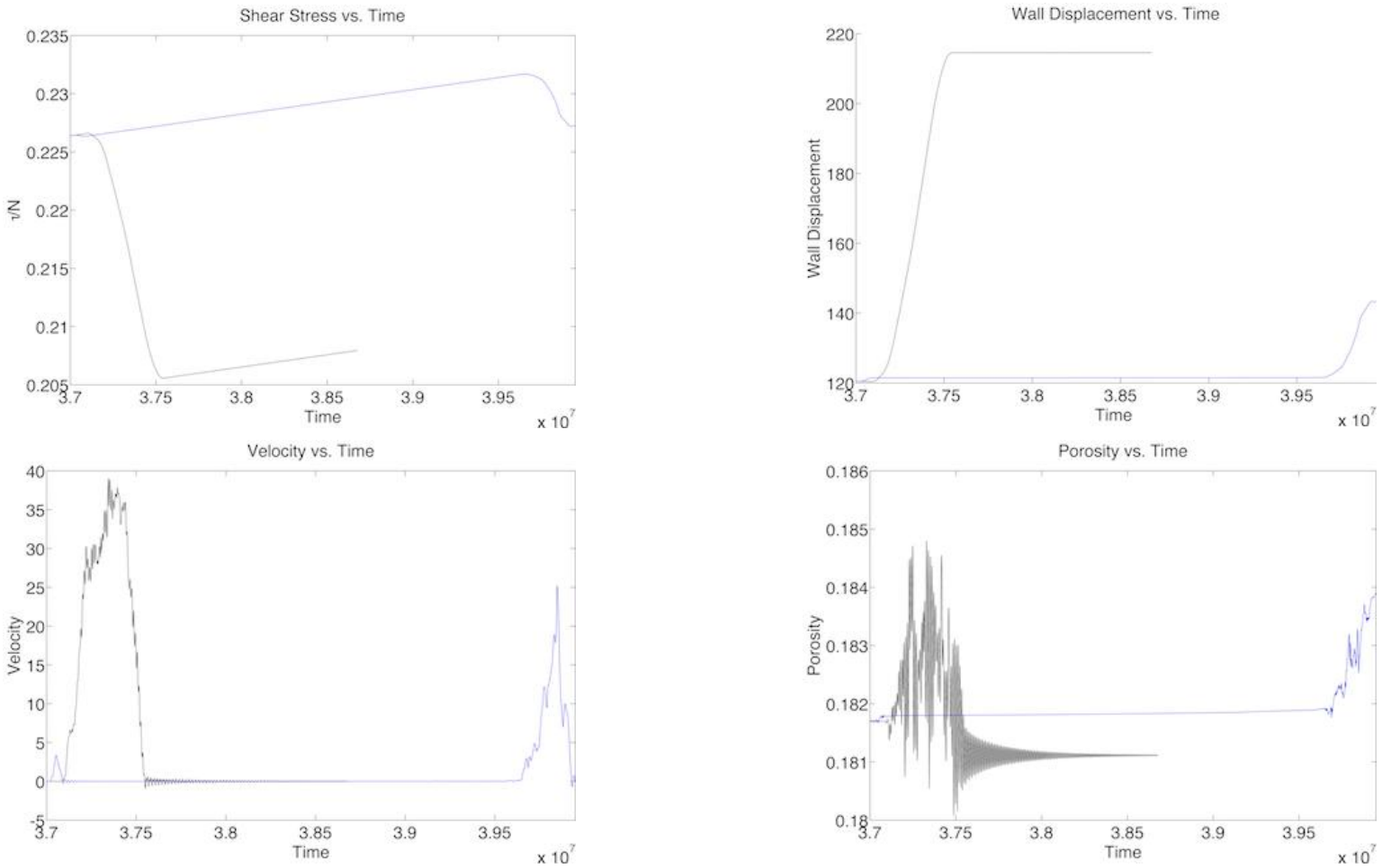

Figure D11. Differences in applied shear stress normalized by the constant effective confining stress, dimensionless velocity, dimensionless displacement, and dimensionless porosity from a drained (black) vs. undrained (blue) simulation. The parameters used in this simulation include: $N=3x10^{-4}$, $V_{sp}=9x10^{-6}$, $k=7x10^{-8}$, and $Perm=1x10^{-5}$. The undrained simulation was classified as a Type II-C earthquake [Table 3, Run 18 Dry Restart Slip 3 II-C].

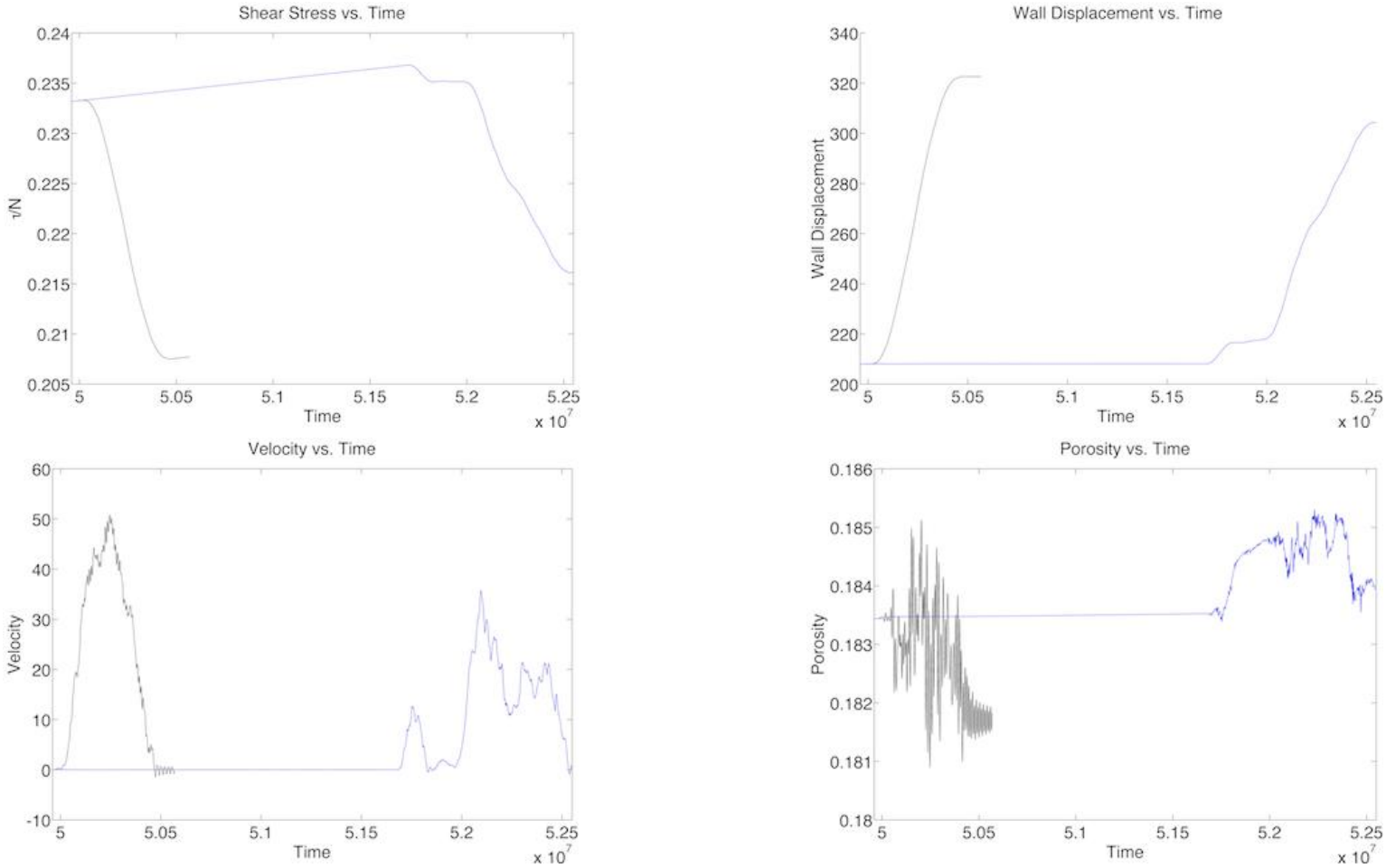

Figure D12. Differences in applied shear stress normalized by the constant effective confining stress, dimensionless velocity, dimensionless displacement, and dimensionless porosity from a drained (black) vs. undrained (blue) simulation. The parameters used in this simulation include: $N=3x10^{-4}$, $V_{sp}=9x10^{-6}$, $k=7x10^{-8}$, and $Perm=1x10^{-5}$. The undrained simulation was classified as a Type II-C earthquake [Table 3, Run 18 Dry Restart Slip 4 II-C].

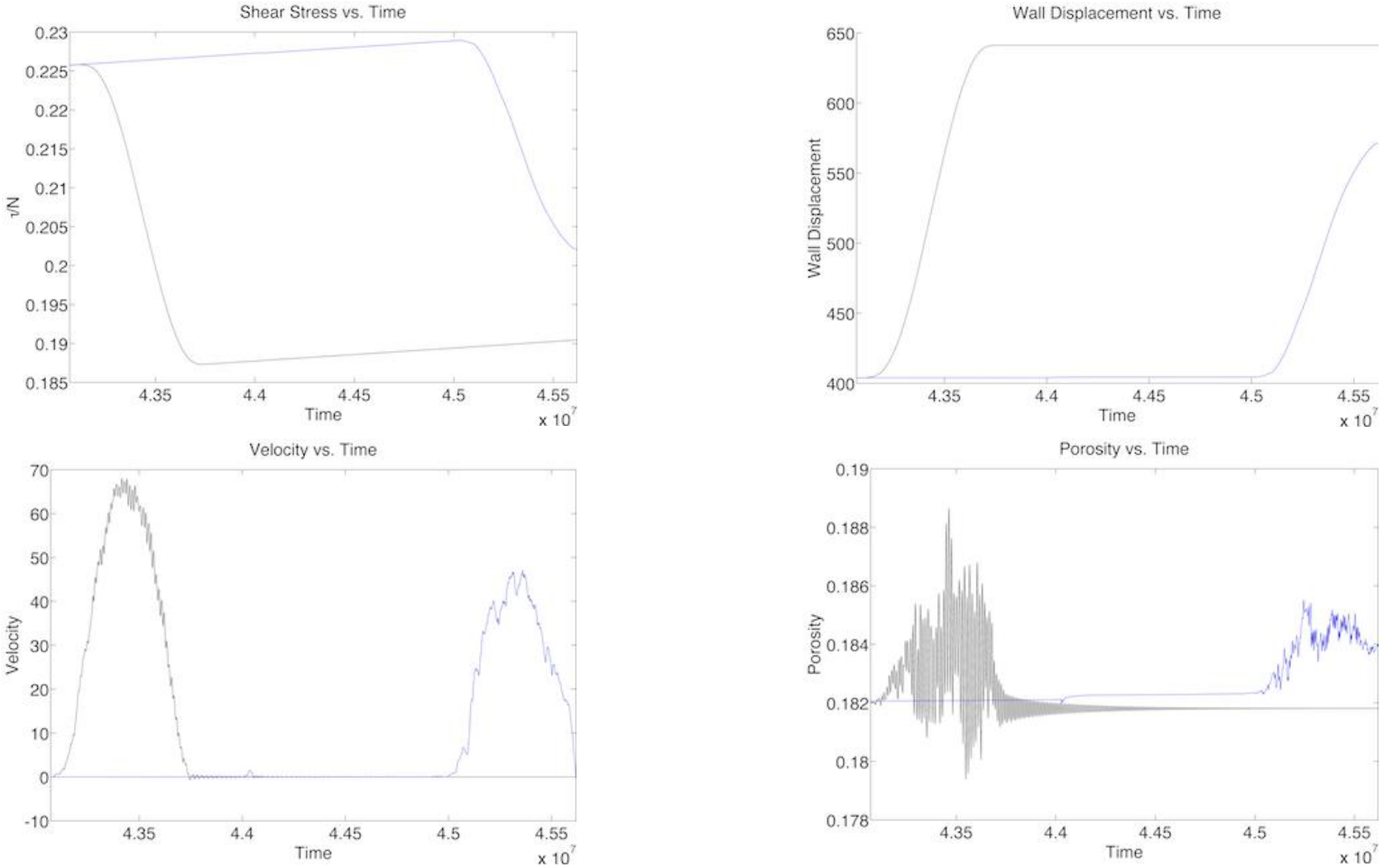

Figure D13. Differences in applied shear stress normalized by the constant effective confining stress, dimensionless velocity, dimensionless displacement, and dimensionless porosity from a drained (black) vs. undrained (blue) simulation. The parameters used in this simulation include: $N=3x10^{-4}$, $V_{sp}=1x10^{-5}$, $k=5x10^{-8}$, and $Perm=1x10^{-5}$. The undrained simulation was classified as a Type II earthquake [Table 3, Run 20 Dry Restart3 Slip 2 II].

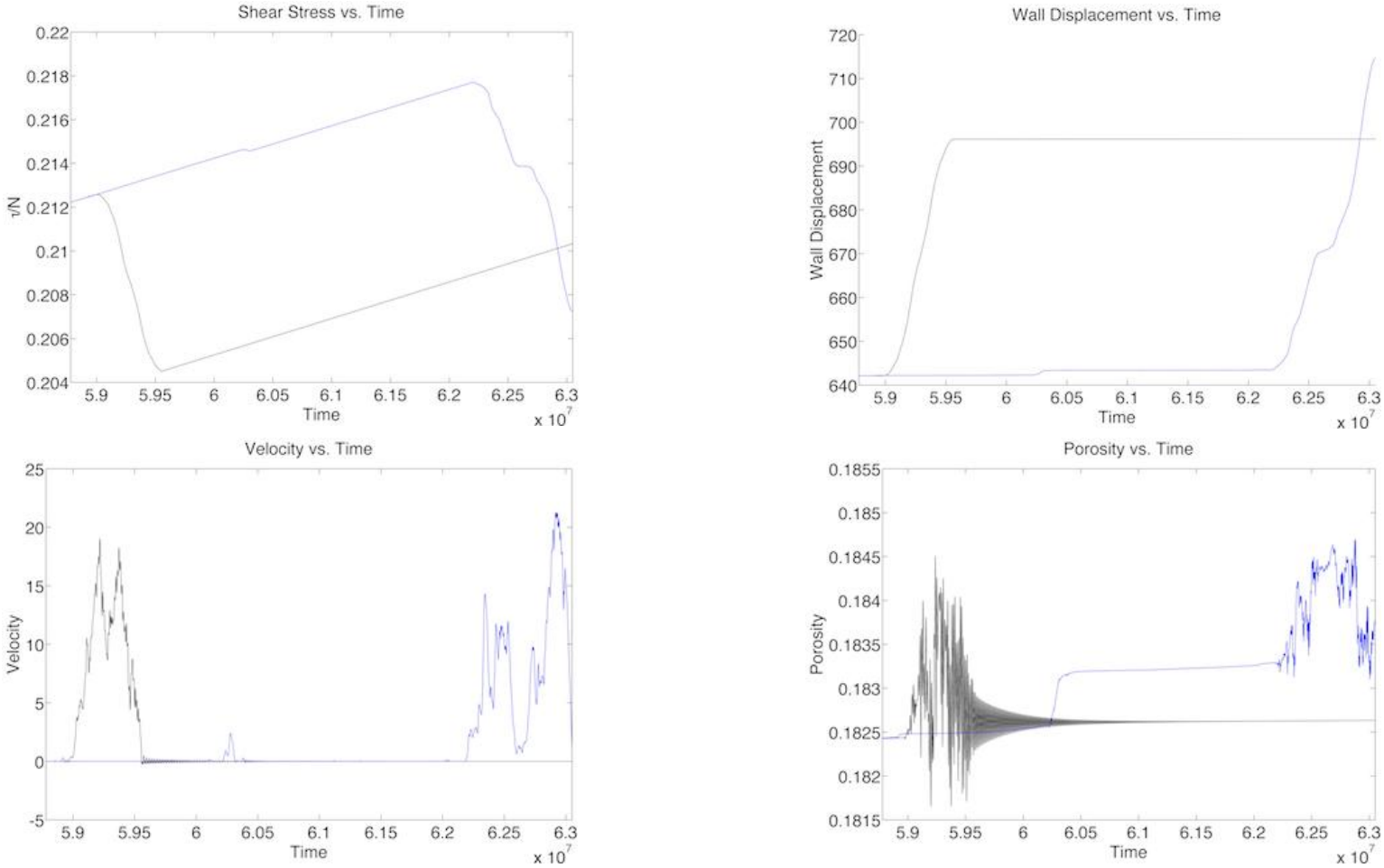

Figure D14. Differences in applied shear stress normalized by the constant effective confining stress, dimensionless velocity, dimensionless displacement, and dimensionless porosity from a drained (black) vs. undrained (blue) simulation. The parameters used in this simulation include: $N=3x10^{-4}$, $V_{sp}=1x10^{-5}$, $k=5x10^{-8}$, and $Perm=1x10^{-5}$. The undrained simulation was classified as a Type II-C earthquake [Table 3, Run 20 Dry Restart3 Slip 3 II-C].

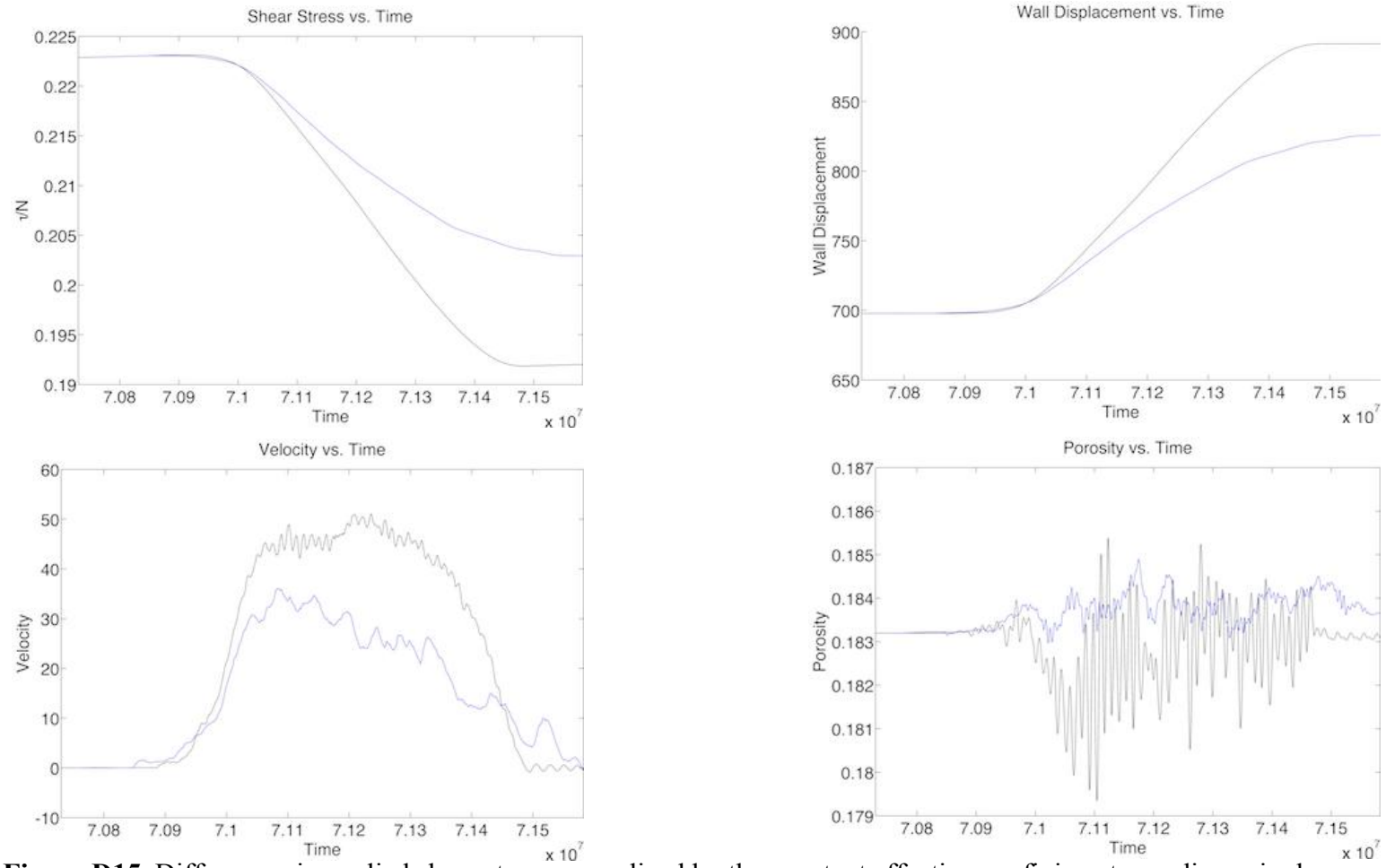

Figure D15. Differences in applied shear stress normalized by the constant effective confining stress, dimensionless velocity, dimensionless displacement, and dimensionless porosity from a drained (black) vs. undrained (blue) simulation. The parameters used in this simulation include: $N=3x10^{-4}$, $V_{sp}=1x10^{-5}$, $k=5x10^{-8}$, and $Perm=1x10^{-5}$. The undrained simulation was classified as a Type I earthquake [Table 3, Run 20 Dry Restart3 Slip 4 I].

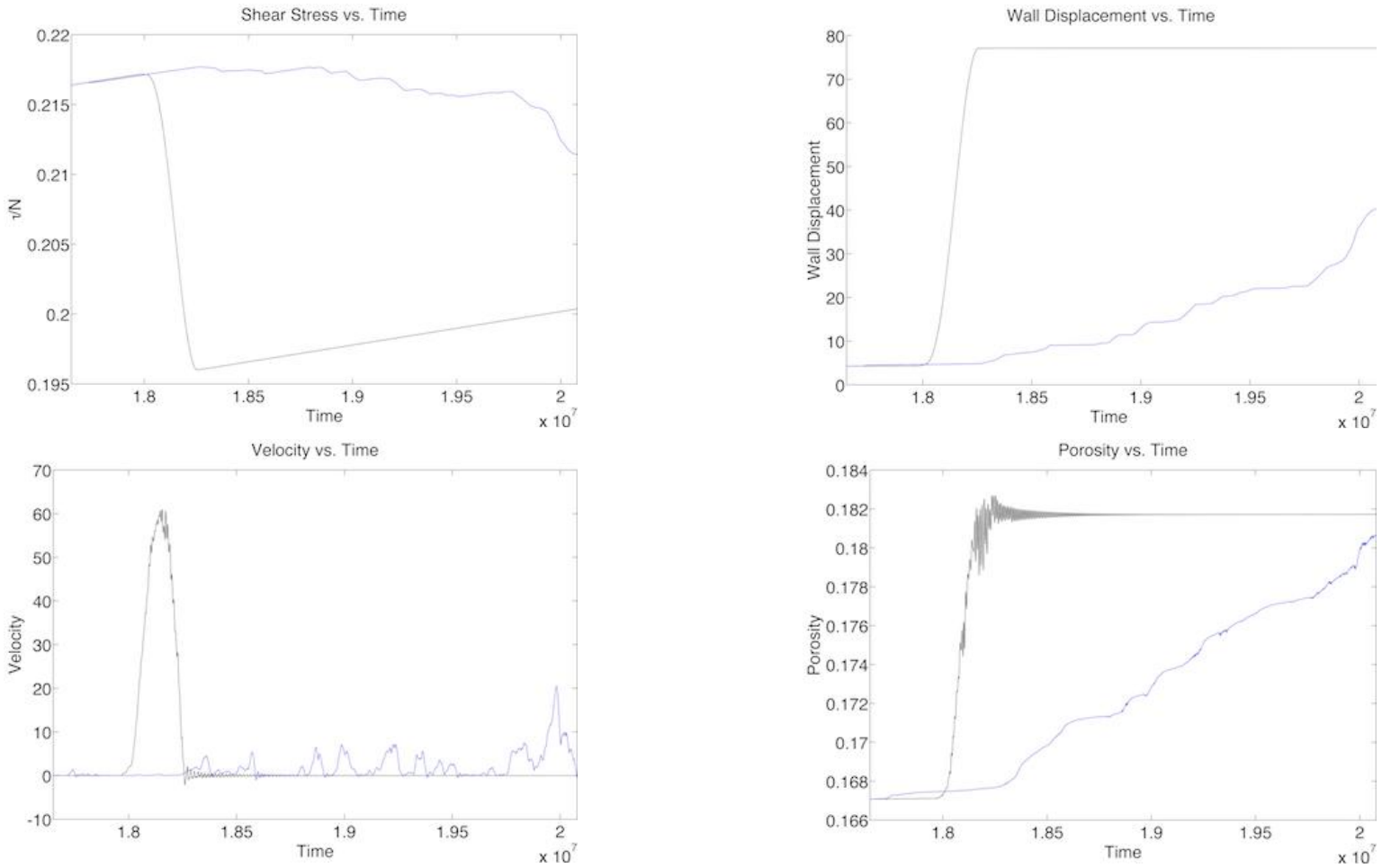

Figure D16. Differences in applied shear stress normalized by the constant effective confining stress, dimensionless velocity, dimensionless displacement, and dimensionless porosity from a drained (black) vs. undrained (blue) simulation. The parameters used in this simulation include: $N=3x10^{-4}$, $V_{sp}=8x10^{-6}$, $k=9x10^{-8}$, and $Perm=1x10^{-5}$. The undrained simulation was classified as a Type II-C earthquake [Table 3, Run 21 Dry Restart Slip 1 II-C].

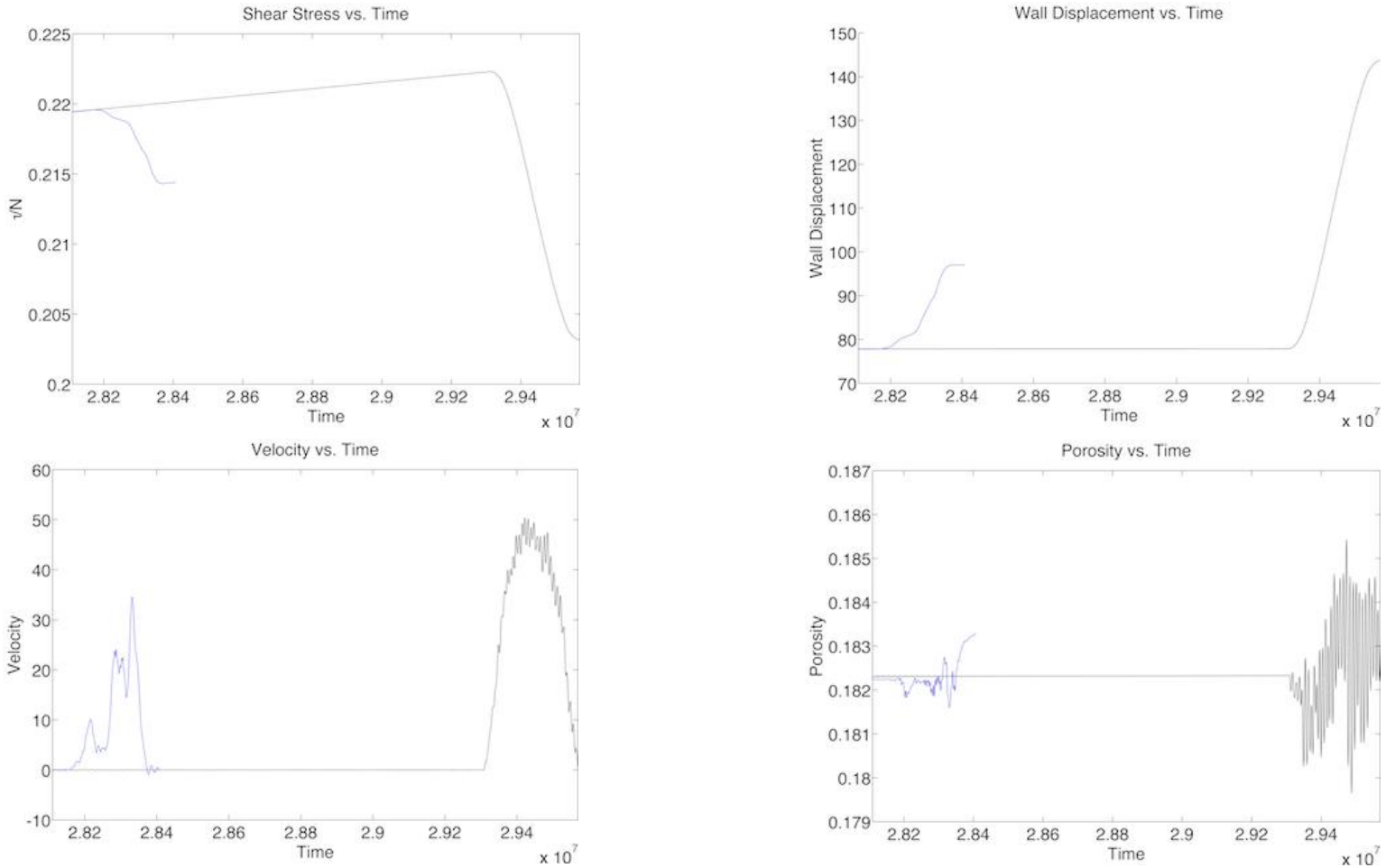

Figure D17. Differences in applied shear stress normalized by the constant effective confining stress, dimensionless velocity, dimensionless displacement, and dimensionless porosity from a drained (black) vs. undrained (blue) simulation. The parameters used in this simulation include: $N=3x10^{-4}$, $V_{sp}=8x10^{-6}$, $k=9x10^{-8}$, and $Perm=1x10^{-5}$. The undrained simulation was classified as a Type I-C earthquake [Table 3, Run 21 Dry Restart Slip 2 I-C].

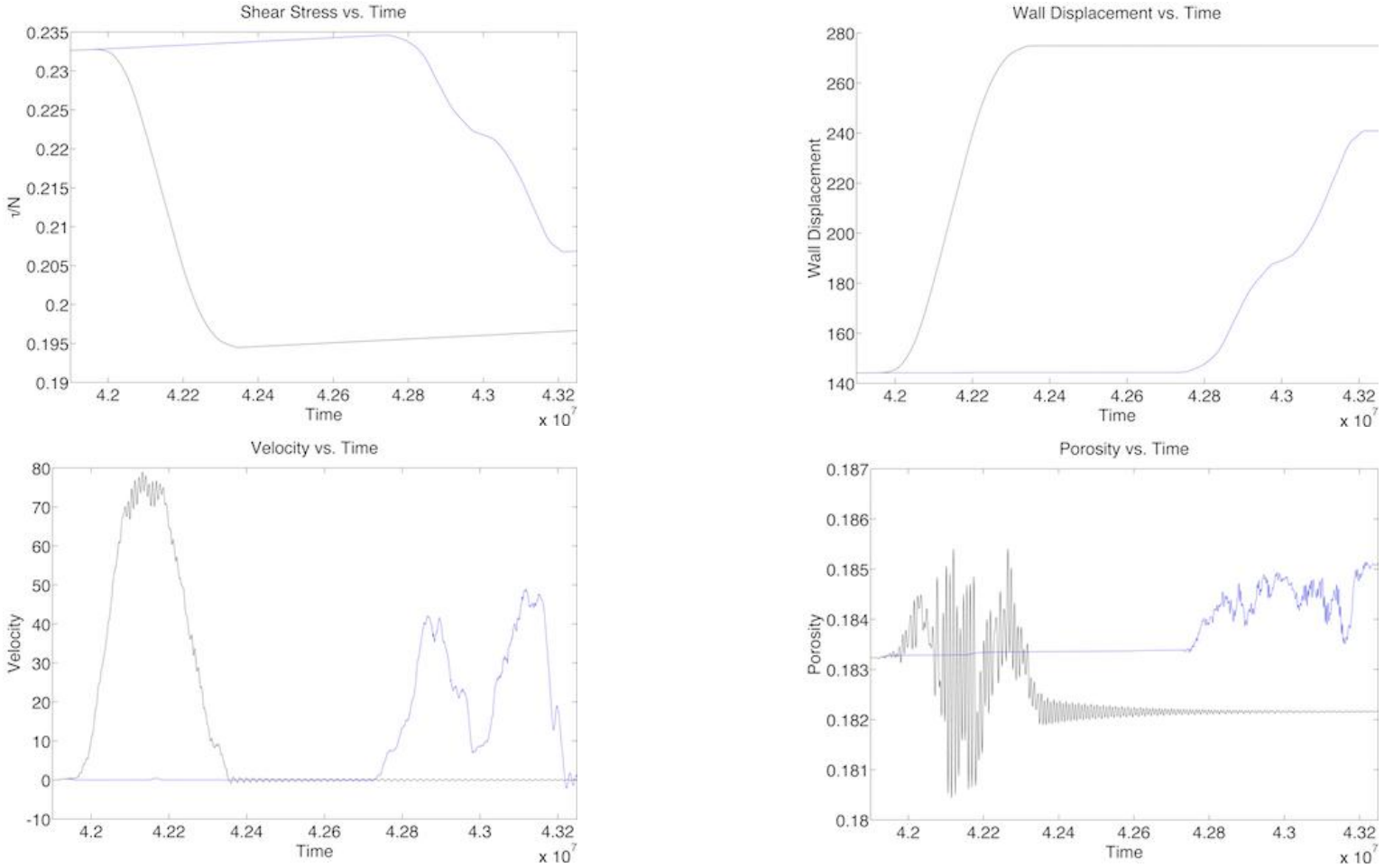

Figure D18. Differences in applied shear stress normalized by the constant effective confining stress, dimensionless velocity, dimensionless displacement, and dimensionless porosity from a drained (black) vs. undrained (blue) simulation. The parameters used in this simulation include: $N=3x10^{-4}$, $V_{sp}=8x10^{-6}$, $k=9x10^{-8}$, and $Perm=1x10^{-5}$. The undrained simulation was classified as a Type II-C earthquake [Table 3, Run 21 Dry Restart Slip 4 II-C].

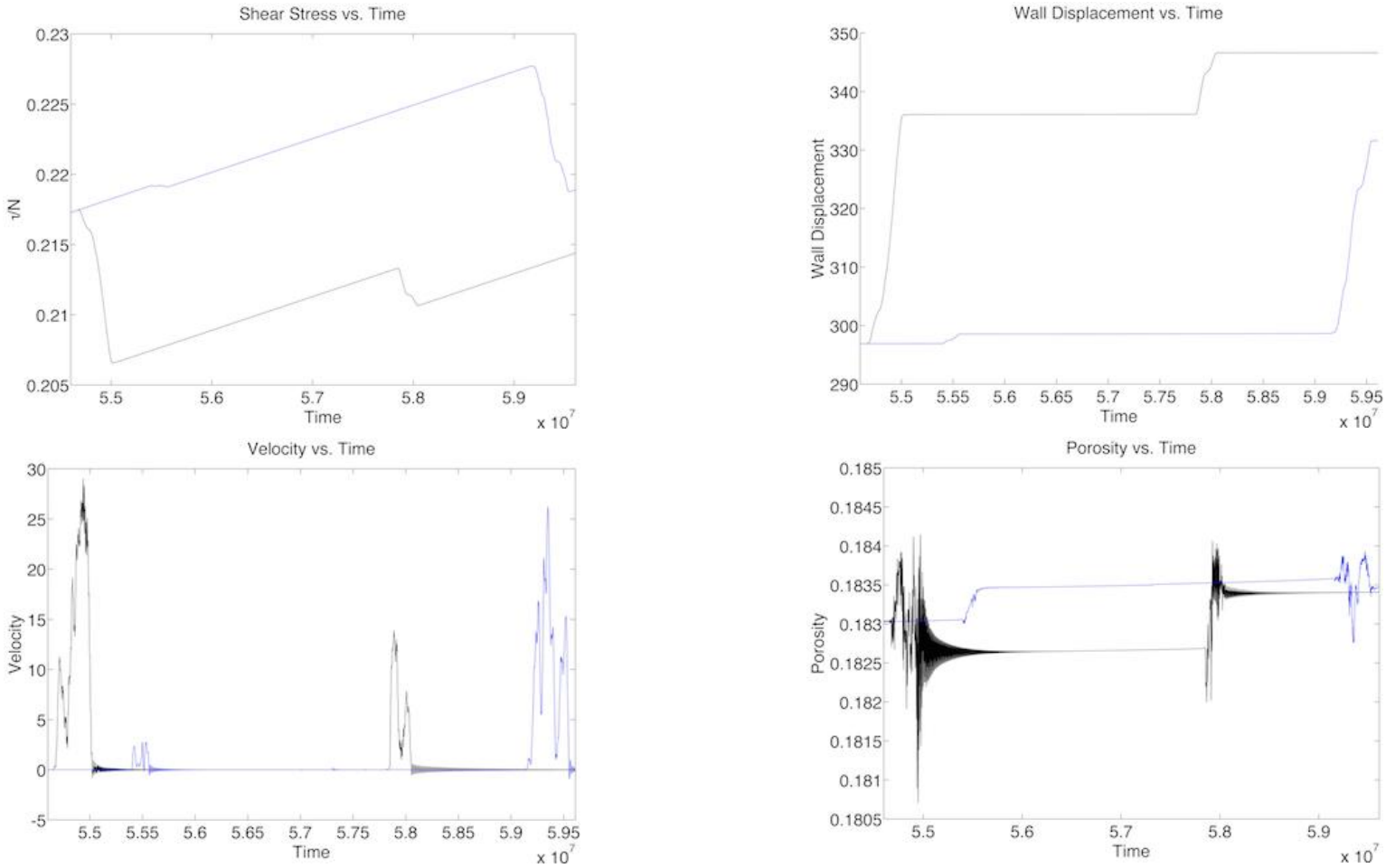

Figure D19. Differences in applied shear stress normalized by the constant effective confining stress, dimensionless velocity, dimensionless displacement, and dimensionless porosity from a drained (black) vs. undrained (blue) simulation. The parameters used in this simulation include: $N=3x10^{-4}$, $V_{sp}=8x10^{-6}$, $k=9x10^{-8}$, and $Perm=1x10^{-5}$. The undrained simulation was classified as a Type II-C earthquake [Table 3, Run 21 Dry Restart Slip 5 II-C].

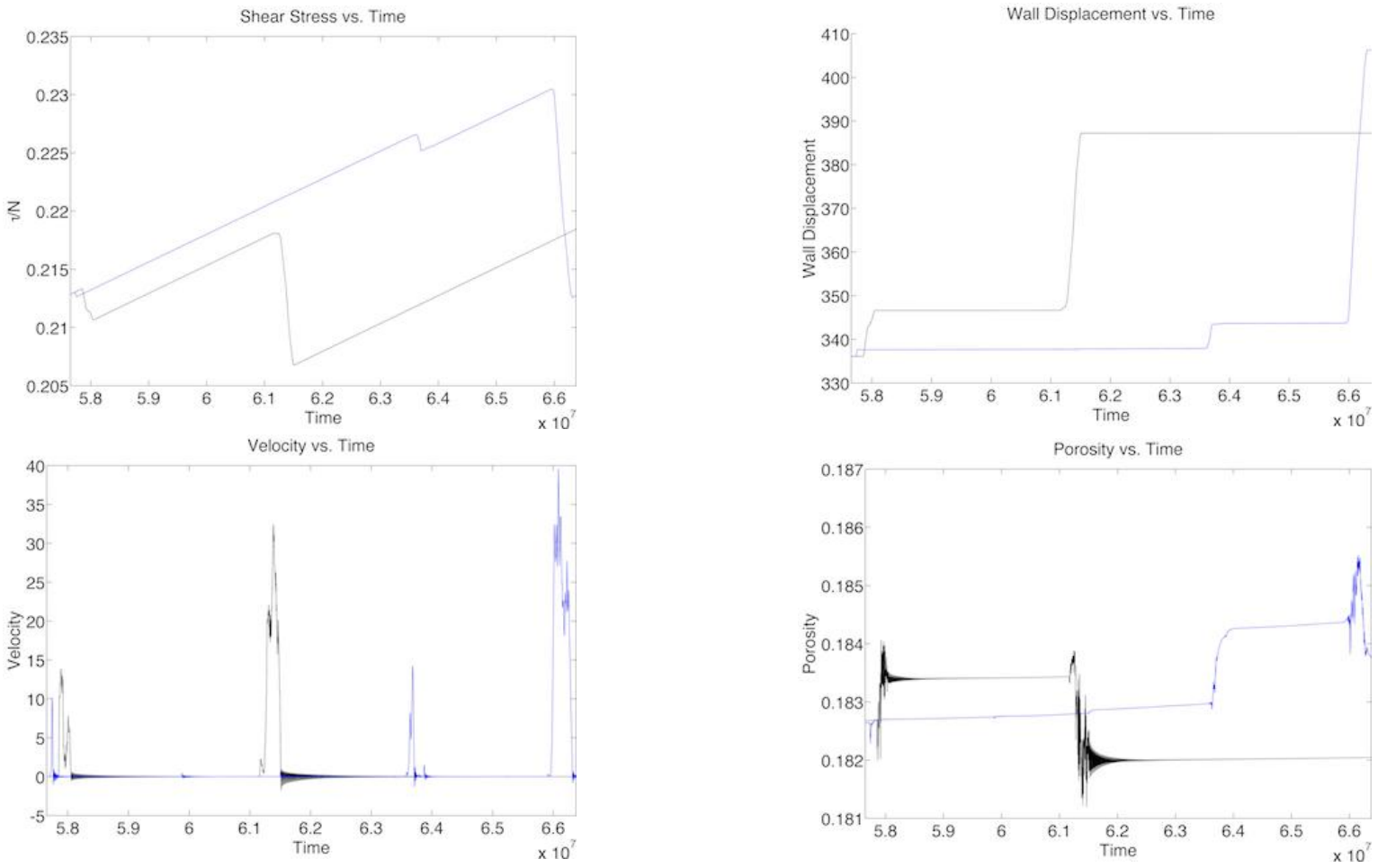

Figure D20. Differences in applied shear stress normalized by the constant effective confining stress, dimensionless velocity, dimensionless displacement, and dimensionless porosity from a drained (black) vs. undrained (blue) simulation. The parameters used in this simulation include: $N=3x10^{-4}$, $V_{sp}=8x10^{-6}$, $k=9x10^{-8}$, and $Perm=1x10^{-5}$. The undrained simulation was classified as a Type II earthquake [Table 3, Run 21 Dry Restart Slip 6 II].

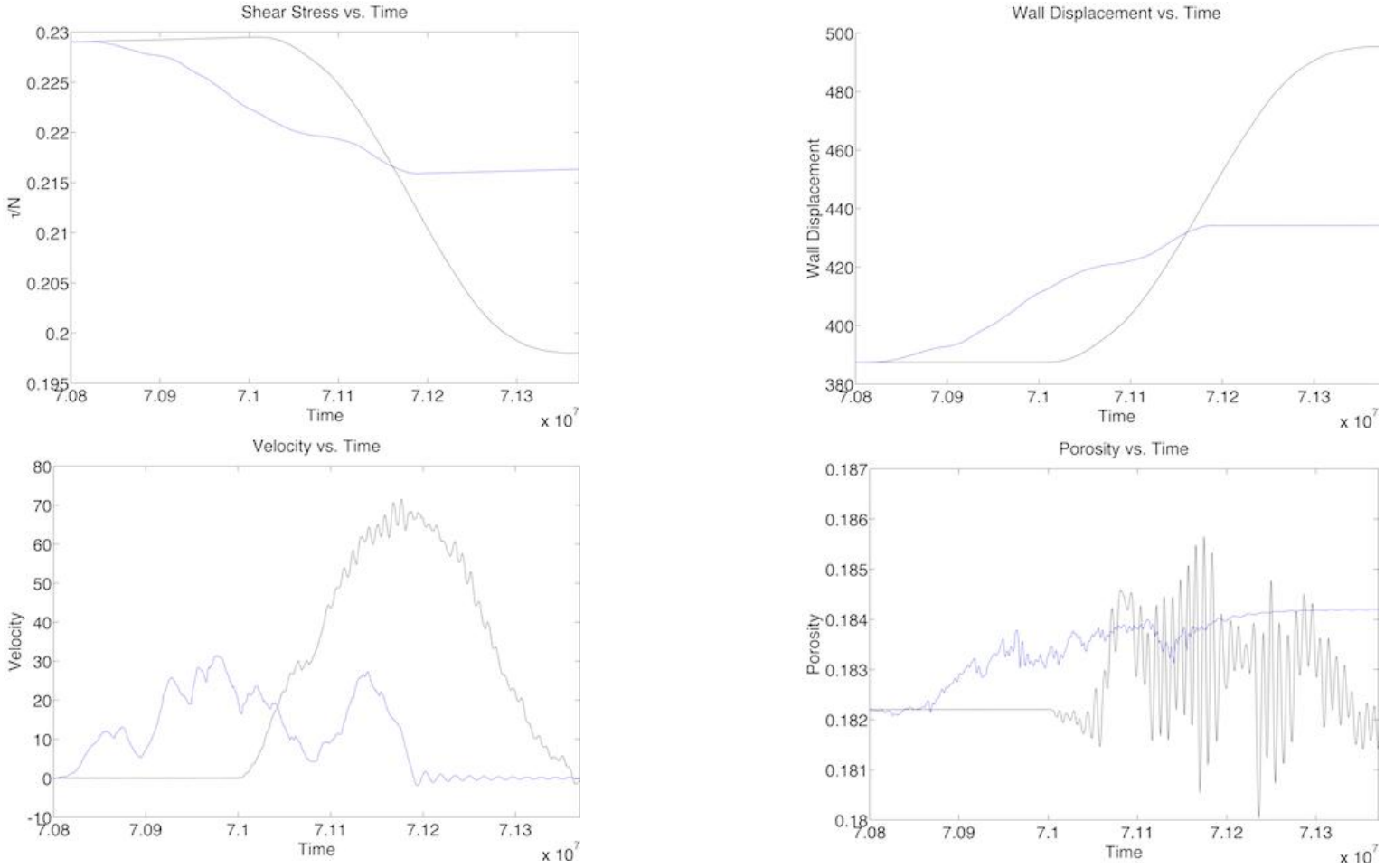

Figure D21. Differences in applied shear stress normalized by the constant effective confining stress, dimensionless velocity, dimensionless displacement, and dimensionless porosity from a drained (black) vs. undrained (blue) simulation. The parameters used in this simulation include: $N=3x10^{-4}$, $V_{sp}=8x10^{-6}$, $k=9x10^{-8}$, and $Perm=1x10^{-5}$. The undrained simulation was classified as a Type I-C earthquake [Table 3, Run 21 Dry Restart Slip 8 I-C].

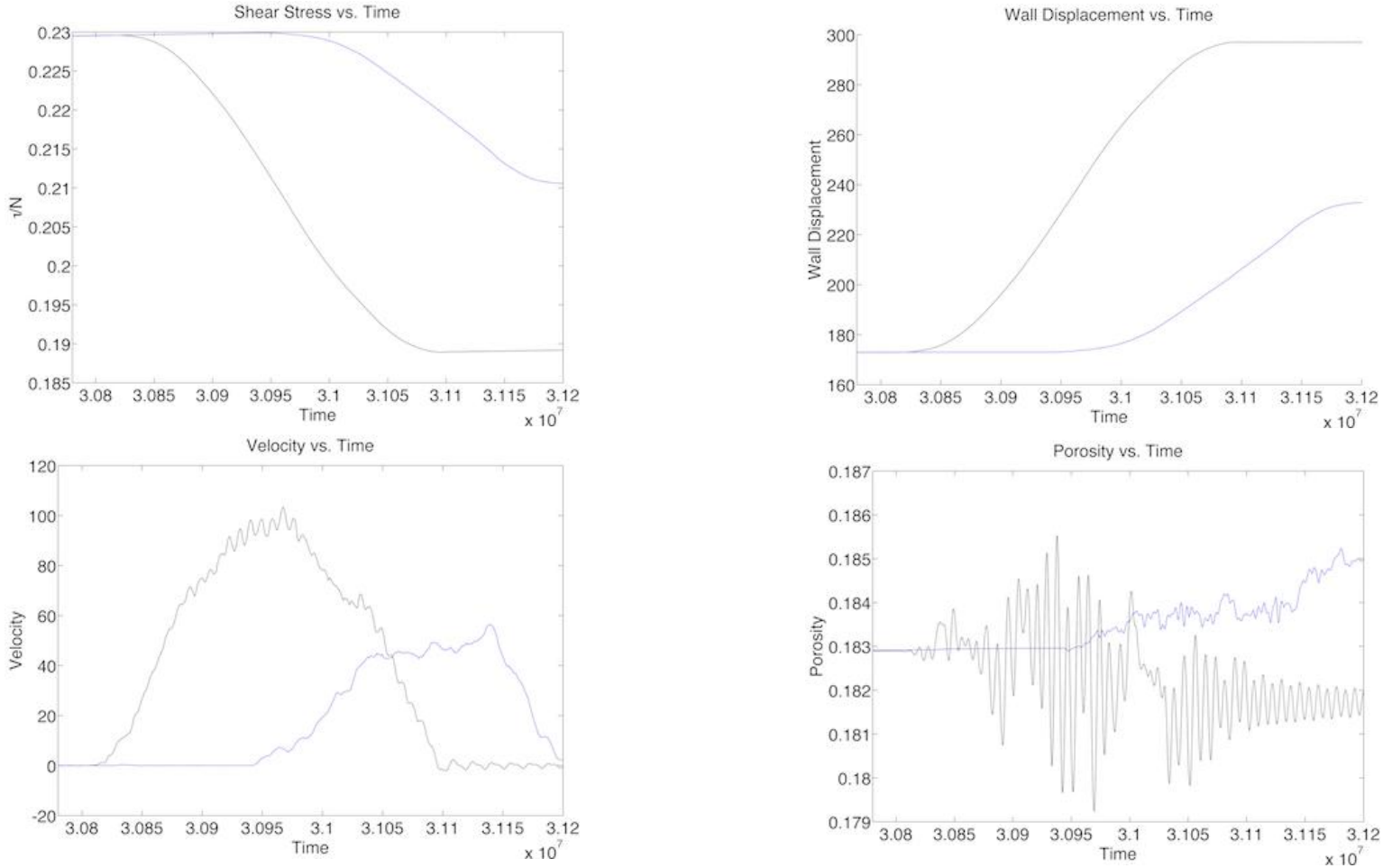

Figure D22. Differences in applied shear stress normalized by the constant effective confining stress, dimensionless velocity, dimensionless displacement, and dimensionless porosity from a drained (black) vs. undrained (blue) simulation. The parameters used in this simulation include: $N=3x10^{-4}$, $V_{sp}=7.5x10^{-6}$, $k=1x10^{-7}$, and $Perm=1x10^{-5}$. The undrained simulation was classified as a Type II earthquake [Table 3, Run 22 Dry Restart Slip t=3E7 II].

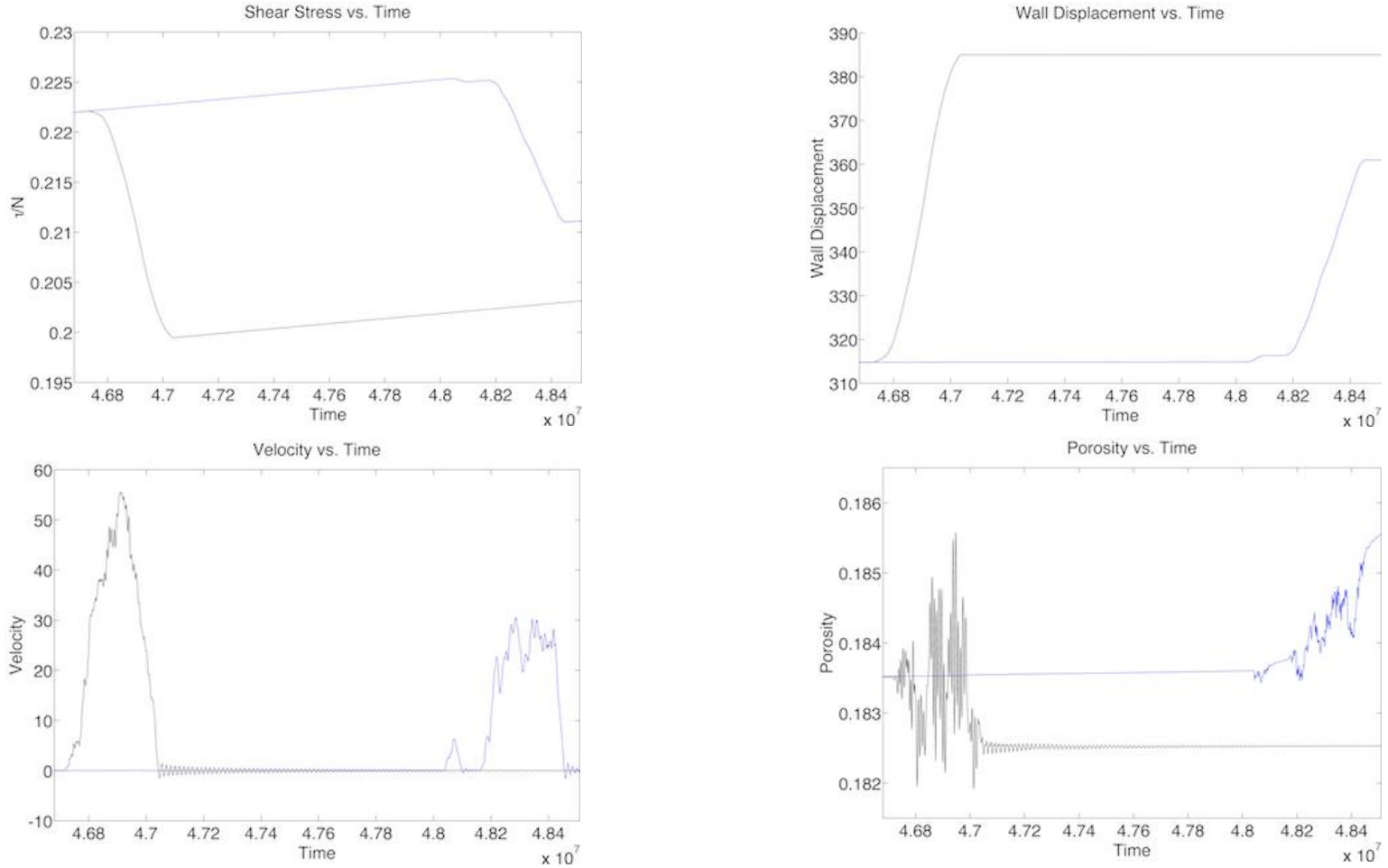

Figure D23. Differences in applied shear stress normalized by the constant effective confining stress, dimensionless velocity, dimensionless displacement, and dimensionless porosity from a drained (black) vs. undrained (blue) simulation. The parameters used in this simulation include: $N=3\times10^{-4}$, $V_{sp}=7.5\times10^{-6}$, $k=1\times10^{-7}$, and $Perm=1\times10^{-5}$. The undrained simulation was classified as a Type II-C earthquake [Table 3, Run 22 Dry Restart Slip t=4.65E7 II-C].

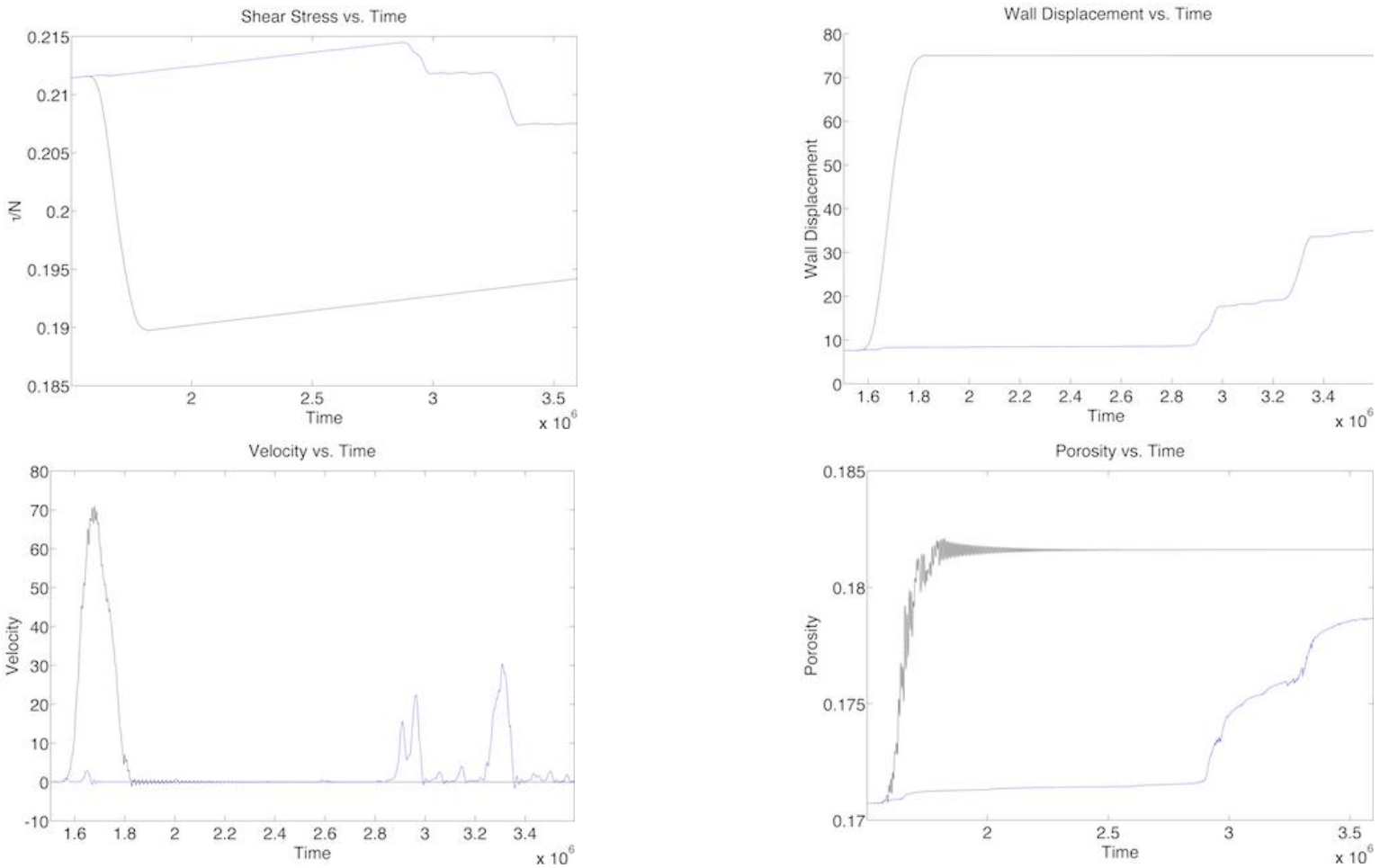

Figure D24. Differences in applied shear stress normalized by the constant effective confining stress, dimensionless velocity, dimensionless displacement, and dimensionless porosity from a drained (black) vs. undrained (blue) simulation. The parameters used in this simulation include: $N=3x10^{-4}$, $V_{sp}=7.5x10^{-6}$, $k=1x10^{-7}$, and $Perm=1x10^{-5}$. The undrained simulation was classified as a Type II-C earthquake [Table 3, Run 22 Dry Restart Slip 1 II-C].

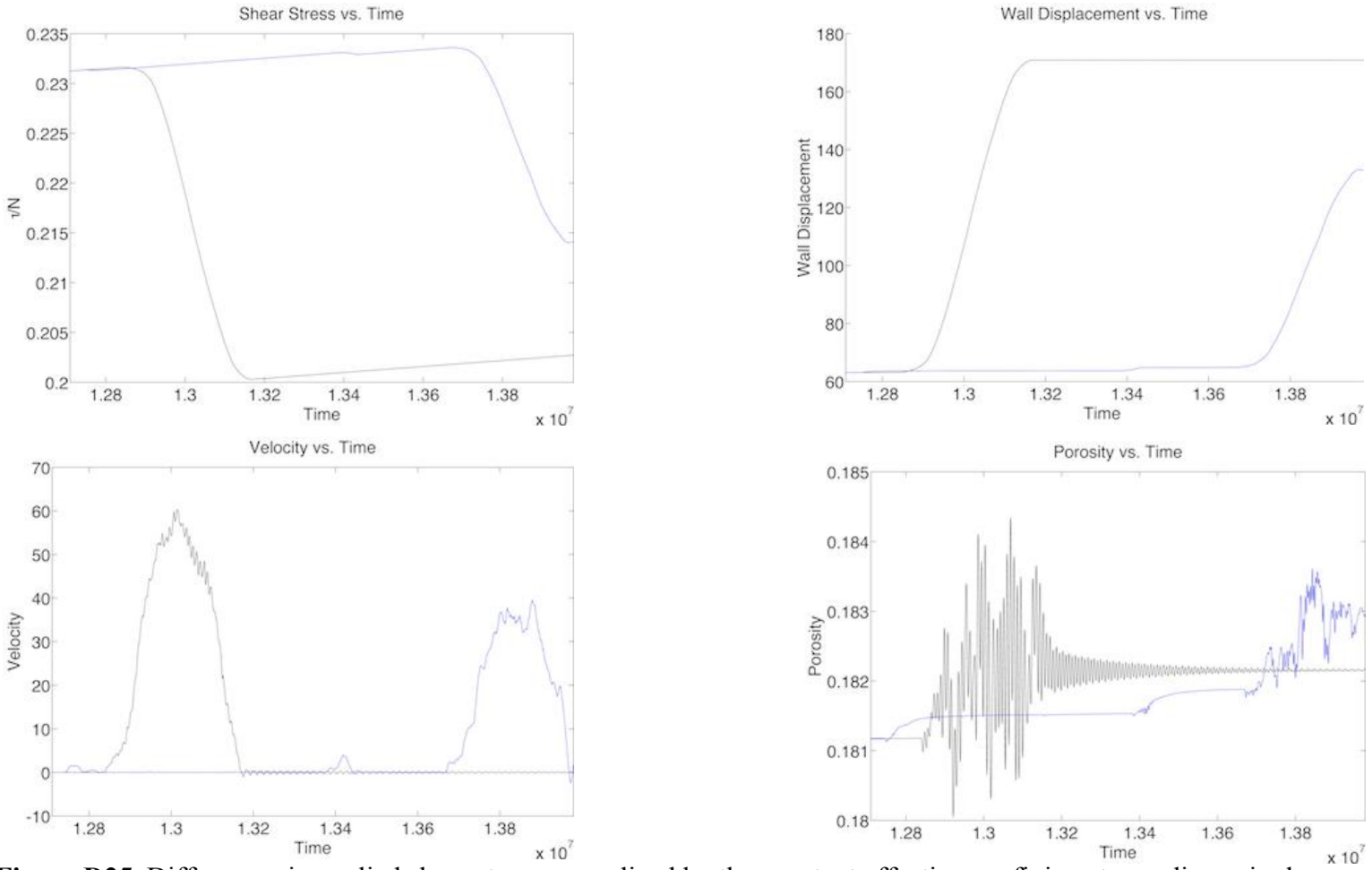

Figure D25. Differences in applied shear stress normalized by the constant effective confining stress, dimensionless velocity, dimensionless displacement, and dimensionless porosity from a drained (black) vs. undrained (blue) simulation. The parameters used in this simulation include: $N=3x10^{-4}$, $V_{sp}=1x10^{-5}$, $k=9x10^{-8}$, and $Perm=1x10^{-5}$. The undrained simulation was classified as a Type II earthquake [Table 3, Run 23 Dry Restart Slip 1.3E7 II].

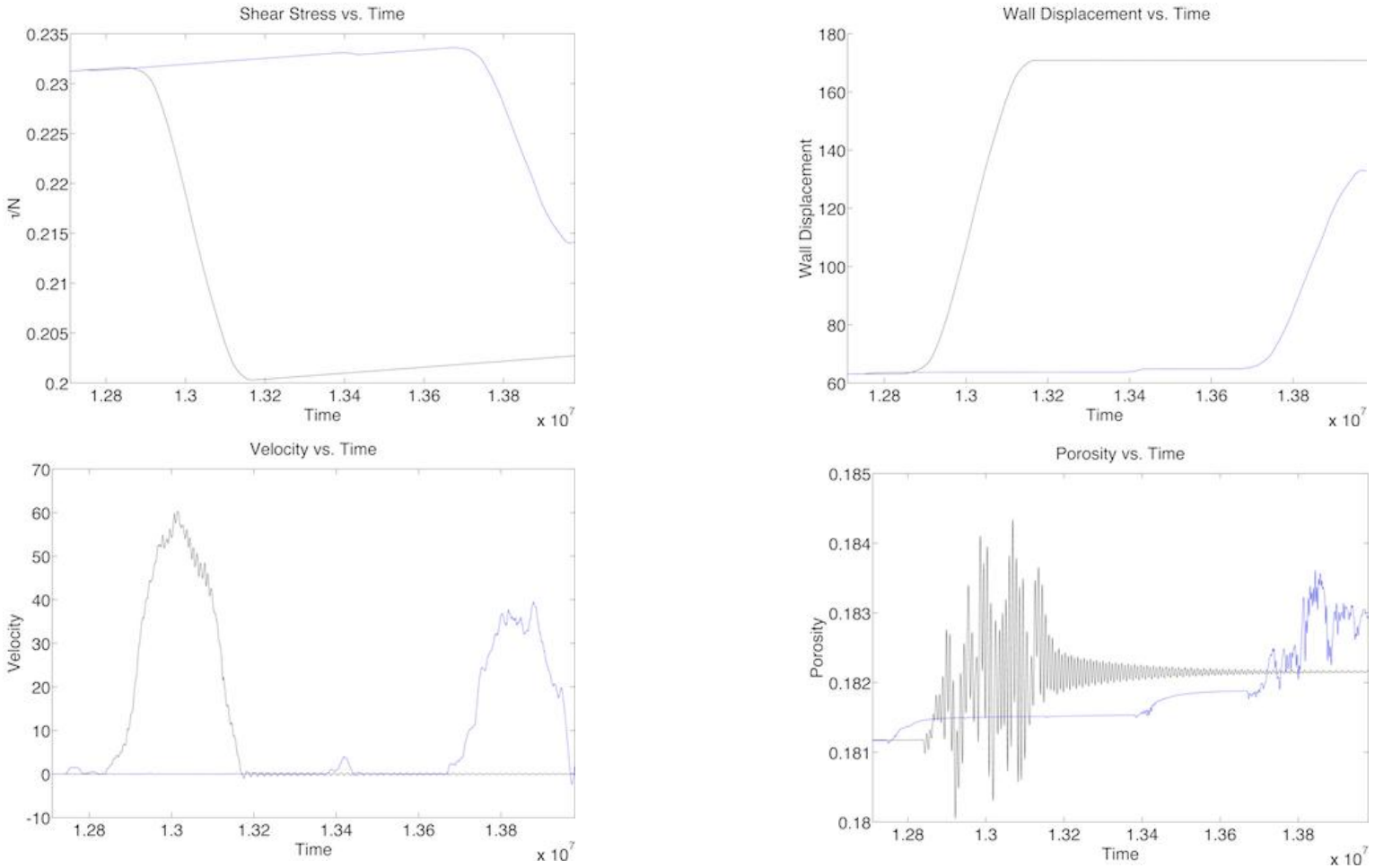

Figure D26. Differences in applied shear stress normalized by the constant effective confining stress, dimensionless velocity, dimensionless displacement, and dimensionless porosity from a drained (black) vs. undrained (blue) simulation. The parameters used in this simulation include: $N=3x10^{-4}$, $V_{sp}=1x10^{-5}$, $k=9x10^{-8}$, and $Perm=1x10^{-5}$. The undrained simulation was classified as a Type II-C earthquake [Table 3, Run 23 Dry Slip 1 II-C].

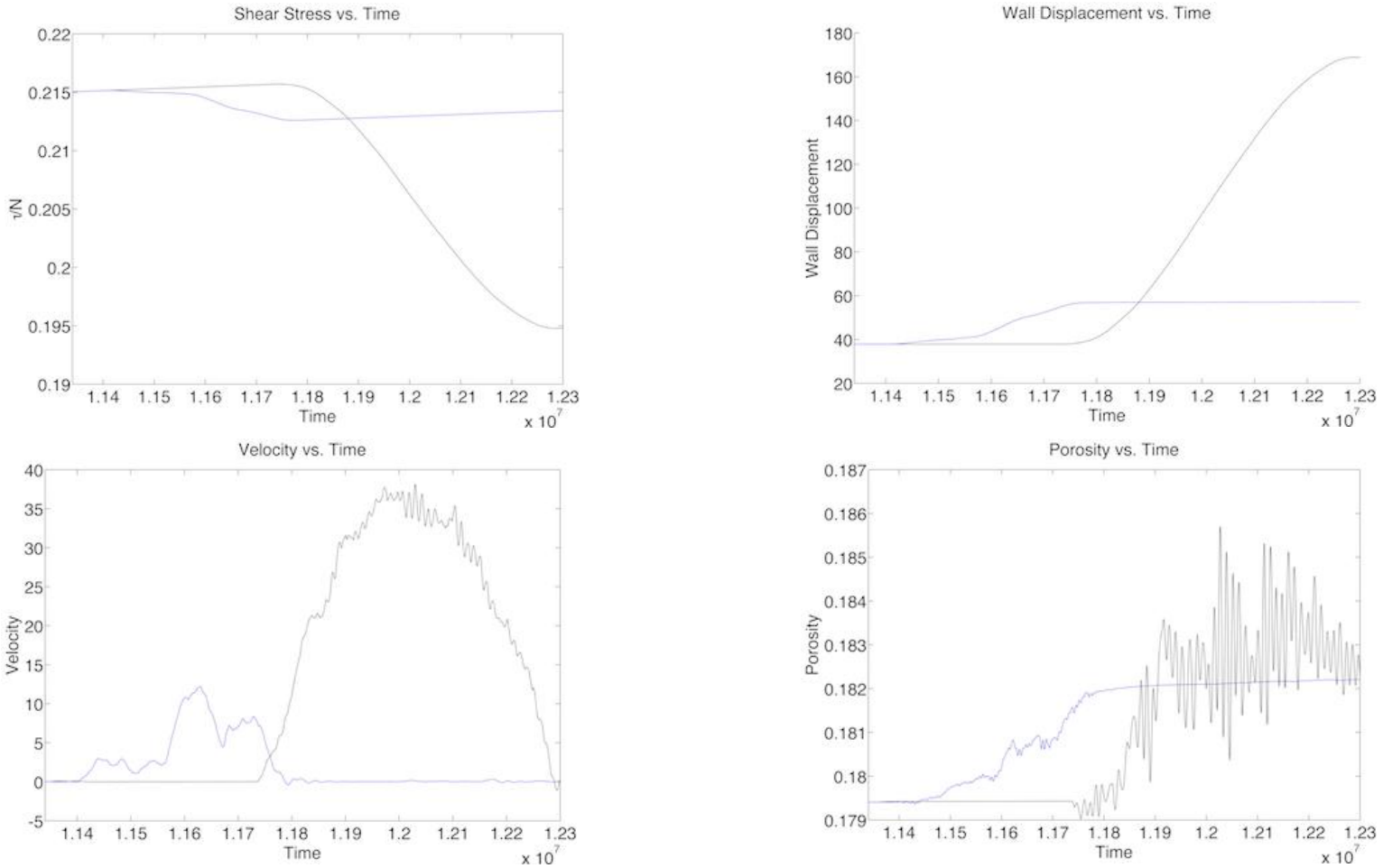

Figure D27. Differences in applied shear stress normalized by the constant effective confining stress, dimensionless velocity, dimensionless displacement, and dimensionless porosity from a drained (black) vs. undrained (blue) simulation. The parameters used in this simulation include: $N=3x10^{-4}$, $V_{sp}=1x10^{-5}$, $k=5x10^{-8}$, and $Perm=1x10^{-5}$. The undrained simulation was classified as a Type I-C earthquake [Table 3, Run 24 Dry Restart Slip 2 I-C].

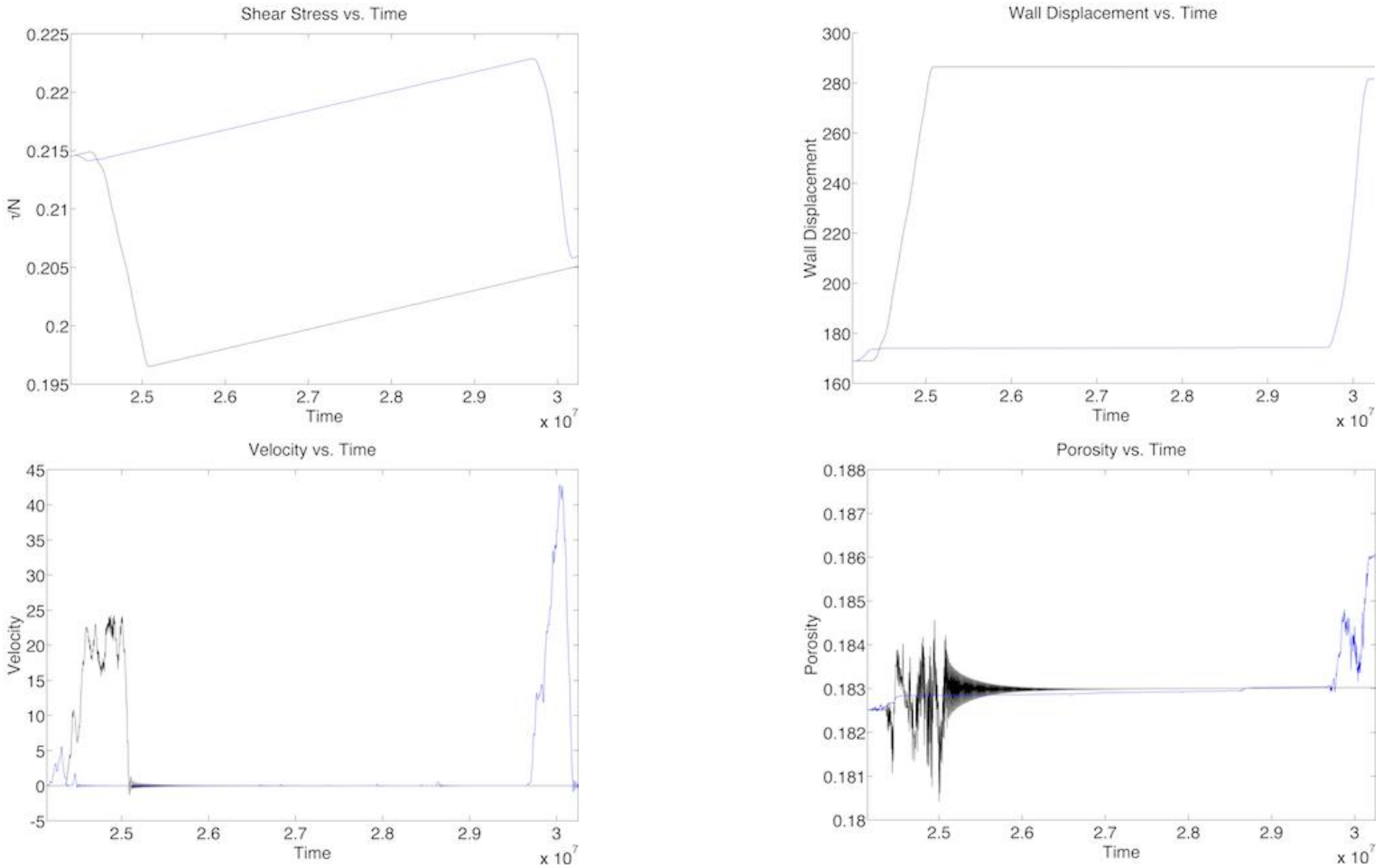

Figure D28. Differences in applied shear stress normalized by the constant effective confining stress, dimensionless velocity, dimensionless displacement, and dimensionless porosity from a drained (black) vs. undrained (blue) simulation. The parameters used in this simulation include: $N=3x10^{-4}$, $V_{sp}=1x10^{-5}$, $k=5x10^{-8}$, and $Perm=1x10^{-5}$. The undrained simulation was classified as a Type II earthquake [Table 3, Run 24 Dry Slip 3 II].

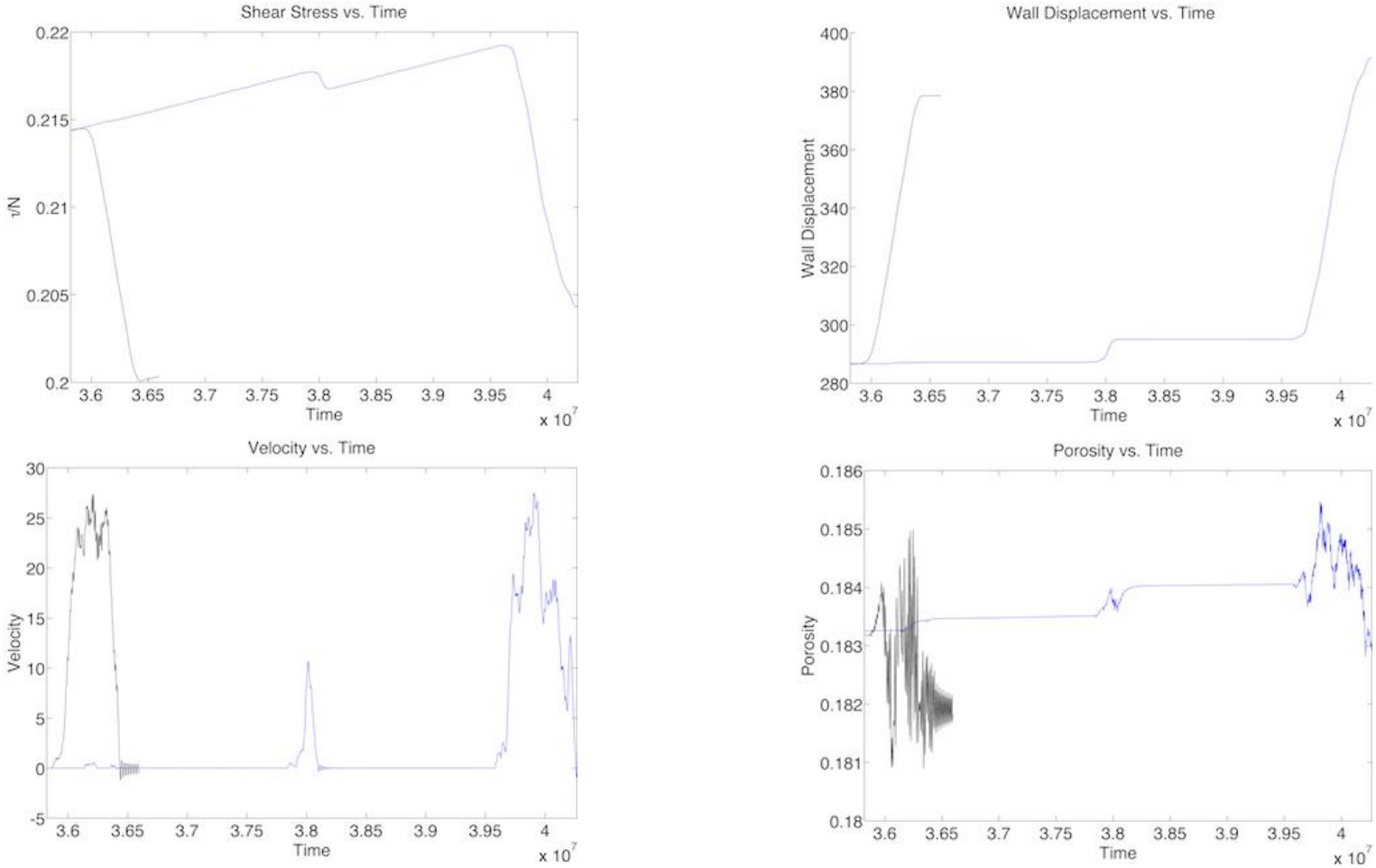

Figure D29. Differences in applied shear stress normalized by the constant effective confining stress, dimensionless velocity, dimensionless displacement, and dimensionless porosity from a drained (black) vs. undrained (blue) simulation. The parameters used in this simulation include: $N=3x10^{-4}$, $V_{sp}=1x10^{-5}$, $k=5x10^{-8}$, and $Perm=1x10^{-5}$. The undrained simulation was classified as a Type II-C earthquake [Table 3, Run 24 Dry Slip 4 II-C].

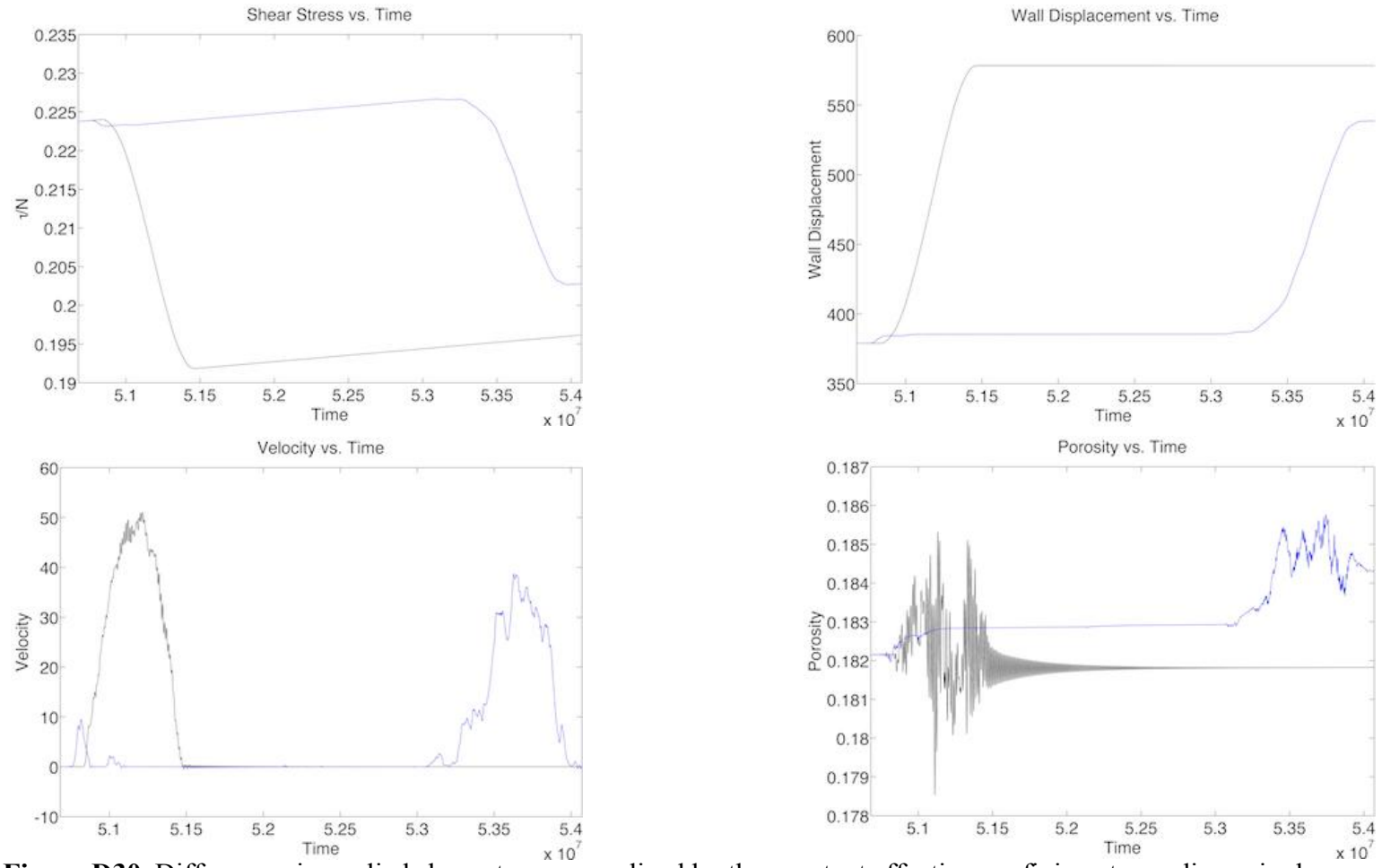

Figure D30. Differences in applied shear stress normalized by the constant effective confining stress, dimensionless velocity, dimensionless displacement, and dimensionless porosity from a drained (black) vs. undrained (blue) simulation. The parameters used in this simulation include: $N=3x10^{-4}$, $V_{sp}=1x10^{-5}$, $k=5x10^{-8}$, and $Perm=1x10^{-5}$. The undrained simulation was classified as a Type II earthquake [Table 3, Run 24 Dry Slip 5 II].

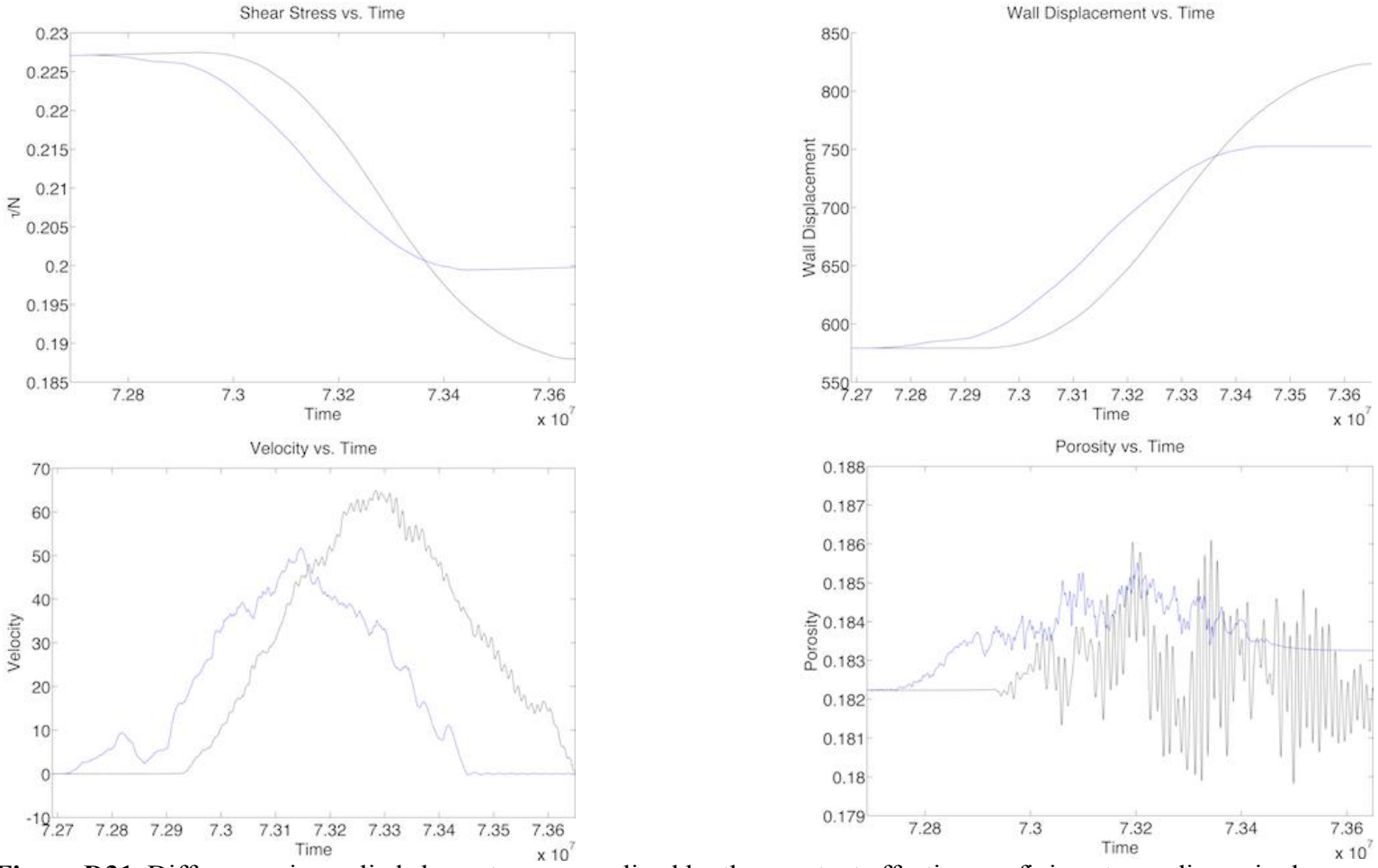

Figure D31. Differences in applied shear stress normalized by the constant effective confining stress, dimensionless velocity, dimensionless displacement, and dimensionless porosity from a drained (black) vs. undrained (blue) simulation. The parameters used in this simulation include: $N=3x10^{-4}$, $V_{sp}=1x10^{-5}$, $k=5x10^{-8}$, and $Perm=1x10^{-5}$. The undrained simulation was classified as a Type I earthquake [Table 3, Run 24 Dry Slip 6 I].

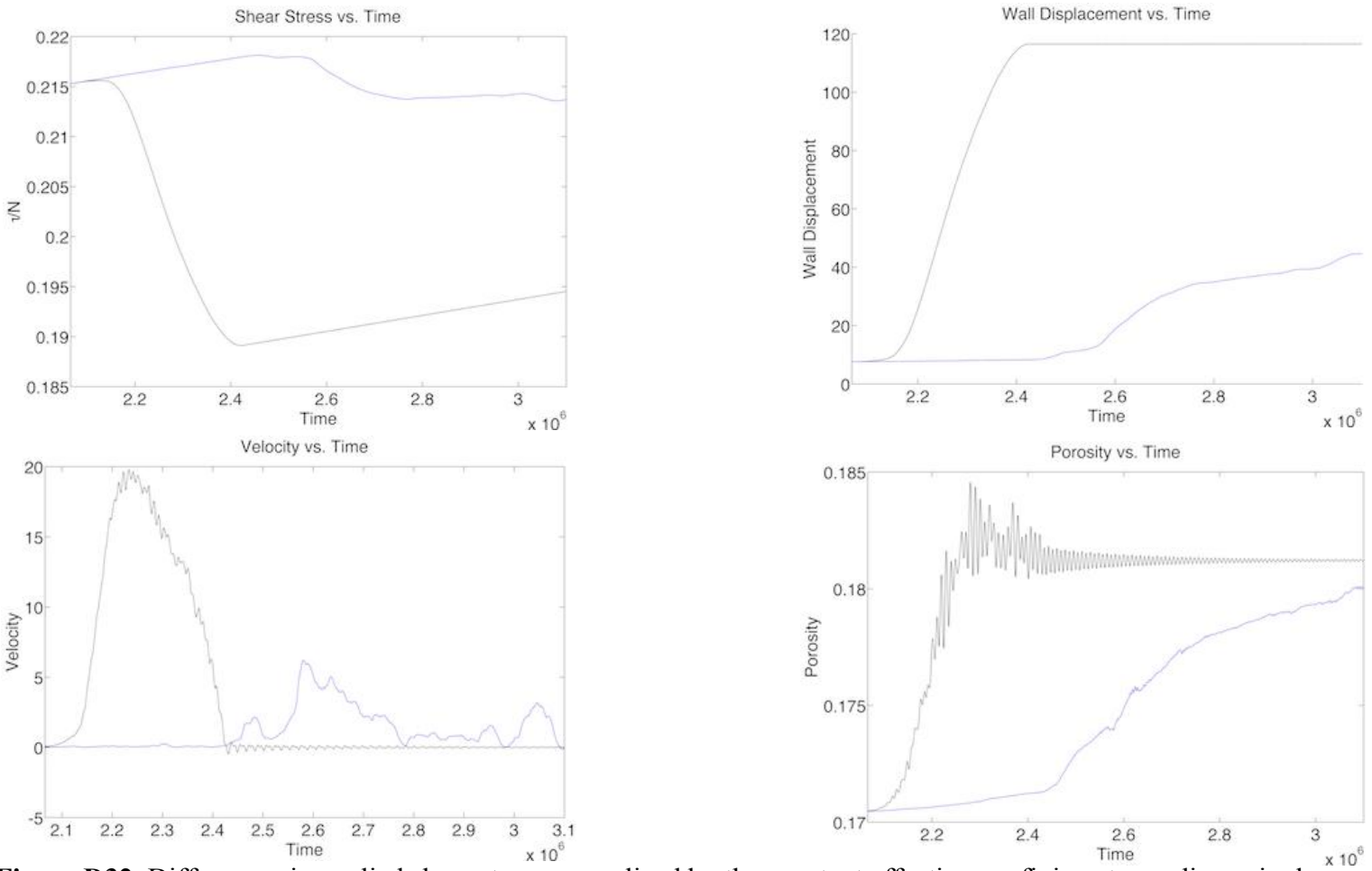

Figure D32. Differences in applied shear stress normalized by the constant effective confining stress, dimensionless velocity, dimensionless displacement, and dimensionless porosity from a drained (black) vs. undrained (blue) simulation. The parameters used in this simulation include: $N=3x10^{-4}$, $V_{sp}=3x10^{-5}$, $k=8x10^{-8}$, and $Perm=1x10^{-5}$. The undrained simulation was classified as a Type II-C earthquake [Table 3, Run 27 Dry Slip 1 II-C].

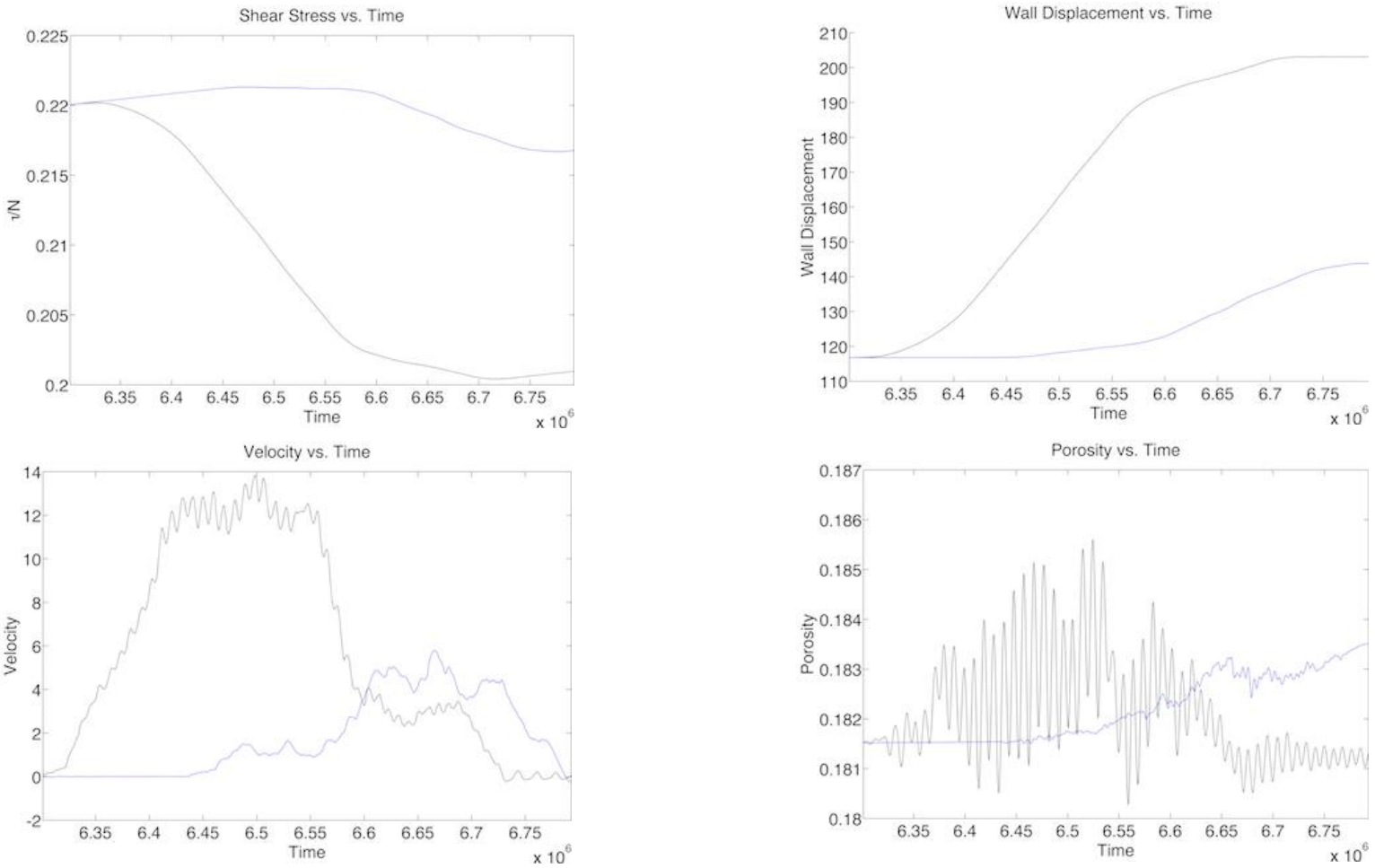

Figure D33. Differences in applied shear stress normalized by the constant effective confining stress, dimensionless velocity, dimensionless displacement, and dimensionless porosity from a drained (black) vs. undrained (blue) simulation. The parameters used in this simulation include: $N=3x10^{-4}$, $V_{sp}=3x10^{-5}$, $k=8x10^{-8}$, and $Perm=1x10^{-5}$. The undrained simulation was classified as a Type II-C earthquake [Table 3, Run 27 Dry Slip 2 II-C].

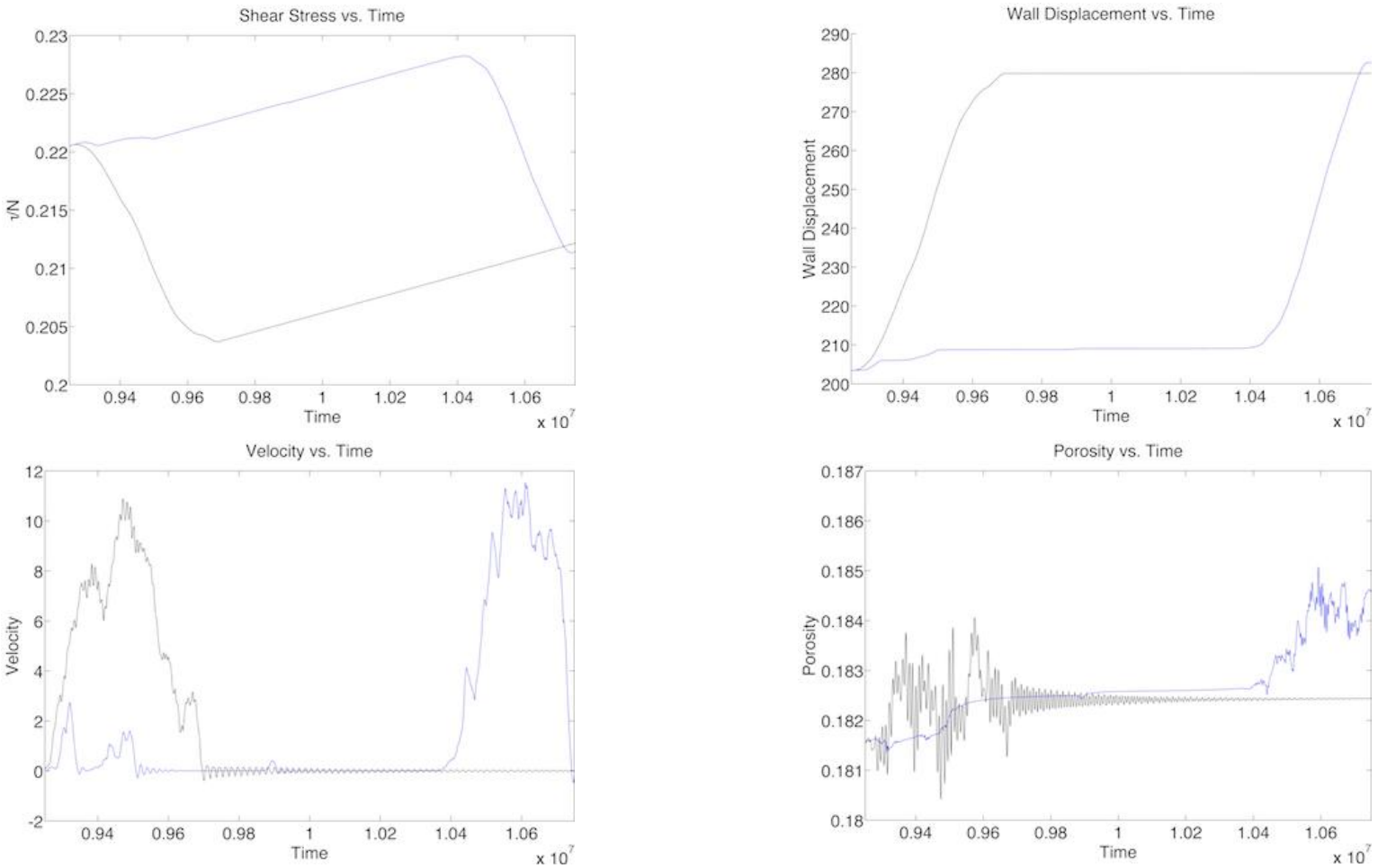

Figure D34. Differences in applied shear stress normalized by the constant effective confining stress, dimensionless velocity, dimensionless displacement, and dimensionless porosity from a drained (black) vs. undrained (blue) simulation. The parameters used in this simulation include: $N=3x10^{-4}$, $V_{sp}=3x10^{-5}$, $k=8x10^{-8}$, and $Perm=1x10^{-5}$. The undrained simulation was classified as a Type II-C earthquake [Table 3, Run 27 Dry Slip 3 II-C].

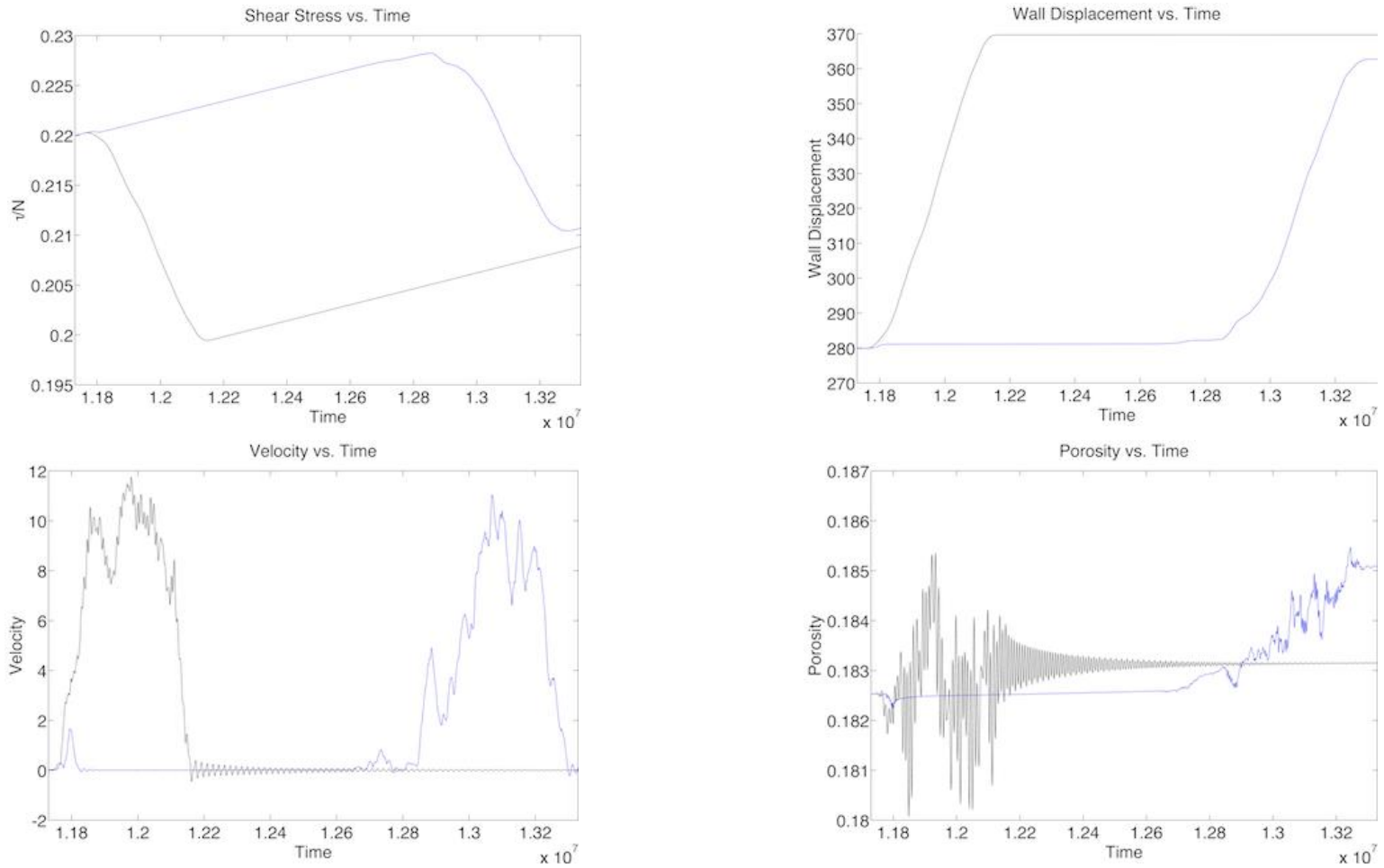

Figure D35. Differences in applied shear stress normalized by the constant effective confining stress, dimensionless velocity, dimensionless displacement, and dimensionless porosity from a drained (black) vs. undrained (blue) simulation. The parameters used in this simulation include: $N=3x10^{-4}$, $V_{sp}=3x10^{-5}$, $k=8x10^{-8}$, and $Perm=1x10^{-5}$. The undrained simulation was classified as a Type II-C earthquake [Table 3, Run 27 Dry Slip 4 II-C].

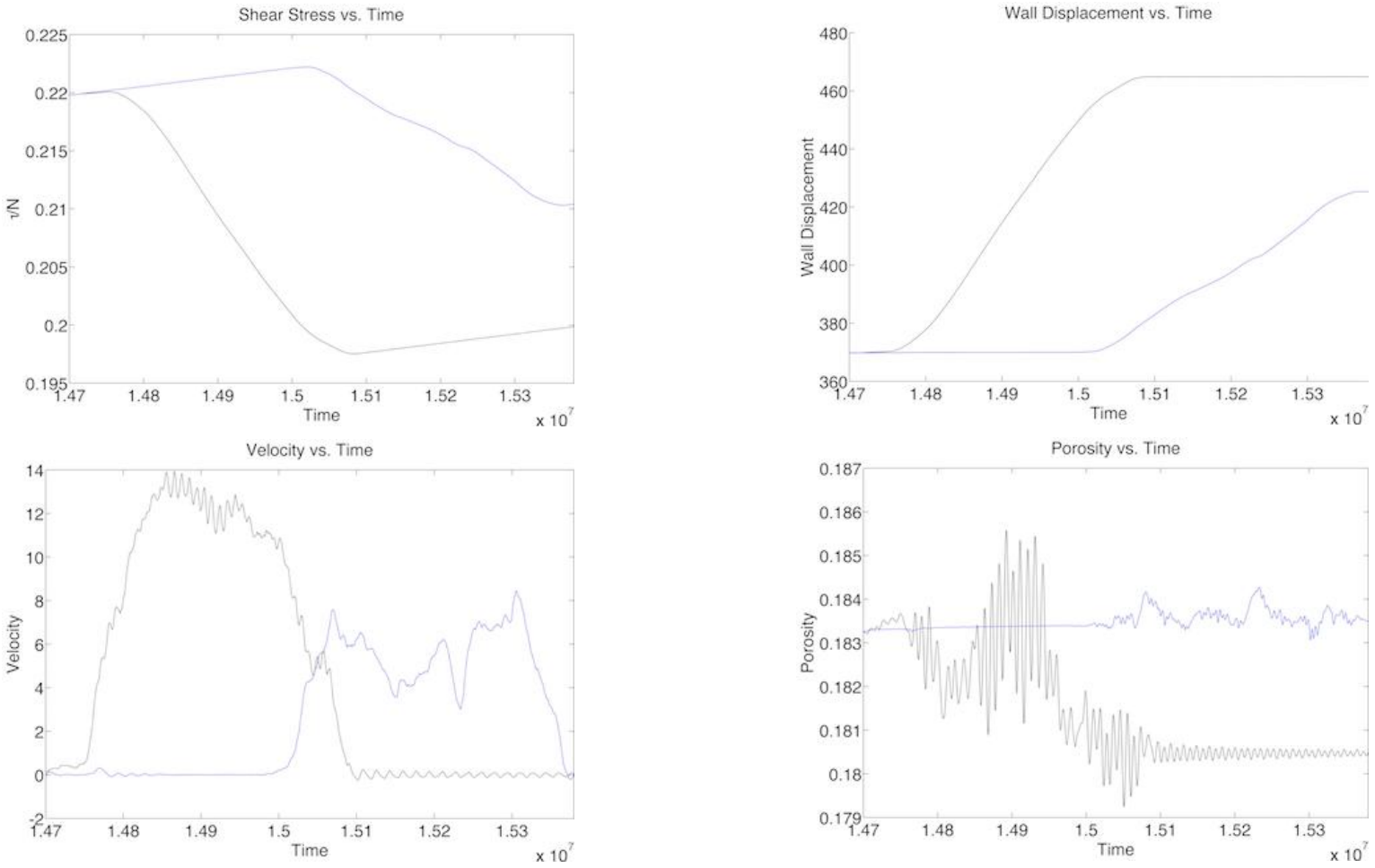

Figure D36. Differences in applied shear stress normalized by the constant effective confining stress, dimensionless velocity, dimensionless displacement, and dimensionless porosity from a drained (black) vs. undrained (blue) simulation. The parameters used in this simulation include: $N=3x10^{-4}$, $V_{sp}=3x10^{-5}$, $k=8x10^{-8}$, and $Perm=1x10^{-5}$. The undrained simulation was classified as a Type II-C earthquake [Table 3, Run 27 Dry Slip 5 II-C].

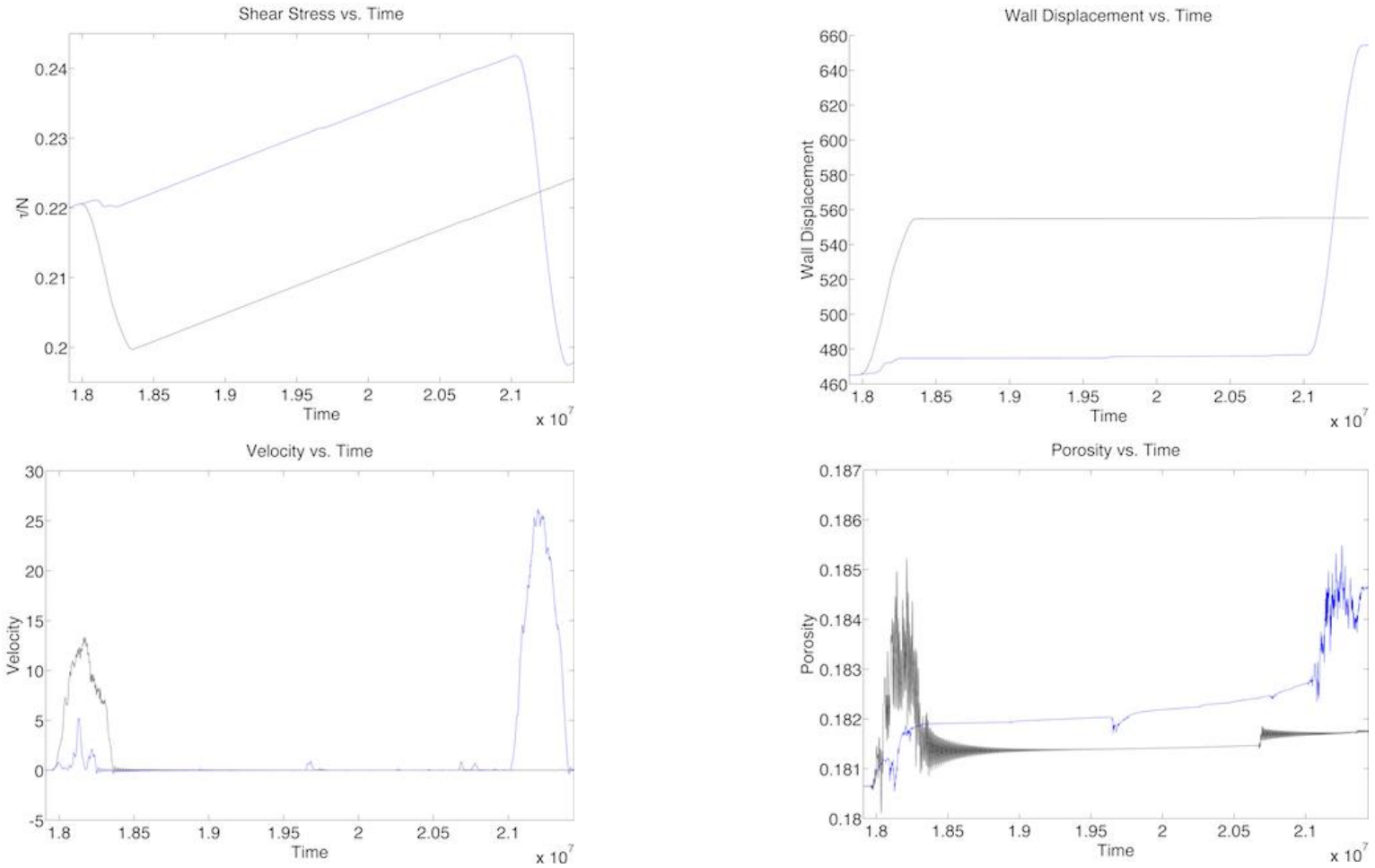

Figure D37. Differences in applied shear stress normalized by the constant effective confining stress, dimensionless velocity, dimensionless displacement, and dimensionless porosity from a drained (black) vs. undrained (blue) simulation. The parameters used in this simulation include: $N=3x10^{-4}$, $V_{sp}=3x10^{-5}$, $k=8x10^{-8}$, and $Perm=1x10^{-5}$. The undrained simulation was classified as a Type II earthquake [Table 3, Run 27 Dry Slip 6 II].

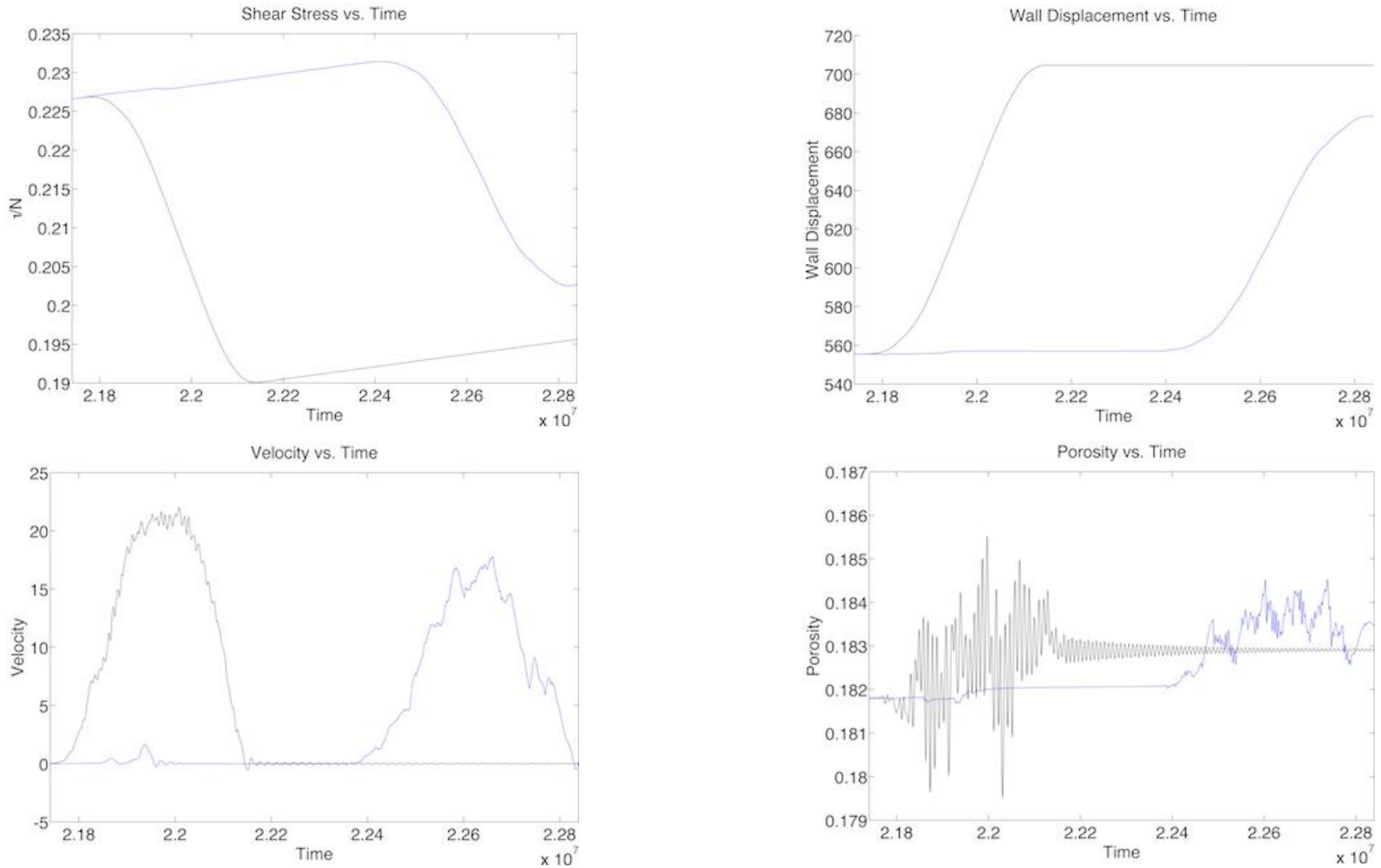

Figure D38. Differences in applied shear stress normalized by the constant effective confining stress, dimensionless velocity, dimensionless displacement, and dimensionless porosity from a drained (black) vs. undrained (blue) simulation. The parameters used in this simulation include: $N=3x10^{-4}$, $V_{sp}=3x10^{-5}$, $k=8x10^{-8}$, and $Perm=1x10^{-5}$. The undrained simulation was classified as a Type II earthquake [Table 3, Run 27 Dry Slip 7 II].

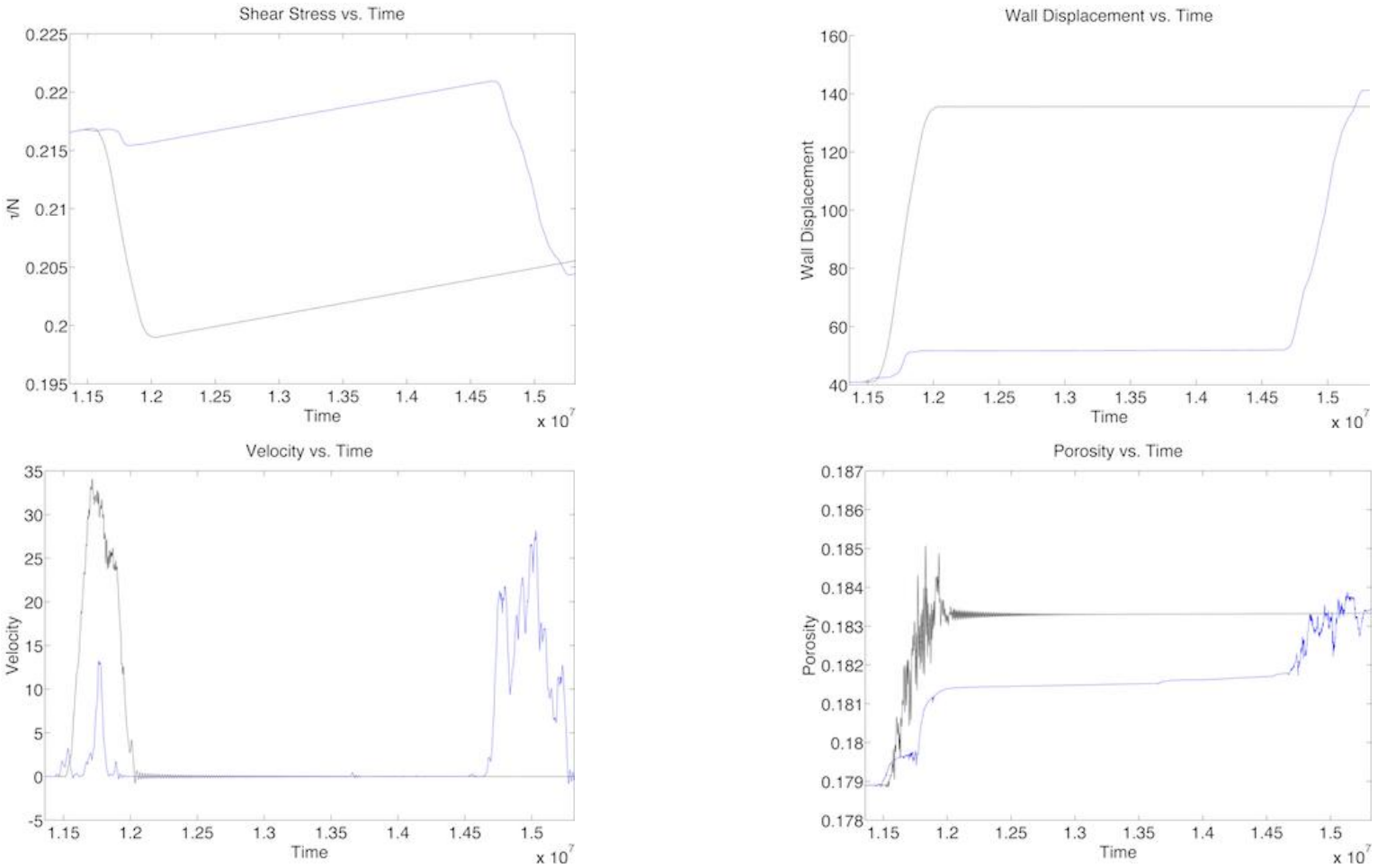

Figure D39. Differences in applied shear stress normalized by the constant effective confining stress, dimensionless velocity, dimensionless displacement, and dimensionless porosity from a drained (black) vs. undrained (blue) simulation. The parameters used in this simulation include: $N=3x10^{-4}$, $V_{sp}=1x10^{-5}$, $k=6x10^{-8}$, and $Perm=1x10^{-5}$. The undrained simulation was classified as a Type II-C earthquake [Table 3, Run 28 Dry Slip 2 II-C].

APPENDIX E

The Discrete Element Method follows the genneral outline of Cundall and Strack [1979], and we employ the code developed in Aharonov and Sparks [1998] and modified it to include fluid effects as described in Goren et al. [2011]. We track and compute contact forces using the following algorithm. We used the soft-grain model that uses very small penetrations of non-deforming grains to calculate repulsive elastic contact forces. If grain i and j are in contact, then r_{ij}, the distance between their centers, is less than the sum of their radii's, $R_i + R_j$. Thus, the amount of grain contact overlap used in the calculation of repulsive forces is given by $\xi_{ij} = R_i + R_j - r_{ij}$. Because the grains are under a normal confining pressure and shear stress, they exhibit normal forces and shear forces along their contacts. The normal force on the contact is calculated using:

$$F_{ij}^{n}(t) = \left[\tilde{k}_n \xi_{ij} - \gamma m_{ij} \left(\dot{r}_{ij} \bullet \hat{n}_{ij} \right) \right] \hat{n}_{ij} \qquad [8]$$

where $\tilde{k}_n \xi_{ij}$ is a nonlinear (Hertzian) elastic repulsive force due to granular overlap used in grain collisions, γm_{ij} is a dampening viscous force, $\dot{r}_{ij}$ represents the grains relative velocities, and $\hat{n}_{ij}$ is the unit vector normal to the contact. The coefficient of the normal repulsive force in Equation 8 is a nonlinear stiffness given by:

$$\tilde{k}_n = \frac{\sqrt{2}E}{3\left(1-\nu^2\right)} \left(R_{ij} \xi_{ij} \right)^{1/2} \qquad [9]$$

with E being the bulk modulus of the grain, ν is Poisson's ratio, and R_{ij} is the harmonic mean of the grain's radii. A nonlinear stiffness is used because the volume of a

sphere that is deformed by a contact increases as the force of the contact increases. The contact shear force calculation is made via an elastic-frictional law:

$$F_{ij}^{s}(t) = -\left[\min\left(\tilde{k}_s \Delta s, \mu F_{ij}^{n}\right)\right]\hat{s}_{ij} \qquad [10]$$

Here, Δs is the shear displacement since the time the grains first came into contact, μ is a friction coefficient to simulate surface roughness, and $\hat{s}_{ij}$ is the unit vector tangential to the point of contact. Similar to the normal force calculation, the shear force calculation also has a coefficient of the tangential repulsive force, $\tilde{k}_s$:

$$\tilde{k}_s = \frac{2^{3/2} E}{(2-\nu)(1+\nu)}\left(R_{ij}\xi_{ij}\right)^{1/2} \qquad [11]$$

Depending on the magnitude of these forces, two grains can slide against each other or stick. If μF_{ij}^{n} is larger the grains slide relative to each other, while if F_{ij}^{s} is larger the grain contact point will stick. All grains have a preset coefficient of static friction to simulate roughness because we use smooth grains. To simulate a number of grains moving and rotating, the forces calculated in Equation 8 and Equation 10 are used in momentum conservation equations:

$$m_i \dot{u}_i = m_i g + \sum_j F_{ij} - \frac{\nabla P \bullet V_i}{1-\phi} \qquad [12]$$

$$I_i \dot{\omega}_i = \sum_j R_i \dot{n}_{ij} \times F_{ij} \qquad [13]$$

In these equations, m_i is the mass of grain i, $\dot{u}_i$ is the velocity of grain i, g is gravitational acceleration, I is the grains moment of inertia, and $\dot{\omega}_i$ is the grain's rotational velocity. The change in gravitational acceleration from the top wall to the

bottom wall is negligible and hence neglected in these experiments. Lastly, the drag force exerted on grain i is given by the divergence of the fluid pressure gradient, ∇P, with its; volume V_i, normalized by the local solid fraction with ϕ being porosity. Although this modeled system is two-dimensional, so that positions and velocities of grains lie within a plane, the mass and inertia of grains is calculated as though they were spheres.

The addition of fluid is included in the model so the differences between low permeability and high permeability systems can be examined. To track fluid pressures, the following conservation equations for the solid and fluid phases are used as outlined by Goren et al. [2011]:

$$\frac{\partial\left[(1-\phi)\rho_s\right]}{\partial t}+\nabla\bullet\left[(1-\phi)\rho_s\mu_s\right]=0 \qquad [14]$$

$$\frac{\partial\phi\rho_f}{\partial t}+\nabla\bullet\left(\phi\rho_f u_f\right)=0 \qquad [15]$$

In these equations, t is dimensional time, ρ_s and ρ_f are densities of the solid and fluid respectively, with u_s representing u_f their velocities. The solid velocities are continuum velocities, interpolated onto the grid from the surrounding discrete grain velocities. The separation velocity of the two phases is assumed to be controlled by a Darcy-like flow law. In Equation 16, κ is permeability and η is fluid compressibility.

$$\phi\left(u_f-u_s\right)=-\frac{k}{\eta}\nabla P \qquad [16]$$

Finally, while the grains are taken to be incompressible, the fluid has a small but finite

compressibility.

$$\rho_f = \rho_0(1+\beta P) \quad [17]$$

Using these equations, Goren et al. [2011] determined an equation relating the temporal evolution of pressure to the granular movement and diffusion of pore pressure:

$$\frac{\partial P}{\partial t} = \frac{(1+\beta P)}{\beta\phi}\nabla \bullet \vec{u}_s + \frac{1}{\beta\phi}\nabla \bullet \left[(1+\beta P)\frac{\kappa}{\eta}\nabla P\right] \quad [18]$$

In this equation β is fluid compressibility, and $\vec{u}_s$ is the granular matrix velocity. The first term represents the evolution of pore pressure as a function of time. The second term creates pressure fluctuations caused by the dilation and compaction of the granular matrix. The final term is the diffusion of pressure fluctuations from fluid flow in pore spaces.

Because we are modeling a fault core bounded by a highly fractured zone, the boundary conditions for fluid flow set on the horizontal walls are free flow $(P=0)$. When the second and third term of Equation 18 balance each other, the system responds to shear as if it were effectively drained (no significant pressurizations are produced). On the other hand, the evolution of a slip event can be greatly affected when pressures from granular movement cannot diffuse to the free-flow boundaries quickly enough. After non-dimensionlization of Equation 18, Goren et al. [2011] term the equilibrium between these two terms as the Deborah (De) number (Equation 19):

$$De = \frac{l^2/D}{l/u_0} = \frac{t_{Diffusion}}{t_{generation}} \quad [19]$$

Here D is the diffusivity of pressure, and l is the dimensional distance from the isolated

pressure generation event to the walls of the system with free flow boundary conditions, and u_0 is the velocity of a grain. This dimensionless number describes the same relationships between the second and third terms in Equation 18 as discussed above. When $De << 1$ the isolated pressure generations within the granular system quickly diffuses through out the system (drained) having no effect on the evolution of a slip event. On the contrary, for $De >> 1$ the pressure generation from granular compaction and/or movement cannot flow (undrained) from the area, having little impact on pressure generation or reduction in the surrounding areas. We are interested in when fluid flow has an effect during earthquakes $(De \geq 1)$, that is, when fluid can neither flow too easily (such as at the boundaries) nor is it restricted too much where pressure diffusion cannot effect the surrounding system.

We numerically approximate Equation 18 by using a finite difference grid to average fluid pressures and grain velocities across a few grains. Gradients in these pressures act as a drag force on individual grains and are represented by the last term in Equation 19. Local geometric changes in the granular positions will change porosity (ϕ) throughout a simulation. Therefore, local permeability is calculated dynamically using a Carman-Kozeny-like relationship (Equation 20) adjusted for 2D porosity (*Goren et al.*, 2011].

$$\kappa = \kappa_c \frac{(1+2\phi)^3}{(1-\phi)^2} \qquad [20]$$

The pre-factor, κ_c, is a reference permeability set to a predetermined value. In our simulations, the mean permeability is about $10^{-14}\ m^2$ and it varies locally within the system from about $2.3\times10^{-14}\,m^2$ to $5.8\times10^{-15}\,m^2$. A mean permeability of $10^{-13}\,m^2$ allows enough fluid flow that even rapid slip events do not generate significant pressures. Note that the permeability used in these simulations is orders of magnitude larger than some real fault zone conditions [*Sutherland et al.*, 2012]. Using a permeability found in fault zones such as $10^{-19}\ m^2$, would make deviations in pressure even more pronounced [*Bianco*, 2013].